

APM $z \gtrsim 4$ QSO Survey: Spectra and Intervening Absorption Systems

L. J. Storrie-Lombardi¹, R. G. McMahon

*Institute of Astronomy Madingley Road, Cambridge CB3 0HA, UK,
lsl@ucsd.edu and rgm@ast.cam.ac.uk*

M. J. Irwin

Royal Greenwich Observatory Madingley Rd, Cambridge CB3 0EZ, UK, mike@ast.cam.ac.uk

and

C. Hazard

University of Pittsburgh, Pittsburgh, PA 15260 USA and Institute of Astronomy, hazard@ast.cam.ac.uk

arch-ive/9604021 — to appear in ApJ Supplements, 1 September 1996

ABSTRACT

The APM multicolor survey for bright $z > 4$ objects, covering 2500 deg² of sky to $m_r \sim 19$, resulted in the discovery of thirty-one quasars with $z \gtrsim 4$. High signal-to-noise optical spectrophotometry at 5Å resolution has been obtained for the twenty-eight quasars easily accessible from the northern hemisphere. These spectra have been surveyed to create new samples of high redshift Lyman-limit systems, damped Lyman- α absorbers, and metal absorption systems (e.g. CIV and MgII). In this paper we present the spectra, together with line lists of the detected absorption systems. The QSOs display a wide variety of emission and absorption line characteristics, with 5 exhibiting broad absorption lines and one with extremely strong emission lines (BR2248–1242). Eleven candidate damped Ly α absorption systems have been identified covering the redshift range $2.8 \leq z \leq 4.4$ (8 with $z > 3.5$). An analysis of the measured redshifts of the high ionization emission lines with the low ionization lines shows them to be blueshifted by 430 ± 60 km s⁻¹. In a previous paper (Storrie-Lombardi et al. 1994) we discussed the redshift evolution of the Lyman limit systems catalogued here. In subsequent papers we will discuss the properties of the Ly α forest absorbers and the redshift and column density evolution of the damped Ly α absorbers.

Subject headings: quasars: general — quasars: absorption lines — quasars: emission lines

¹current address: UCSD-CASS, Mail Code 0111, 9500 Gilman Drive, La Jolla, CA 92093 USA

1. Introduction

Many QSOs have now been discovered beyond redshifts of 4 and they provide powerful probes for exploring these early epochs. They are the youngest objects known in the Universe and it is likely that they flag regions where galaxy formation is very active. Their host galaxies are probably still forming and they may occur in the exceptional ‘ 5σ ’ peaks in the matter distribution of the early Universe (Efsthathiou & Rees 1988). Observational information from this epoch yields constraints on galaxy formation theories and clues for better understanding of the astrophysics of galaxy formation and evolution.

In addition to being of intrinsic interest themselves, bright high redshift QSOs are particularly valuable as probes of the intervening gas clouds and galaxies superimposed on their spectra in absorption. The study of these absorption systems provides information about the formation and evolution of galaxies over most of the age of the Universe. Neutral hydrogen (HI) absorption can be detected over a staggering 10 orders of magnitude from the Ly α forest region with the weakest detectable lines having a column density $N_{\text{HI}} \sim 10^{12}$ atoms cm^{-2} , up to the damped Ly α absorbers with $N_{\text{HI}} \sim 10^{21}$. The rich zoo of these absorbers, in addition to those produced by heavier elements such as carbon, silicon, oxygen, and magnesium, are illuminated along a QSO line-of-sight, leaving their imprint as absorption in the QSO continuum. Study of the Ly α forest ($12 \lesssim \log N_{\text{HI}} \lesssim 17$) yields important information about the intergalactic medium and the background ionizing flux at high redshifts (e.g. Hunstead et al. 1986; Carswell et al. 1987; Bajtlik, Duncan, & Ostriker 1988; Williger et al. 1994). Lyman-limit systems ($\log N_{\text{HI}} \gtrsim 17$) provide a means of directly studying the evolution of galaxies over the redshift range $0.1 < z < 5$ (e.g. Sargent, Steidel, & Boksenberg 1989; Lanzetta et al. 1991; Storrie-Lombardi et al. 1994; Stengler-Larrea et al. 1995). The absorbers detected via the damped Ly α lines they produce ($\log N_{\text{HI}} \gtrsim 20$) show features consistent with an early phase of galactic evolution and are widely believed to be the progenitors of spiral galaxies like our own (e.g. Wolfe et al. 1986; Wolfe 1987; Fall, Pei, & McMahon 1989; Pettini, Boksenberg, & Hunstead 1990; Rauch et al. 1990; Lanzetta et al. 1991; Lanzetta, Wolfe, & Turnshek 1995; Wolfe et al. 1995).

The APM Color Survey for $z > 4$ QSOs was under-

taken to find bright ($m_{\text{R}} \lesssim 19$) quasars with redshifts $4 \lesssim z \lesssim 5$ (Irwin, McMahon, & Hazard 1991). The aim of the program was to find a large sample of QSOs for both intrinsic and absorption line studies. The survey covers approximately 2500 square degrees of sky from the equatorial region of the UK Schmidt Telescope (UKST) B_J, R, I Survey with $|b| > 30^\circ$ and declination range +3 to -17.5 . High signal-to-noise optical spectrophotometry at 5\AA resolution covering the wavelength region 3500–9000 \AA were obtained for all the QSOs discovered in the APM Color Survey that are accessible using the William Herschel Telescope (WHT) (28 of 31 objects). In addition, spectra were obtained at 5\AA resolution of three high redshift radio-selected QSOs (Hook et al. 1995; McMahon et al. in preparation). The spectra have been utilized to discover Lyman-limit, damped Ly α , and metal absorption systems (e.g. CIV and MgII).

The results and analyses from these studies are presented in a series of papers. In this paper we present the spectra, together with a list of accurate redshift determinations of the intrinsic QSO emission lines, a study of the velocity differences between high and low ionization emission lines, and the results of surveys for intervening absorption systems. Line lists for damped Ly α candidates, Lyman limit systems, and metal absorption systems are provided. The analysis of the redshift evolution of the Lyman limit systems was previously presented in Storrie-Lombardi et al. (1994). We will present a detailed analysis of the damped Ly α systems and the redshift evolution of their number density and column density distribution (Storrie-Lombardi, Irwin, & McMahon 1996), and describe the implications derived from the damped Ly α survey for the evolution of the mass density of neutral gas with redshift and the implications for galaxy formation (Storrie-Lombardi, McMahon, & Irwin 1996). Other papers will cover studies of the Ly α forest clouds at high redshift and the intrinsic properties of the QSOs. High resolution studies of the Ly α forest region at $z > 4$ have been completed by Williger et al. (1994) and Wampler et al. (1996).

2. Observations

High signal-to-noise optical spectrophotometry at 5\AA resolution covering the wavelength range 3500–8800 \AA was obtained with the 4.2m William Herschel telescope of the Isaac Newton Group of telescopes in the Canary Islands. We used the ISIS double-spectrograph

with typical integration times of 2700-3600 seconds. The spectrophotometry is accurate to within 5-10 percent. ISIS is a double beam spectrograph with arms optimized for blue and red light, mounted at the f/11 Cassegrain focus of the WHT. For this project the lowest dispersion was required, and gratings with 158 lines/mm and a dichroic to split the light at $\sim 5400\text{\AA}$ were used. This gives $2.71\text{\AA}/\text{pixel}$ in the red arm and $2.89\text{\AA}/\text{pixel}$ in the blue. The gratings were arranged so that the blue part of the spectrum was centered on 4600\AA and covered a range of 2950\AA while the red was centered on 7000\AA and covered a range of 3380\AA . The red and blue arm observations were carried out simultaneously. On the red arm an English Electric Valve (EEV) 1242×1152 CCD with $22.5\mu\text{m}$ pixels was used as detector. On the blue arm a thinned Tektronix 1024×1024 CCD with $24\mu\text{m}$ pixels was used. All the narrow slit observations were taken with a slit width of $1.5''$ except for BR 2237 – 0607 ($1''$) and all were taken with the slit perpendicular to the horizon (at the parallactic angle). This slit orientation is used to minimize the effects of atmospheric differential refraction (Filippenko 1982).

Though the QSOs from the APM Color Survey are bright for high redshift objects ($m_R < 19$), they were barely visible on the acquisition TV, so nearby off-set stars ($m_R \sim 15 - 17$) were acquired first. Blind-offsetting was then used to position the target object in the slit and as a check the TV integration time was increased until the periphery of the QSO was visible in the slit. All observations were made with a long slit and the CCDs were windowed in the spatial direction to reduce the overhead due to readout time. The observations are summarized in table 1.

3. Data Reduction

The data were reduced using standard software from the IRAF² package. After the data were over-scan, bias, and flat-field corrected they were extracted using the variance-weighted extraction in APALL. Typically the ISIS spectra curved by less than a pixel from one end of the chip to the other. APALL outputs the sky spectrum which was used for quick wavelength calibration at the telescope. A sample dark sky spectrum taken with ISIS is shown in figure 1.

²IRAF is distributed by the National Optical Astronomy Observatories, which is operated by the Association of Universities for Research in Astronomy, Inc. (AURA) under cooperative agreement with the National Science Foundation.

CuNe+CuAr arcs were taken at intervals throughout the night to provide an accurate wavelength calibration. Emission lines were identified and a pixel-to-wavelength calibration curve was found by fitting a 3rd order chebyshev polynomial to the calibration points in IDENTIFY. Typical *rms* residuals from the fit were 0.2\AA . The dispersion solution was applied to the extracted spectra and they were put on a linear wavelength scale using DISPCOR.

The individual spectra were then extinction corrected and coadded. Spectrophotometric standards taken from Oke (1974) and Oke & Gunn (1983) were used to flux calibrate the spectra. The goal was absolute spectrophotometry correct to within 10 percent and relative flux levels from the blue and red arms accurate enough to allow determination of the spectral indices. The flux calibration procedure was checked by flux-calibrating the standards and overlaying calibration points. It was found that calibration was reliable over the wavelength range 5500\AA - 8600\AA (ISIS red) and 3500\AA - 5500\AA (ISIS blue). Observations with a $5''$ slit were obtained for all but three of the QSOs. These were reduced in the same way as the narrow slit observations and used to correct the absolute flux levels for slit losses. The slit losses ranged from 0–50%.

‘Featureless’ B-stars were selected from the *Bright Star Catalogue* (Hoffleit & Jaschek 1982) or *Sky Catalogue 2000.0* (Hirshfeld, Sinnott, & Ochsenbien 1991) for use in removing the effects of atmospheric absorption in the red spectra, (e.g. O₂ A-band at 7600\AA). Observations of B-stars were taken at different air masses to provide a range of absorption so that as many objects as possible could be corrected. The spectrum of HR4468 taken at an airmass of 1.48 is shown in figure 2 and HD13679 taken at an airmass of 1.06 is shown in figure 3(a). The atmospheric absorption features seen in the B-star spectrum were removed by interpolating between values on either side of the feature, resulting in the spectrum shown in figure 3(b). The original B-star spectrum was then divided by this featureless spectrum with the result shown in figure 3(c). The object spectra taken at comparable air masses were then divided by the result. The technique was successful in almost all cases though it remains an art form to do it properly.

The red and blue arm spectra were joined using SCOMBINE. The final reduced spectra are shown in figure 4 and the individual QSOs are described in

section 5. The AB magnitude³ measured at $\lambda_{rest} = 1450\text{\AA}$ and $\lambda_{observed} = 7000\text{\AA}$, along with the APM R magnitudes measured from the plate scans are listed in table 2. Using the absolute flux calibration for Vega taken from Hayes & Latham (1975) and defining the zero-point of the AB magnitude system at $\lambda = 5556\text{\AA}$ leads to the following magnitude zero-point differences: AB measures at $\lambda = 7000\text{\AA}$ are 0.25 magnitudes fainter than on a Vega-based system; for $\lambda = 1450 \times (1+z)\text{\AA}$ the difference ranges between 0.3 and 0.5 magnitudes for a $4 \lesssim z \lesssim 5$ sample; the effective wavelength of the photographic R-band is $\lambda = 6500\text{\AA}$ and the difference between the systems here is 0.2 magnitudes. The 1σ errors are ± 0.1 . For those objects with no long slit observations or non-photometric conditions, only the APM R magnitude is quoted.

4. Redshift Measurements

4.1. Measuring the Emission Line Redshifts

At redshifts greater than 4, Ly α +NV (rest wavelengths 1215.67 \AA and 1240.13 \AA) and CIV (1549.1 \AA) are usually the only strong emission lines visible. Ly α is almost 50% absorbed by the Ly α forest, making it difficult to use for redshift determination. Emission lines from Ly β (1025.72 \AA), OVI (1034.0 \AA), SiII (1263.0 \AA), OI (1304.46 \AA), CII (1335.0 \AA), SiIV+OIV] (1400.0 \AA), NIV] (1486.0 \AA), HeII (1640.4 \AA), and OIII] (1663.0 \AA) may also be detected. Single Gaussians were fit to the emission lines in each QSO, and the redshifts for each line were determined from the central wavelength ($z = \lambda_{observed}/\lambda_{emitted} - 1$). For the Ly α +NV blend the fit was mainly to the red wing due to the absorption by the forest. The redshifts for the strong metal lines were then averaged together (excluding Ly α) to determine a mean redshift for the QSO. The redshift of each of the emission lines, the mean QSO redshift, the 1σ error, and the lines used in the determination are shown in table 3.

4.2. Emission Line Velocity Shifts

There are uncertainties in the systemic redshift of the QSOs in that redshifts determined from high and low ionization lines have been shown to exhibit velocity differences up to 2000 km s⁻¹ (e.g. Espey et al. 1989; Steidel & Sargent 1991; Carswell et al. 1991;

Tytler & Fan 1992), where the velocity difference, Δv , is defined as

$$\Delta v = c \frac{z_{ion} - z_{civ}}{(1 + z_{civ})}.$$

The same trend is exhibited in the APM sample, with a median difference of 430 ± 60 km s⁻¹ between OI and CIV, with the high ionization line CIV blue-shifted with respect to the OI. The velocity difference relative to CIV has been calculated for all the measured emission lines and the results are summarized in table 4. The BAL QSOs have been excluded from this analysis. Histograms of the velocity differences are shown in figure 5. Some of the very large differences of several thousand kilometers per second are due to the difficulty in accurately measuring some of the heavily absorbed emission lines, e.g. Ly α . These shifts are important in estimating the metagalactic ultraviolet background flux based on the proximity effect (e.g. Williger et al. 1994) since an error in the redshift of the QSO of ~ 1000 km s⁻¹ can lead to a factor of 2–3 error in the derived ionizing flux.

5. Emission and Absorption Features

The character of the emission lines and the HI and metal absorption systems detected are described below for each QSO. Additional analysis of the intrinsic properties of the QSOs are described in a separate paper. The metal absorption systems in the non-BAL QSOs were selected with an automated algorithm that detected absorption features redward of Ly α emission with an equivalent width $W \geq 3\sigma$ in 2.5 resolution elements. In the cases where the feature detected included more than one line, Gaussians were fit to the lines individually to measure the redshifts and equivalent widths. The results, with 1σ errors, are listed in table 5, along with the identification of ion and redshift where possible. The selection of the damped Ly α candidates is discussed in section 6 and the Lyman limit systems previously published in Storrie-Lombardi et al. (1994) are summarized in table 6.

a) BR0019–1522, ($z_{em} = 4.528$)

The Ly α +NV and CIV emission lines are strong and sharp. There is a Lyman-limit system at $z=4.27$ and a damped Ly α candidate system at $z=3.98$. SiII, CIV, and FeII absorption are observed at $z=3.4$.

b) BRI0103+0032, ($z_{em} = 4.437$)

Strong and sharp Ly α and CIV, with weaker OI,

³ $AB = -2.5 * \log(f(\nu)[ergs/s/cm^2/Hz]) - 48.6$ as defined by Oke (1969).

CII, and SiIV+OIV] can be seen. There is weak MgII at $z=1.818$ with 2 corresponding FeII lines and MgII at $z=1.366$. There are absorption edges visible just shortward of the emission lines that correspond to OI+SiIII at $z=4.41$ and SiIV and CIV at $z=4.37$. There are two Lyman-limit systems at $z=4.31$ and 4.15 .

c) BR10151–0025, ($z_{em} = 4.194$)

The Ly α and CIV emission lines are strong and sharp with weaker OI and SiIV+OIV] emission. There is a Lyman-limit system at $z=4.05$ and CIV at $z=3.876$. At $z=4.17$ there is a strong Ly α absorption line, a NV doublet, and a single line that could be CIV. There is MgII with at least one FeII line at $z=1.91$.

d) BR10241–0146, ($z_{em} = 4.053$)

The Ly α +NV, OI, CII, SiIV+OIV], and CIV emission lines are broad and rounded. There is a strong Lyman-limit system at $z=4.10$. There are numerous absorption lines redward of the Ly α emission but they are not easily identifiable. MgII and FeII are identified at $z=1.435$. Shallow absorption troughs are also visible.

e) BR0245–0608, ($z_{em} = 4.238$)

The Ly α +NV, OI, SiIV+OIV], and CIV emission lines are weak. There is strong Ly α absorption on the blue side of the Ly α emission corresponding to the Lyman-limit system at $z=4.23$. An MgII doublet with 4 corresponding FeII lines is observed at $z=1.711$. There are strong, narrow Ly α absorption lines (though not damped candidates) at $z=3.36$ and 4.14 , with corresponding SiIV and CIV at $z=4.14$. CIV is also detected at $z=3.184$.

f) BR0351–1034, ($z_{em} = 4.351$)

This is one of the most unusual objects in the survey with saturated CIV absorption in the middle of the CIV emission. There are a large number of absorption lines including SiIV at $z=4.098$ and 4.352 , CIV at $z=3.633$, 4.098 , 4.351 , and 4.351 , MgII at $z=1.340$ and 1.931 , and NV at $z=4.353$. Due to the difficulty in measuring redshifts from the heavily absorbed emission lines, the redshift for this object was calculated from the CIV absorption at $z=4.351$.

g) BR0401–1711, ($z_{em} = 4.236$)

The Ly α +NV, OI, and CIV emission lines are strong and sharp, while the SiIV+OIV] is broader and weaker. The OI is unusually prominent. There is strong absorption in the CIV emission line at $z=4.229$.

There is Lyman limit system at the QSO redshift. The absorption feature at $\sim 7600\text{\AA}$ is a residual from the removal of the atmospheric absorption line. The spectrum is very noisy at the red end of the blue arm portion ($\sim 5600\text{\AA}$) and does not join together smoothly with the red arm spectrum.

h) BR0945–0411, ($z_{em} = 4.145$, BAL)

This is the first of the five QSOs in the APM Color Survey that exhibits broad absorption lines. OVI, NV, SiIV, and CIV are observed at $z\approx 4.01$.

i) BR0951–0450, ($z_{em} = 4.369$)

The Ly α +NV, OI, CII, SiIV+OIV], and CIV emission lines are weak. There are damped Ly α candidates at $z=3.84$ and 4.20 . CIV doublets are identified at $z=3.703$, 3.855 , 4.196 , and 4.364 and SiIV at $z=3.703$ and 3.858 . There is a Lyman-limit system at $z=4.22$.

j) BR10952–0115, ($z_{em} = 4.426$)

This QSO is gravitationally lensed (McMahon, Irwin, & Hazard 1992). The Ly α +NV, SiIV+OIV], and CIV emission are weak and heavily absorbed. There is a strong damped Ly α candidate systems at $z=4.01$. CIV doublets are identified at $z=3.294$, 3.475 , 3.719 and 4.023 and MgII at $z=1.993$. There is a Lyman-limit system at $z=4.25$.

k) BR11013+0035, ($z_{em} = 4.405$)

The Ly α +NV, OI, CII, SiIV+OIV], and CIV emission lines are weak. There is a damped Ly α candidate at $z=3.10$ with corresponding FeII detected. There is an MgII doublet at $z=2.054$ with 6 corresponding FeII lines at $z=2.058$. There is a Lyman-limit system at $z=3.78$.

l) BR1033–0327, ($z_{em} = 4.509$)

The Ly α +NV, OI, CII, SiIV+OIV], and CIV emission lines fall at the strong end of the weaker-lined objects. There is a Lyman-limit system at $z=4.19$ and CII tentatively identified at $z=4.148$. See Williger et al. (1994) for a detailed analysis of the Ly α forest region in this object.

m) BR11050–0000, ($z_{em} = 4.286$)

The Ly α and CIV emission lines are strong and sharp with weaker OVI, OI, and SiIV+OIV] emission. There is CII, SiIV, and CIV detected at $z=3.862$ and a Lyman-limit system at $z=4.08$.

n) BR11108–0747, ($z_{em} = 3.922$)

The Ly α and CIV emission are strong and this is one of the few objects where Ly β , OVI, and NV are easily distinguished, along with OI, CII, SiIV+OIV], and NIV]. CIV doublets are observed at $z=3.575$, and 3.607.

o) BRI1110+0106, ($z_{em} = 3.918$)

The Ly α +NV, OI, CII, SiIV+OIV], and CIV emission are weak. The O₂ A-band atmospheric absorption has been removed from the CIV emission line and a residual spike was cut-off, resulting in the unreal flat top to the emission line. MgII and 2 FeII lines are observed at $z=1.479$ and MgII at $z=1.800$.

p) BRI1114-0822, ($z_{em} = 4.495$)

The Ly α +NV, SiIV+OIV], and CIV emission lines are weak though the Ly β +OVI is fairly prominent. There is a damped Ly α candidate at $z=4.25$ and a Lyman-limit system at $z=4.51$. There is absorption in the blue wing of the Ly α emission line that corresponds to MgII at $z=1.395$ but no confirming FeII can be observed due to the Ly α forest. Single absorption lines are observed that could correspond to SiIV and CIV at $z=3.91$ and CIV at 4.25. CIV doublets are seen at $z=3.422$, 3.571, and 3.589. There is an MgII doublet at $z=1.794$.

q) BR1117-1329, ($z_{em} = 3.958$, BAL)

This QSO exhibits broad absorption lines for OVI, NV, SiIV, and CIV at $z=3.62$ and 3.89.

r) BR1144-0723, ($z_{em} = 4.147$, BAL)

This object exhibits broad absorption lines but also has detectable intervening absorption. There is a strong broad absorption trough corresponding to CIV and a weak trough for SiIV at $z=4.00$. The emission lines are weak. There is a damped Ly α candidate system at $z=3.26$ but this is probably confused with broad OVI absorption at $z=4.0$. There is MgII absorption at $z=1.905$ and 5 corresponding FeII lines.

s) BR1202-0725, ($z_{em} = 4.694$)

This is the highest redshift and brightest object in the APM sample. It has very weak emission lines with Ly α and CIV almost completely absorbed away. The spectrum is very similar to that of BRI1335-0417, described below. The redshift is determined from the edge of the Ly α emission line since the metal lines are so heavily absorbed. (The redshift determined from OI and CIV is 4.679.) There is a damped Ly α system at $z=4.38$ and a Lyman-limit system at $z=4.52$. MgII doublets, some with associated FeII, are

observed at $z=1.463$, 1.754, 2.238, 2.339, and 2.444. CIV is detected at $z=3.525$, 3.565, 4.474, and 4.679. See Wampler et al. (1996) for a detailed analysis of the Ly α forest in this object.

t) BR1302-1404, ($z_{em} = 3.996$, BAL)

This QSO exhibits a complex series of broad absorption lines for OVI, NV, SiIV, and CIV at $z \approx 3.65$, 3.72, and 3.92. There are two MgII doublets at $z=2.044$ and 2.058 with 4 and 3 associated FeII lines, respectively.

u) BRI1328-0433, ($z_{em} = 4.217$)

The OVI, Ly α , NV, SiIV+OIV], and CIV emission lines are strong with weaker OI present. This is one of the few objects in the sample with well defined NV emission. There is strong MgII absorption at $z=1.628$ with 2 FeII lines. Lyman-limit systems are seen at $z=3.31$ and 4.25.

v) BRI1335-0417, ($z_{em} = 4.396$)

The Ly α +NV and CIV emission lines are very weak, with the Ly α almost completely absorbed away. This QSO is looks very similar to BR1202-0725. MgII with 4 associated FeII lines is seen at $z=1.822$. There is a Lyman-limit system at $z=4.45$ and SiII and CII at $z=4.40$. There is strong Ly α absorption at the QSO redshift.

w) BRI1346-0322, ($z_{em} = 3.992$)

The Ly α and CIV emission lines are very strong and sharp. There is NV absorption at $z=3.974$. There are CIV doublets at $z=3.359$ and 3.994, and a single line that is most likely CIV at $z=3.974$. MgII with FeII is seen at $z=1.944$. There is a damped Ly α candidate at $z=3.73$ and a corresponding Lyman-limit absorption edge at $z=3.75$.

x) BRI1500+0824, ($z_{em} = 3.943$)

The Ly α +NV, OI, SiIV+OIV], and CIV emission lines are weak but sharp. There is a damped Ly α candidate at $z=2.80$, MgII with 6 FeII lines at $z=1.908$, and CIV absorption in the emission line at $z=3.940$. This object shows one of the most successful removals of the O₂ A-band absorption at 7600Å, in the middle of the CIV emission.

y) GB1508+5714, $z_{em} = 4.283$

This is a radio-selected object from Hook et al. (1995). The Ly α and CIV emission lines are strong and sharp. There is a Lyman-limit system at $z=3.9$.

z) MG1557+0313, $z_{em} = 3.891$

This is a radio-selected object from McMahon et al. (in preparation). The Ly α and CIV emission are strong and sharp. There is CIV absorption at $z=3.898$.

aa) GB1745+6227, $z_{em} = 3.901$

This is a radio-selected object from Hook et al. (1995), also discovered independently by Becker, Helfand, & White (1992) on the basis of its X-ray emission. The Ly α and CIV emission are strong and sharp. It has MgII absorption at $z=1.471$. There are 6 FeII lines at $z=2.322$, but the corresponding MgII doublet is not seen as it should occur at 9296Å, redward of the end of this spectrum.

bb) BR2212–1626, ($z_{em} = 3.990$)

The Ly α +NV and CIV emission lines are strong and sharp with weaker OI, SiIV+OIV], and NIV].

cc) BRI2235–0301, ($z_{em} = 4.249$, BAL)

This QSO is the highest redshift BAL in the sample and has very broad absorption troughs. The emission lines are almost completely absorbed, making it difficult to determine an accurate redshift. It exhibits broad absorption lines of OVI ($z= 4.08$), NV ($z=3.74$), SiIV ($z=3.83$), and CIV ($z=3.65, 3.82, 4.03$). There is a possible MgII doublet at $z=1.873$.

dd) BR2237–0607, ($z_{em} = 4.558$)

The Ly α +NV, OI, SiIV+OIV], and CIV emission are strong with the Ly α line being particularly sharp. There is a damped Ly α candidate at $z=4.08$ and a Lyman-limit system at $z=4.28$. There is a NV doublet at $z=4.545$, SiIV at $z=4.079$, CII at $z=4.078$, CIV at $z=4.482$, FeII at $z=2.155$, and MgII at $z=1.672$.

ee) BR2248–1242, ($z_{em} = 4.161$)

This QSO has pathologically strong emission lines for OVI+Ly β , Ly α , NV, OI, CII, SiIV+OIV], NIV], CIV, HeII, and OIII]. It is the only object with obvious NIV].

6. Survey for Damped Lyman- α Absorption Systems

6.1. Background

While the baryonic content of spiral galaxies that are observed in the present epoch is concentrated in stars, in the past this must have been in the form of gas. The principal gaseous component in spirals is

neutral hydrogen which has led to surveys for absorption systems detected by the damped Ly α (DLA) lines they produce (Wolfe et al. 1986; Lanzetta et al. 1991; Lanzetta et al. 1995; Wolfe et al. 1995). Damped Ly α absorption systems comprise the high column density tail of neutral hydrogen absorbers with column densities of $N_{\text{HI}} \geq 2 \times 10^{20} \text{ cm}^{-2}$. They are identified by the presence of broad (FWHM $>5\text{\AA}$) absorption lines shortward of Lyman- α (1216Å) in the QSO rest frame. These lines are broadened by radiation damping and at $z>4$ have observed equivalent widths of $W \gtrsim 25\text{\AA}$. The visibility of the damping wings in the absorption profile is due to the large HI column density and the low velocity dispersion ($\sim 10 \text{ km s}^{-1}$), two features that damped systems have in common with spiral galaxies observed at the present. The column density along a typical line-of-sight in the Milky Way is $N_{\text{HI}} \sim 10^{21} \text{ atoms cm}^{-2}$. Other features that resemble HI disk galaxies are the presence of metals in mainly low ionization states such as C+, Si+, and Fe+ and the detection of 21 cm absorption associated with damped systems shows that the gas is cold and has a low level of turbulence (*c.f.* Wolfe et al. 1986; Wolfe 1987; Turnshek et al. 1989).

6.2. Selection of Damped Ly α Candidates

The Ly α forest region in QSO spectra at redshift 4 is very crowded. Many lines are blended at 5Å resolution and may appear broader than they actually are. However, real damped absorbers at high redshift result in very broad lines. They have observed equivalent widths $W > 25\text{\AA}$ and are relatively easy to see in the spectra. Two techniques were used to select the candidate absorbers. We first selected the candidates interactively and then independently used the standard equivalent width selection criteria with an automated algorithm. There was good agreement between the two selection methods though we only report the candidates selected with the automated algorithm. This is described below.

The technique used for selecting candidates and measuring the sensitivity of the survey with redshift follows the methods described in Lanzetta et al. (1991) and is described below. A local continuum was fit to each spectrum using straight lines between the peaks of the forest regions. An equivalent width spectrum and variance spectrum were created for each

QSO defined as

$$W_i = \Delta\lambda \sum_{n=i-m}^{i+m} (1 - F_n/C_n), \text{ and}$$

$$\sigma_{E_i}^2 = (\Delta\lambda)^2 \sum_{n=i-m}^{i+m} (\sigma_{F_n}/C_n)^2,$$

where C_i and F_i are the continuum and flux levels at pixel i , $\Delta\lambda$ is the $\text{\AA}/\text{pixel}$ of the spectrum, and $2m+1$ is the passband over which the total equivalent width is measured. A passband of 15 pixels was used, equivalent to 37.5\AA .

The spectra were analyzed using the above algorithm starting 3000 km s^{-1} blueward of the emission redshift to avoid lines possibly associated with the quasar. The analysis was stopped when the signal-to-noise ratio became too low to detect a Ly α line with $W(\text{rest}) \geq 5\text{\AA}$ at the 5σ level. This point was typically caused by the incidence of a Lyman limit system. This selected wavelength range is used to construct the sensitivity function, $g(z)$. It gives the number of lines of sight at a given redshift over which damped systems can be detected at a $> 5\sigma$ level (see Lanzetta et al. 1991 or Lanzetta et al. 1995). Figure 6 shows the sensitivity function of the APM survey compared with three previous damped Ly α surveys (Wolfe et al. 1986; Lanzetta et al. 1991; Lanzetta et al. 1995). The APM survey adds substantial redshift path for damped Ly α absorption system surveys, more than trebling the path surveyed for $z > 3$. The redshift path over which damped systems could be detected is crucial in estimating the cosmological mass density in neutral gas from the damped systems (Storrie-Lombardi, McMahon, & Irwin 1996). Gaussians were fit to the lines selected by the algorithm, and N_{HI} was estimated for features with $W > 20\text{\AA}$. Of the 32 measured, 11 have estimated $N_{\text{HI}} \geq 2 \times 10^{20} \text{ cm}^{-2}$ covering $2.8 \leq z \leq 4.4$. Only one candidate has estimated $N_{\text{HI}} \geq 10^{21} \text{ cm}^{-2}$. They are all listed in table 7 along with the QSOs with no candidates detected above this threshold. The absorbers listed in table 7 are marked with a vertical slash in the spectra in figure 7. The damped Ly α candidates with estimated column densities above the threshold of $\log N_{\text{HI}} \geq 20.3$ have an asterisk after the column density in table 7 and a circle around the vertical slash in figure 7.

To test this selection procedure, simulated high resolution spectra with damped systems included at known column densities were degraded to 6\AA resolution and the column densities estimated with the

above technique. The estimates were within $\pm 0.2 \times 10^{20} \text{ atoms cm}^{-2}$ of the real value. Two simulated QSOs are shown in figure 8. Panels (a) and (b) show a $z = 3.86$, $\log N_{\text{HI}} = 20.69$ damped Ly α absorption system in a $z = 4.37$ QSO at 1.6\AA and 6\AA resolution, respectively, with a signal-to-noise ratio of 25. Panels (c) and (d) show a $z = 3.73$, $\log N_{\text{HI}} = 20.15$ Ly α absorption system in a $z = 4.51$ QSO at 1.6\AA and 6\AA resolution, respectively, with a signal-to-noise ratio of 10.

Many of the damped candidates have estimated N_{HI} near the statistical sample threshold of $N_{\text{HI}} = 2 \times 10^{20} \text{ atoms cm}^{-2}$ (Wolfe et al. 1986). Some of those with $N_{\text{HI}} < 2 \times 10^{20}$ will be confirmed as damped and some of these with $N_{\text{HI}} \geq 2 \times 10^{20}$ will turn out to be blends of weaker lines. Higher resolution spectra are essential to verify the individual column densities though the estimates should give an accurate representation of their distribution at high redshift. Three of the candidates have been observed at ESO with the NTT and these are discussed in Storrie-Lombardi, Irwin & McMahon (1996). Preliminary results from 1.5\AA resolution spectra taken with LRIS on the Keck telescope indicate that the rest of the candidates selected are representative of the true distribution of HI column densities at high redshift (Storrie-Lombardi & Wolfe, in preparation). When the follow-up spectroscopy is complete, this will result in a complete sample of damped absorbers for $z > 3.5$, increasing the confirmed numbers of these absorbers by ~ 20 percent and covering an epoch crucial to understanding the formation of galaxies.

7. Conclusions

Intermediate resolution (5\AA) spectrophotometry are presented for 31 QSOs with redshifts $3.9 \leq z \leq 4.7$, 28 from the APM Color Survey and 3 radio-selected objects. The spectra were surveyed to create new data sets of intervening absorption lines systems. The QSOs display a wide variety of emission and absorption line characteristics, with 5 exhibiting broad absorption lines and one with extremely strong emission lines (BR2248–1242).

This high redshift data set more than triples the $z > 3$ redshift path available for damped Ly α absorption system surveys. Eleven candidate damped systems have been identified covering the redshift range $2.8 \leq z \leq 4.4$ (8 with $z > 3.5$). The redshift evolution, column density distribution func-

tion, and contribution to the cosmological mass density from these systems is discussed in other papers (Storrie-Lombardi, Irwin, & McMahon 1996; Storrie-Lombardi, McMahon, & Irwin 1996).

The Lyman-limit systems in the QSOs with $z \geq 4.2$ are catalogued and the spectra presented. Their redshift evolution has been discussed in a previous paper (Storrie-Lombardi et al. 1994). In addition, line lists for metal absorption line systems (e.g. CIV and MgII) are presented. An analysis of the measured redshifts of the high ionization emission lines with the low ionization lines shows them to be blueshifted by $430 \pm 60 \text{ km s}^{-1}$.

We thank an anonymous referee and Mike Fall for suggestions that improved the paper and Art Wolfe for the use of his code in the automated damped candidate selection. We thank the PATT for time awarded to do the observations with the William Herschel Telescope that made this work possible. LSL acknowledges support from an Isaac Newton Studentship, the Cambridge Overseas Trust, and a University of California President's Postdoctoral Fellowship. RGM acknowledges the support of the Royal Society.

REFERENCES

- Bajtlik, S., Duncan, R.C., & Ostriker, J.P. 1988, *ApJ*, 327, 570
- Becker, R.H., Helfand, D.J., & White, R.L. 1992, *ApJ*, 104, 531
- Carswell, R.F., et al. 1991, *ApJ*, 381, L5
- Carswell, R.F., Webb, J.K., Baldwin, J.A., & Atwood, B. 1987, *ApJ*, 319, 709
- Espey, B.R., Carswell, R.F., Bailey, J.A., Smith, M.G. & Ward, M.J., 1989, *ApJ*, 342, 666
- Fall, S.M., Pei, Y.C., & McMahon, R.G. 1989, *ApJ*, 341, L5
- Filippenko, A.V. 1982, *PASP*, 94, 715
- Hayes, D.S. & Latham, D.W., 1975, *ApJ*, 197, 593
- Hirshfeld, A., Sinnott, R.W., & Ochsbenien, F. 1991, *Sky Catalogue 2000.0* Cambridge University Press
- Hoffleit, D. & Jaschek, C. 1982, *Bright Star Catalogue* Yale University Observatory
- Hook, I.M., McMahon, R.G., Patnaik, A.R., Browne, W.A., Wilkinson, P.N., Irwin, M.J., & Hazard, C., 1995, *MNRAS*, 273, L63
- Hunstead, R.W., Murdoch, H.S., Peterson, B.A., Blades, J.C., Jauncey, D.L., Wright, A.E., Pettini, M., & Savage, A. 1986, *ApJ*, 305, 496
- Irwin, M.J., McMahon, R.G., & Hazard, C. 1991, in *Astronomical Society of the Pacific Conference Series*, Vol. 21, ed. D. Crampton (San Francisco: Astronomical Society of the Pacific), 117
- Lanzetta, K.M. 1991, *ApJ*, 375, 1
- Lanzetta, K.M., Wolfe, A.M., & Turnshek, D.A. 1995, *ApJ*, 440, 435
- Lanzetta, K.M., Wolfe, A.M., Turnshek, D.A., Lu, L., McMahon, R.G., & Hazard, C. 1991, *ApJS*, 77, 1
- McMahon, R.G., Irwin, M.J., & Hazard, C. 1992, *Gemini Issue* 36, 1
- McMahon, R.G., Omont, A., Bergeron, J., Kreysa, E., & Haslam, C.G.T., 1994, *MNRAS*, 267, L9
- Oke, J.B. 1969, *PASP*, 81, 11
- Oke, J.B. 1974, *ApJS*, 27, 21
- Oke, J.B. & Gunn, J.E. 1983, *ApJ*, 266, 713
- Pettini, M., Boksenberg, A., & Hunstead, R.W. 1990, *ApJ*, 348, 48
- Rauch, M., Carswell, R.F., Robertson, J.G., Shaver, P.A., & Webb, J.K. 1990, *MNRAS*, 242, 698
- Sargent, W.L.W., Steidel, C.C., & Boksenberg, A. 1989, *ApJS*, 79, 703
- Steidel, C.C. & Sargent, W.L.W. 1991, *ApJ*, 382, 433
- Stengler-Larrea, E.A., Boksenberg, A., Steidel, C.C., Sargent, W.L.W., Bahcall, J.N., Bergeron, J., Hartig, G.F., Januzzi, B.T., Kirhakos, S., Savage, B.D., Schneider, D.P., Turnshek, D.A., & Weymann, R.J., 1995, *ApJ*, 444, 64
- Storrie-Lombardi, L.J., Irwin, M.J., & McMahon, R.G. 1996, *MNRAS*, submitted
- Storrie-Lombardi, L.J., McMahon, R.G., & Irwin, M.J. 1996, *ApJ*, submitted
- Storrie-Lombardi, L.J., McMahon, R.G., Irwin, M.J., & Hazard, C. 1994, *ApJ*, 427, L13
- Turnshek, D.A., Wolfe, A.M., Lanzetta, K.M., Briggs, F.H., Cohen, R.D., Foltz, C.B., Smith, H.E., & Wilkes, B.J. 1989, *ApJ*, 344, 567
- Tytler, D. & Fan, X.M. 1992, *ApJS*, 79, 1
- Williger, G.M., Baldwin, J.A., Carswell, R.F., Cooke, A.J., Hazard, C., Irwin, M.J., McMahon, R.G., & Storrie-Lombardi, L.J. 1994, *ApJ*, 428, 574
- Wampler, E.J., Williger, G.M., Baldwin, J.A., Carswell, R.F., Hazard, C., & McMahon, R.G., 1996, *A&A*, submitted
- White, R.L. & Becker, R.H., 1992, *ApJS*, 79, 331
- Wolfe, A.M. 1987, *Proc. Phil. Trans. Roy. Soc.*, 320, 503
- Wolfe, A.M., Lanzetta, K.M., Foltz C.B., & Chaffee F.H., 1995, *ApJ*, 454, 698
- Wolfe, A.M., Turnshek, D.A., Smith, H.E., & Cohen, R.D. 1986, *ApJS*, 61, 249

This 2-column preprint was prepared with the AAS L^AT_EX macros v4.0.

Fig. 1.— The 5Å resolution flux calibrated sky spectrum from QSO BRI1335–0417 taken with the red and blue arms of the ISIS spectrograph at the WHT.

Fig. 2.— B-star HR4468: [B9.5, $m_V = 4.7$, exposure=1 second, 92 Apr 24, airmass=1.48]

Fig. 3.— B-star HD13679: [B8, $m_V = 6.8$, exposure=1 second, 93 Aug 21, airmass=1.056] (a) wavelength calibrated counts spectrum, (b) with atmospheric absorption features removed, and (c) the spectrum in ‘a’ divided by the spectrum in ‘b’. The absorption spectrum in ‘c’ is then divided into the QSO spectra taken at a similar airmass to remove the atmospheric absorption features.

Fig. 4.— The final flux calibrated spectra. The $z > 4.2$ QSOs used in the Lyman limit system evolution analysis show the region blueward of 5500Å magnified in the upper left hand corner. All except BR0351–1034, BR0401–1711 and BR2237–0607 show the flux corrected for slit losses.

Fig. 4 *continued.*— The flux for BR0351–1034 has not been corrected for slit losses.

Fig. 4 *continued.*— The flux for BR0401–1711 has not been corrected for slit losses.

Fig. 4 *continued.*—

Fig. 4 *continued.*—

Fig. 4 *continued.*—

Fig. 4 *continued.*—

Fig. 4 *continued.*—

Fig. 4 *continued.*—

Fig. 4 *continued.*— The flux for BR2237–0607 has not been corrected for slit losses.

Fig. 4 *continued.*— The upper panel shows the entire spectrum of BR2248-1242. The lower panel has the Ly α and CIV emission lines cut off to show the additional lines visible in the spectrum.

Fig. 5.— Histograms of the velocity difference relative to CIV for all the measured emission lines are shown. These are tabulated in table 4. Some of the very large differences of several thousand kilometers per second are due to the difficulty in accurately measuring some of the heavily absorbed emission lines, e.g. Ly α .

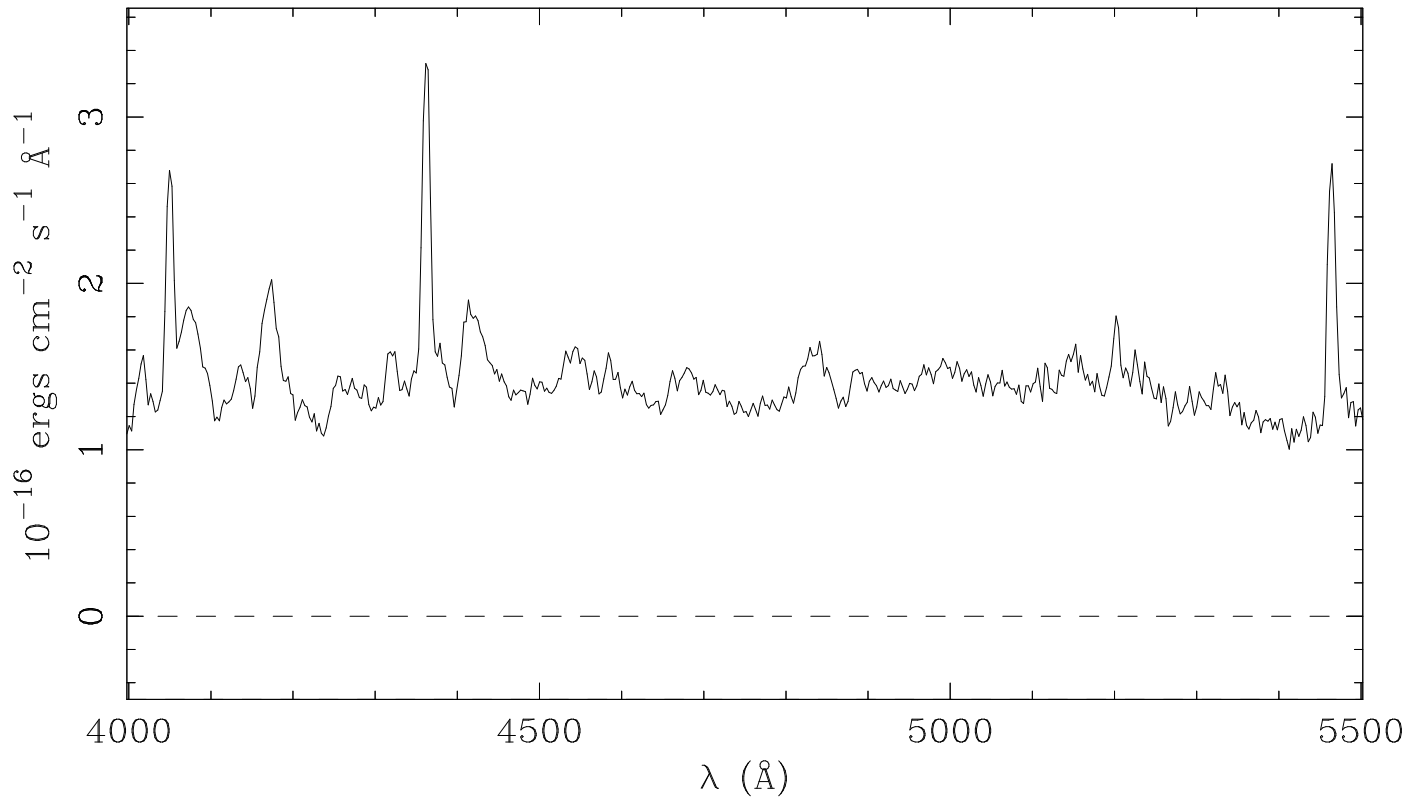
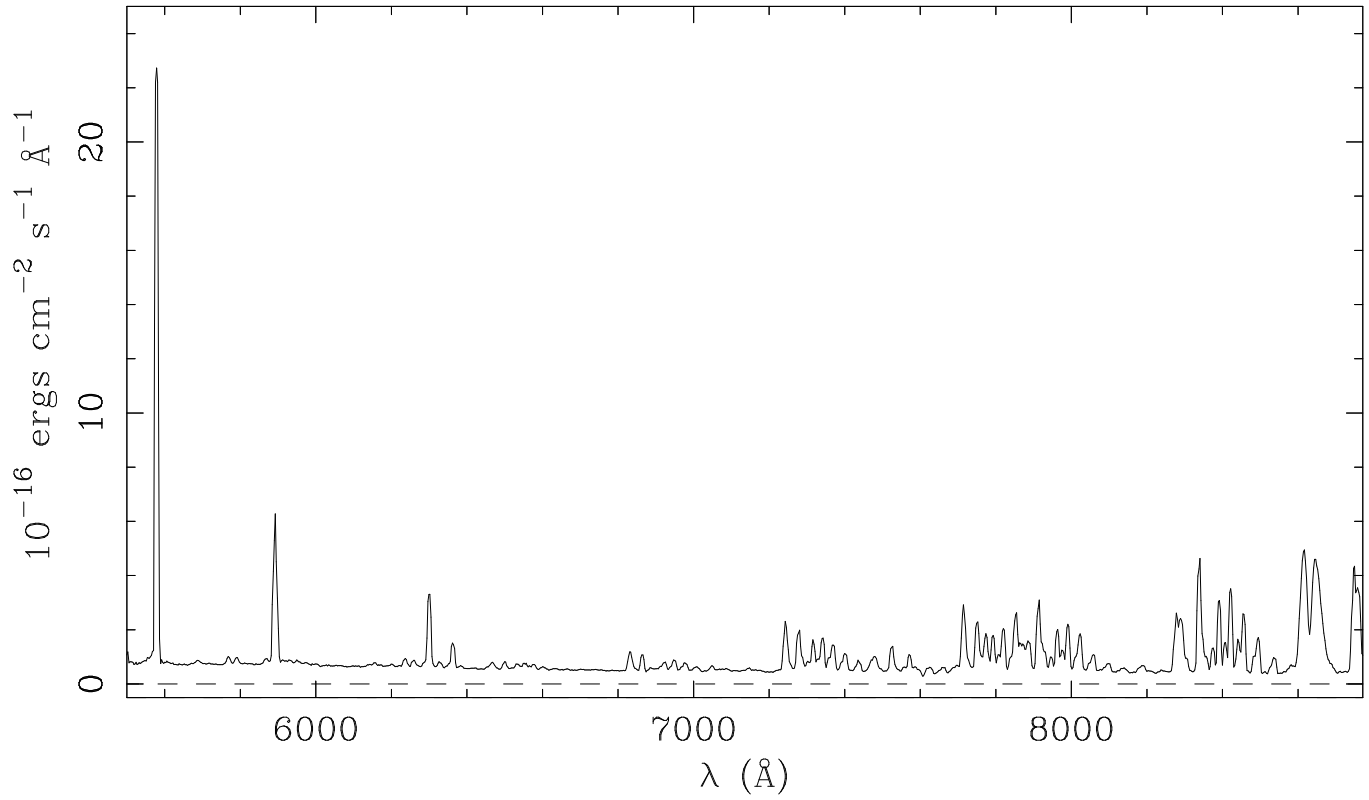
Fig. 6.— The sensitivity function, $g(z)$, of the damped Ly α absorber surveys. This gives the number of lines of sight along which a damped system at

redshift z could be detected. The APM survey adds substantial redshift path for $z > 3$.

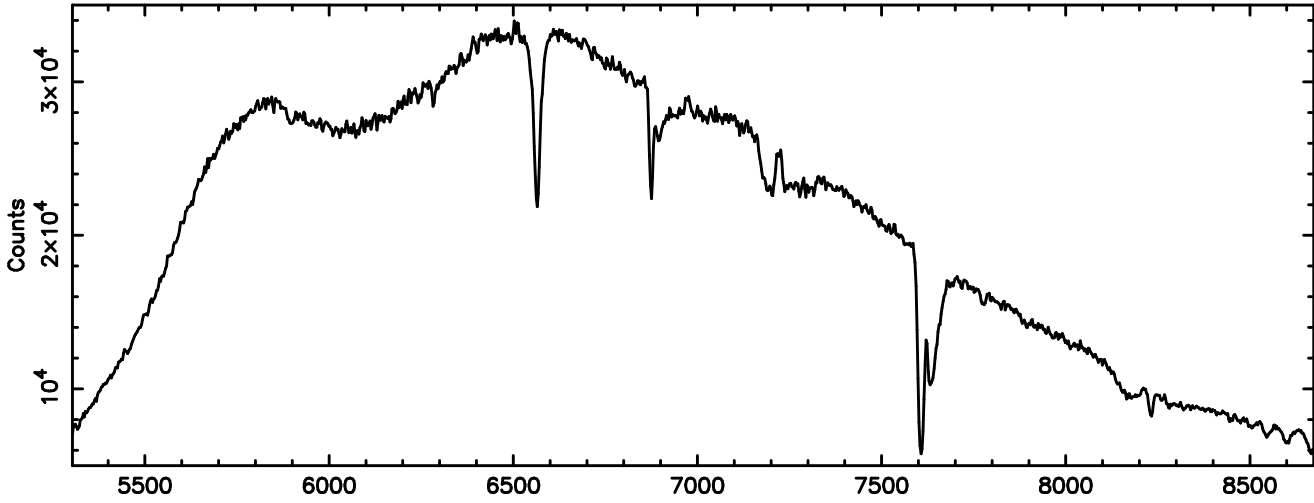
Fig. 7.— The Ly α absorbers listed in table 7 are marked with a vertical slash in the spectra in this figure. It shows the Ly α forest region on an expanded scale for the QSOs shown in figure 4 in which an absorber was measured. The damped Ly α candidates with estimated column densities above the threshold of $\log N_{\text{HI}} \geq 20.3$ have an asterisk after the column density in table 7 and a circle around the vertical slash in the figure.

Fig. 8.— Two simulated QSOs with absorbers are shown. Panels (a) and (b) show a $z = 3.86$, $\log N_{\text{HI}} = 20.69$ damped Ly α absorption system in a $z = 4.37$ QSO at 1.6Å and 6Å resolution, respectively, with a signal-to-noise ratio of 25. Panels (c) and (d) show a $z = 3.73$, $\log N_{\text{HI}} = 20.15$ Ly α absorption system in a $z = 4.51$ QSO at 1.6Å and 6Å resolution, respectively, with a signal-to-noise ratio of 10.

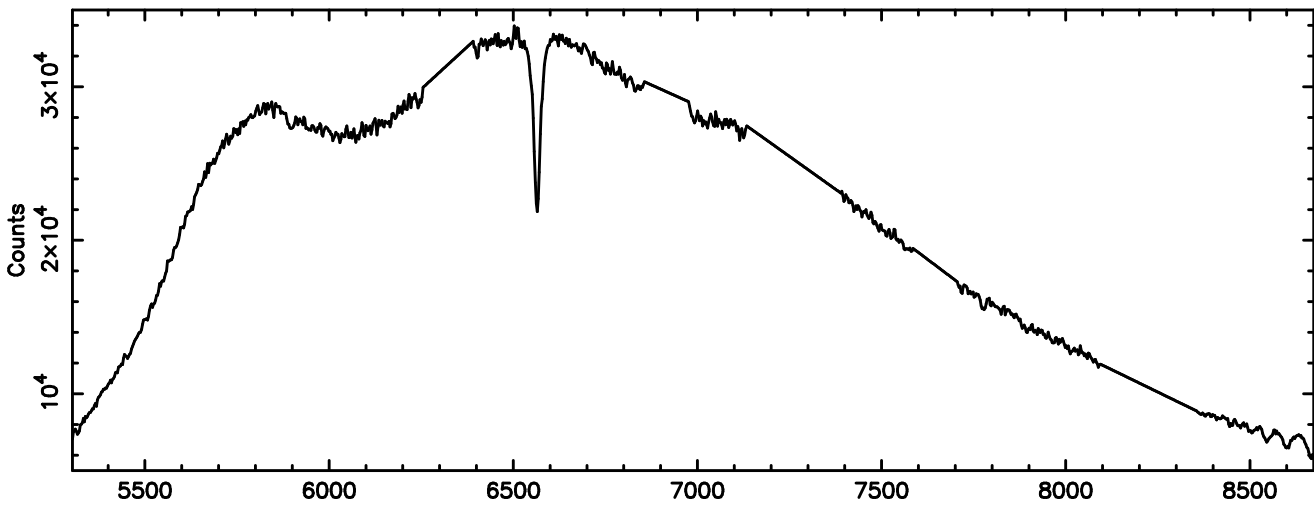
Dark Sky Spectrum – ISIS



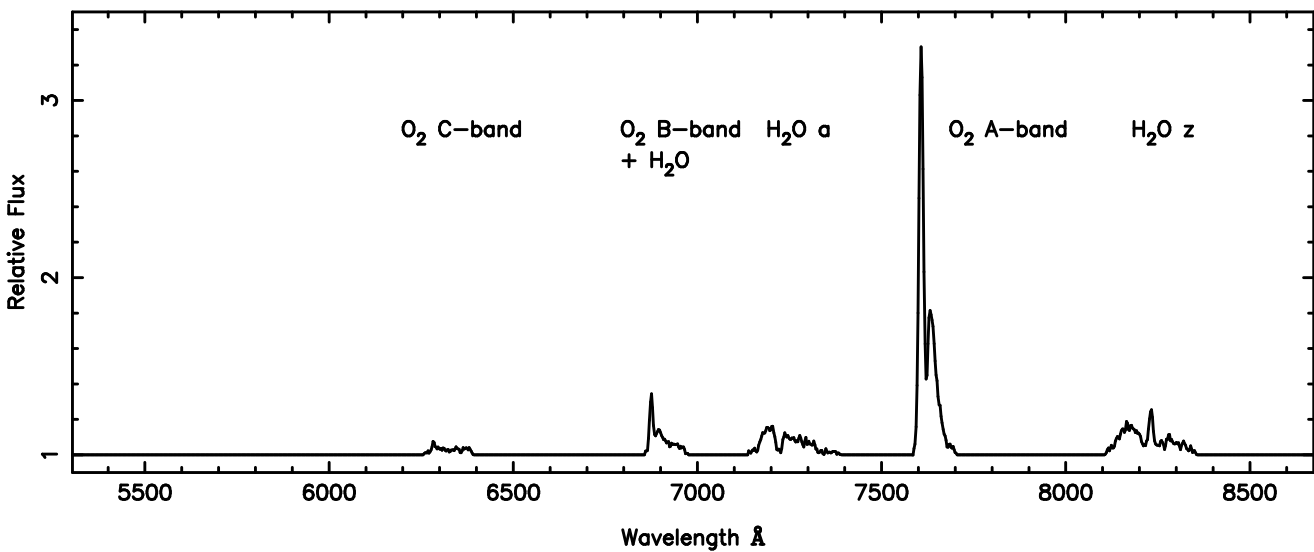
(a) B-star spectrum -- airmass=1.056



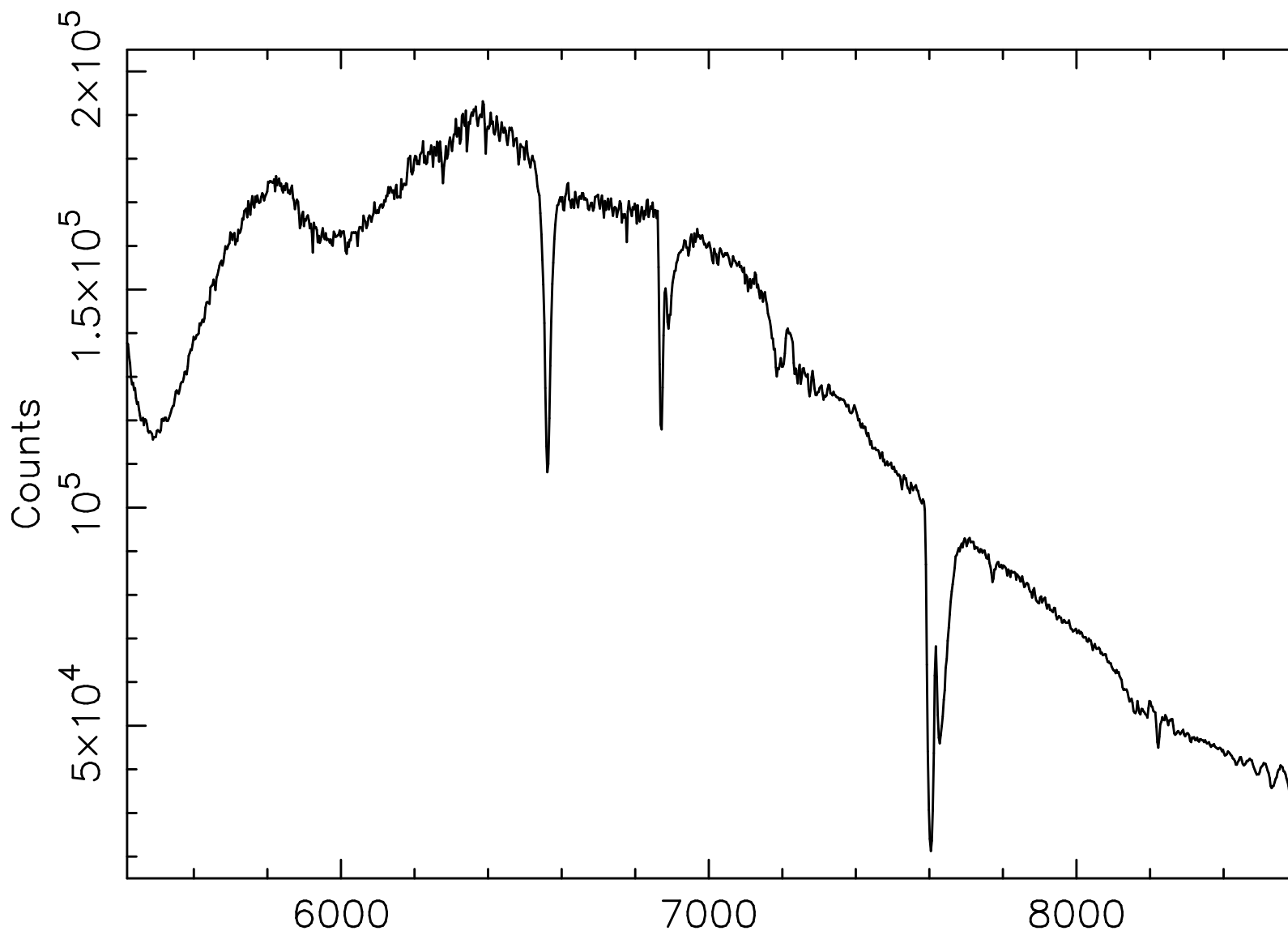
(b) atmospheric absorption features removed

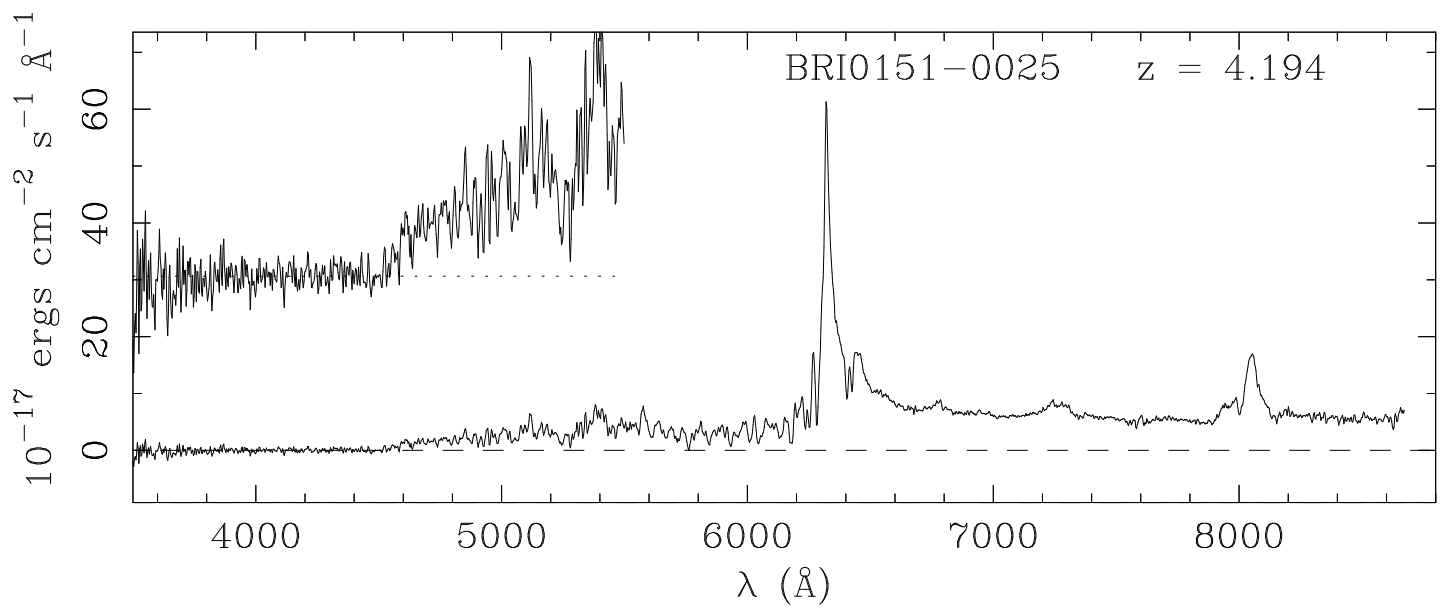
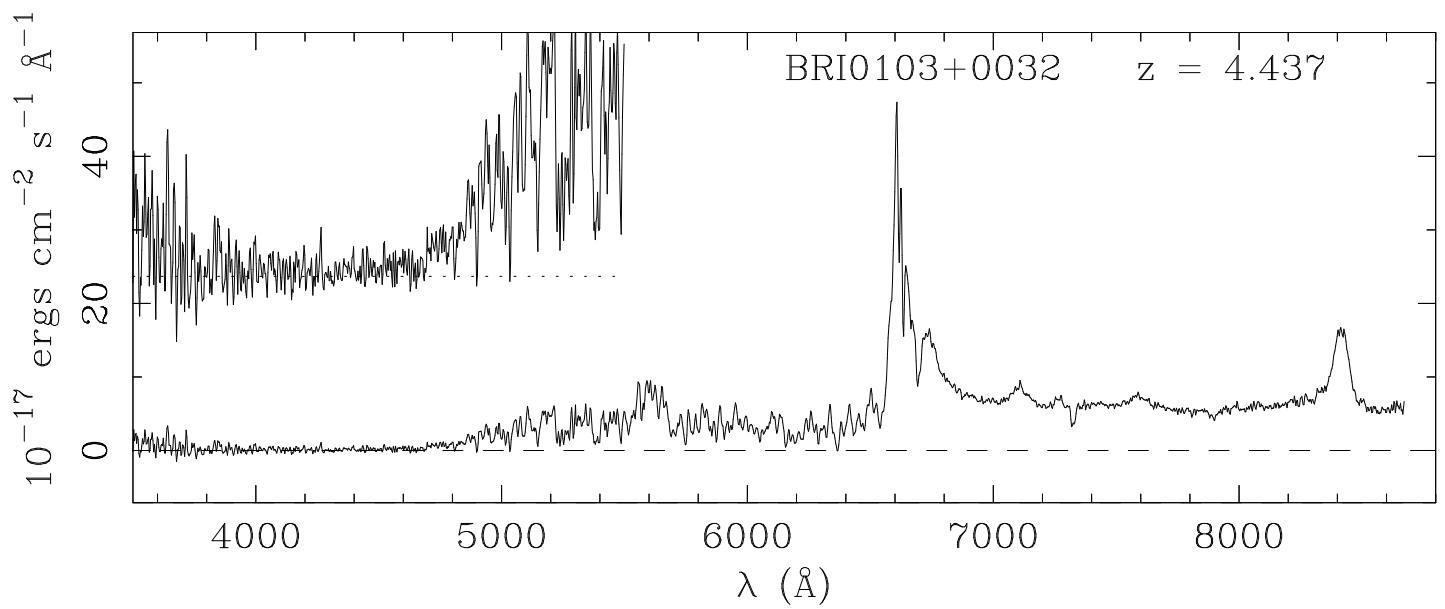
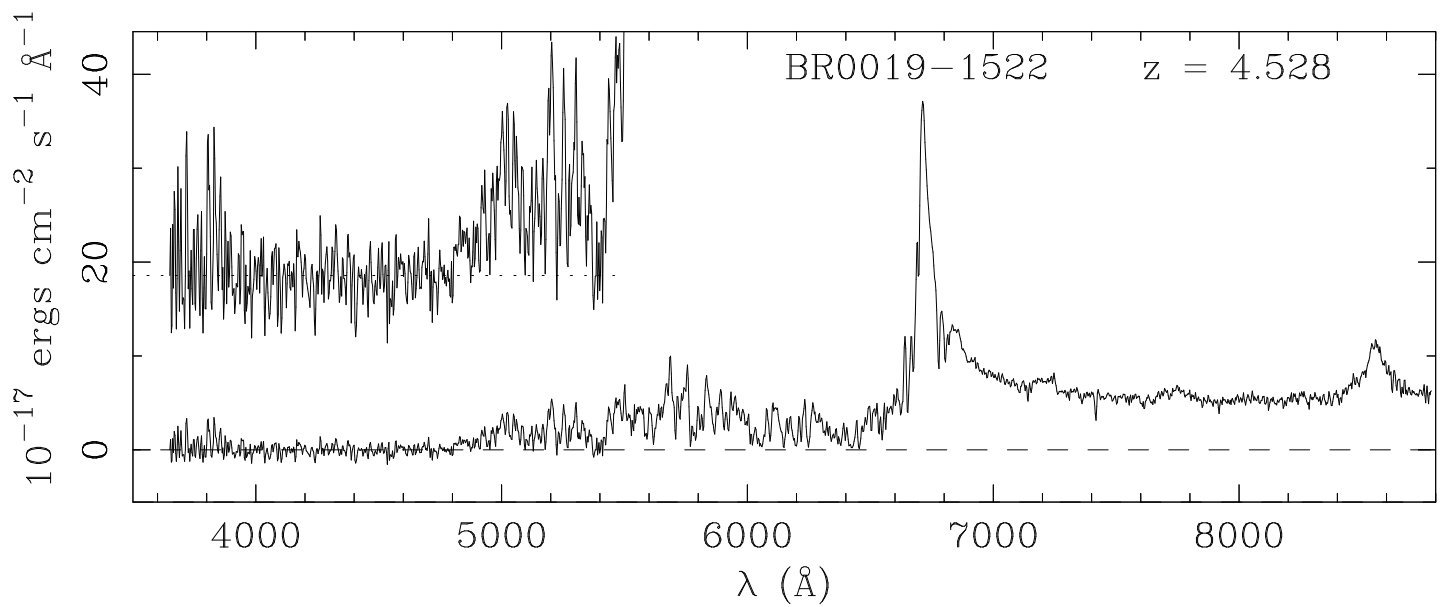


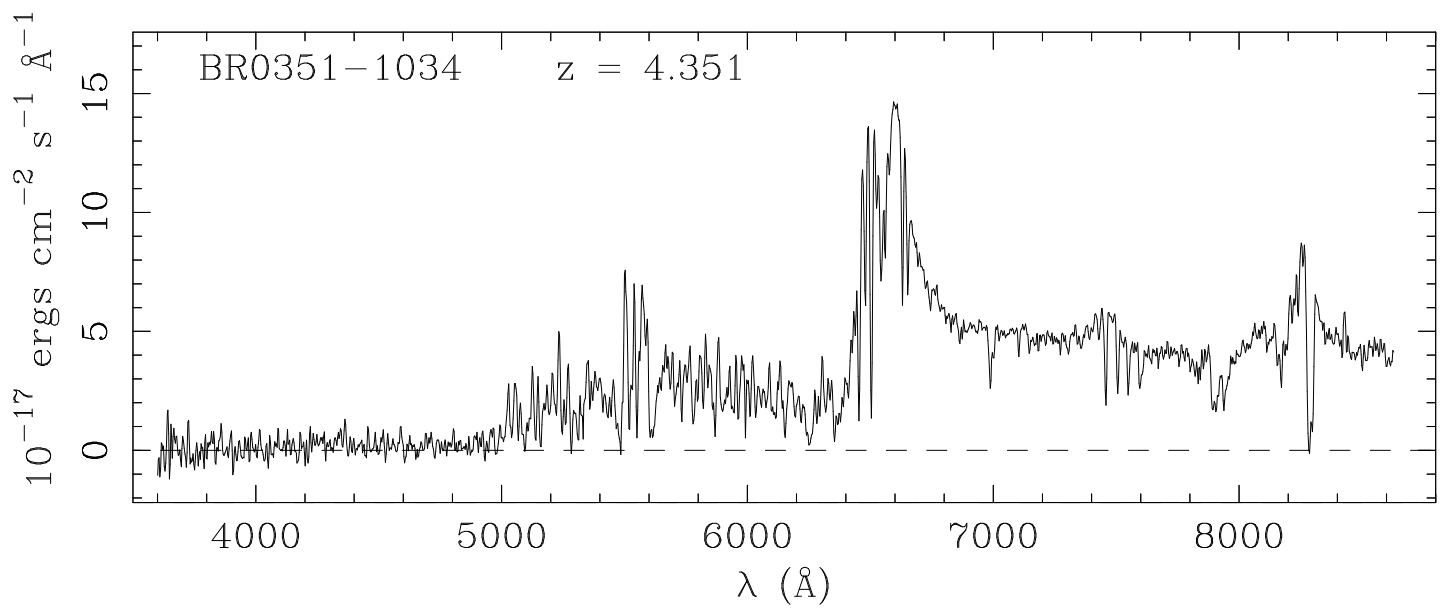
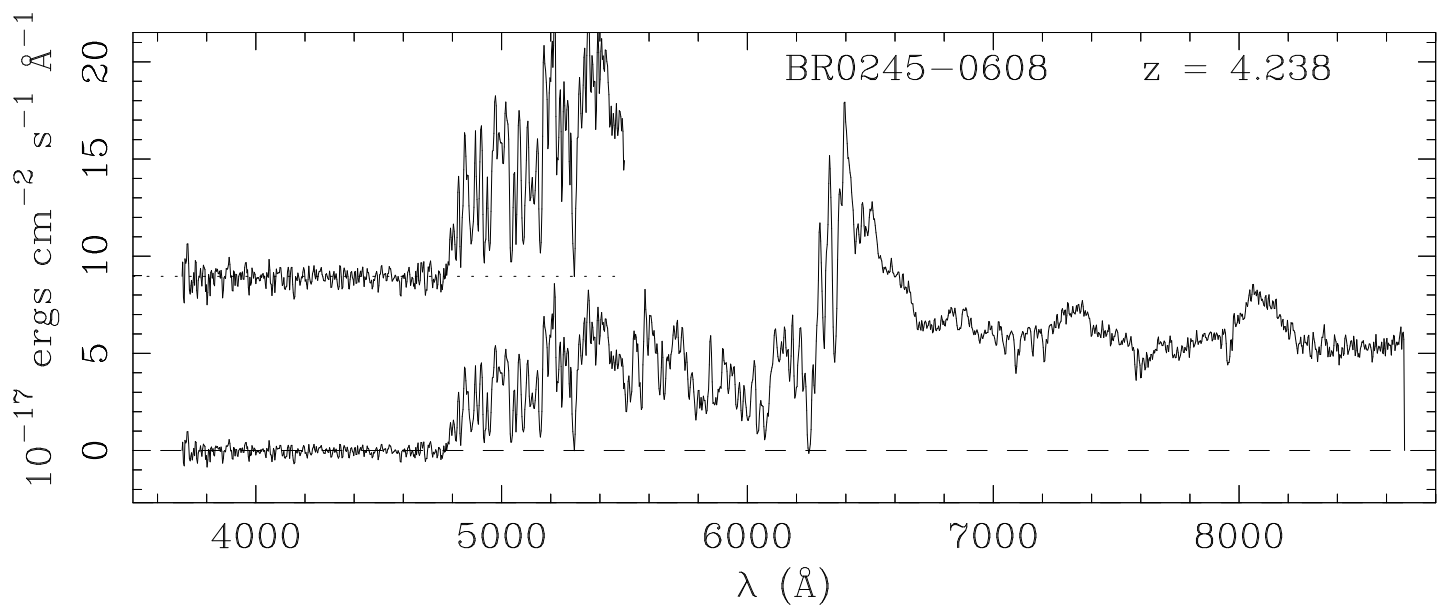
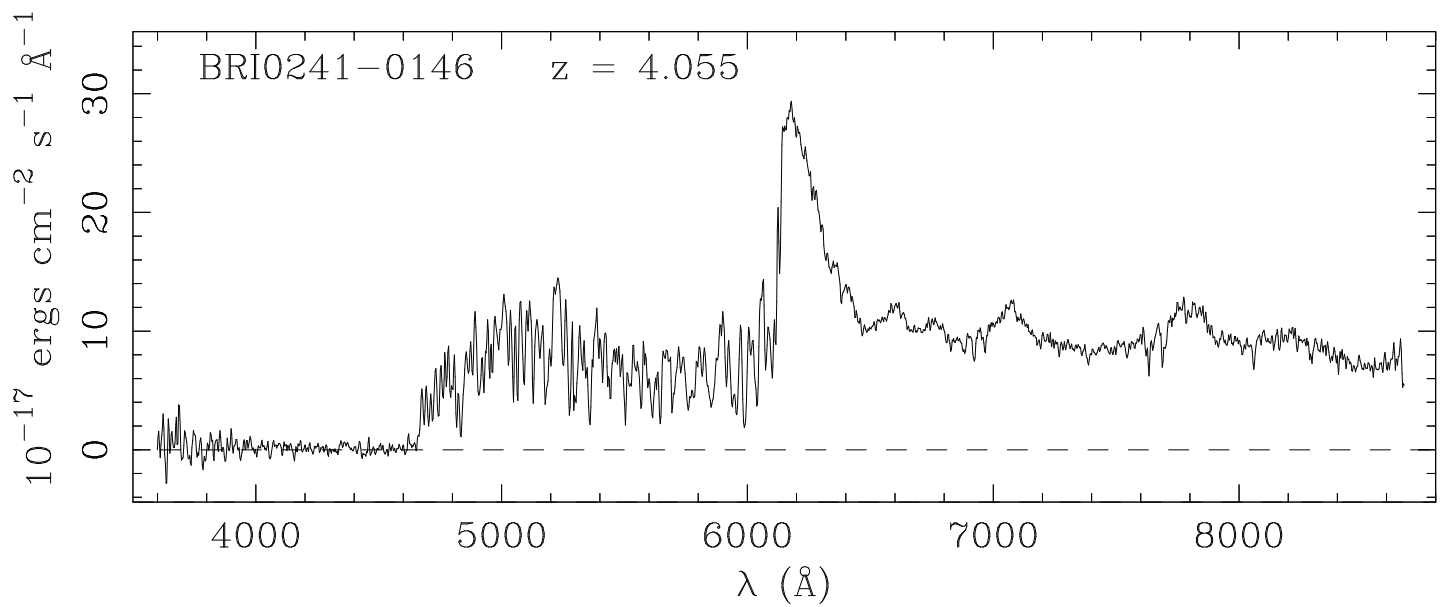
(c) inverted atmospheric absorption spectrum

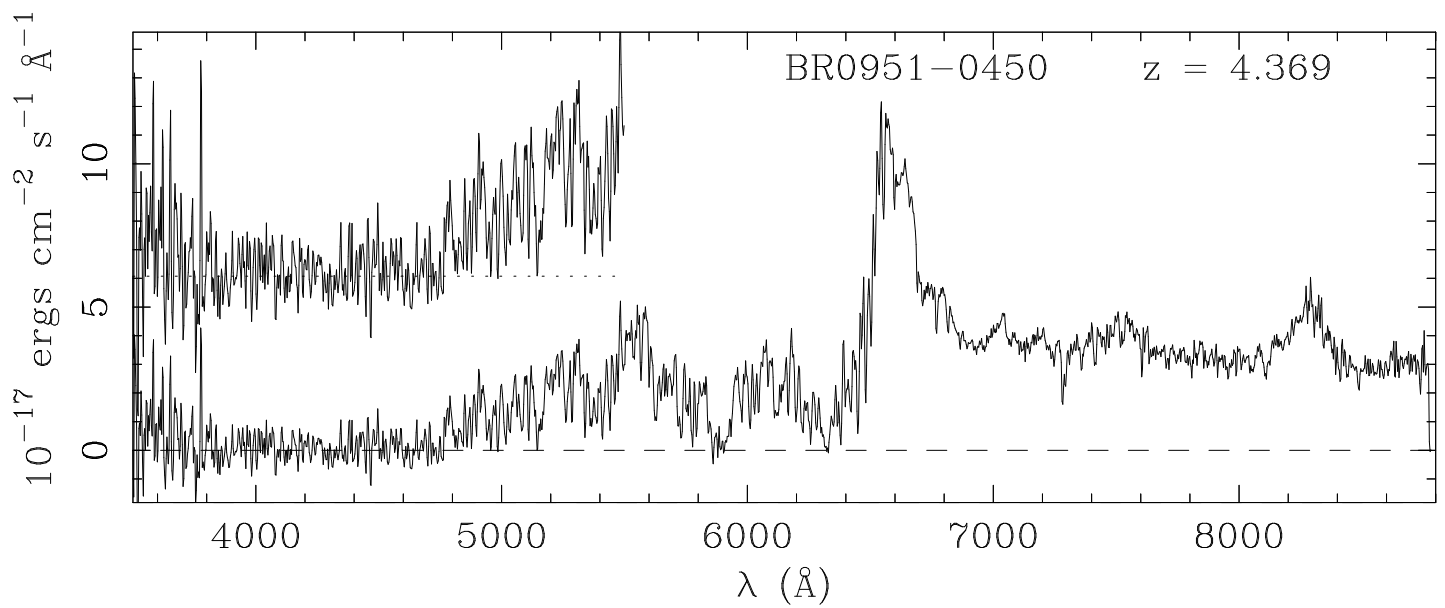
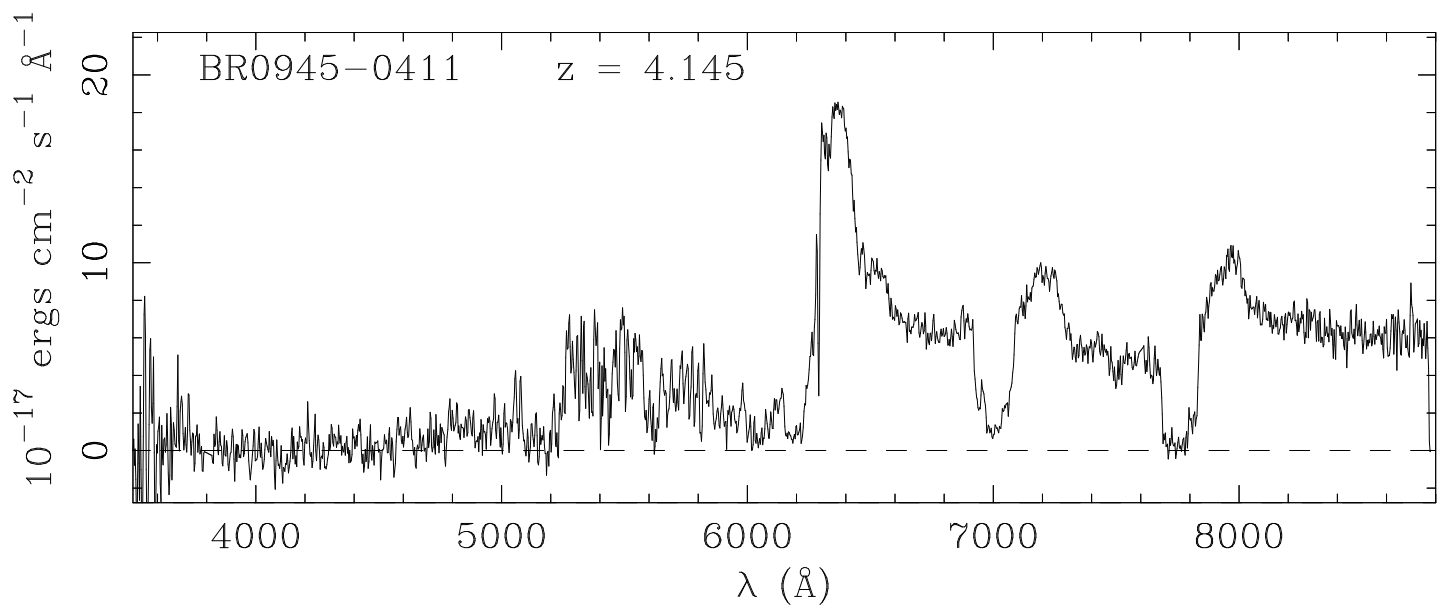
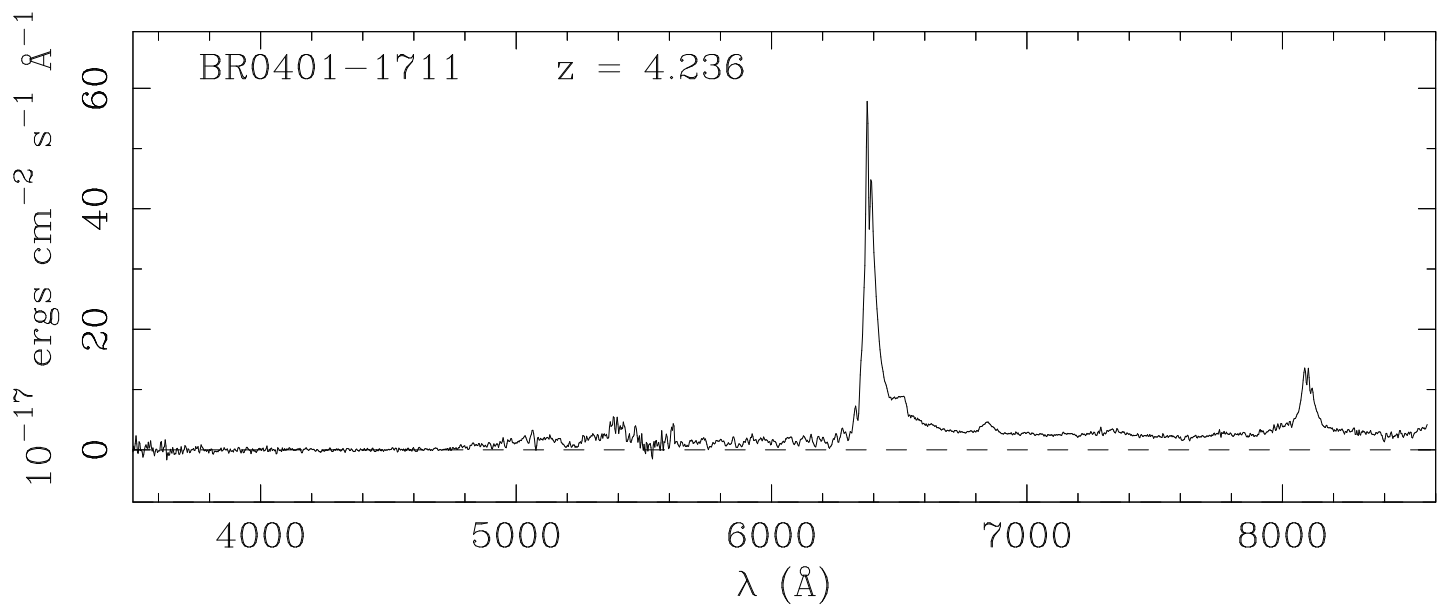


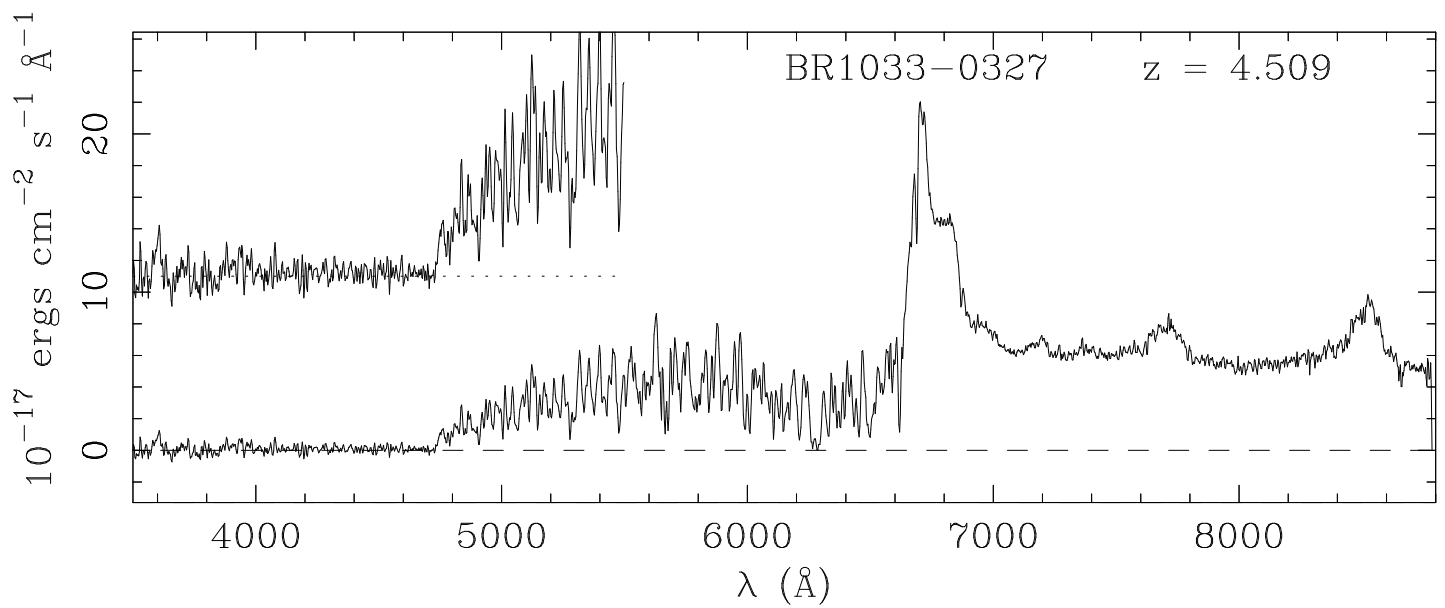
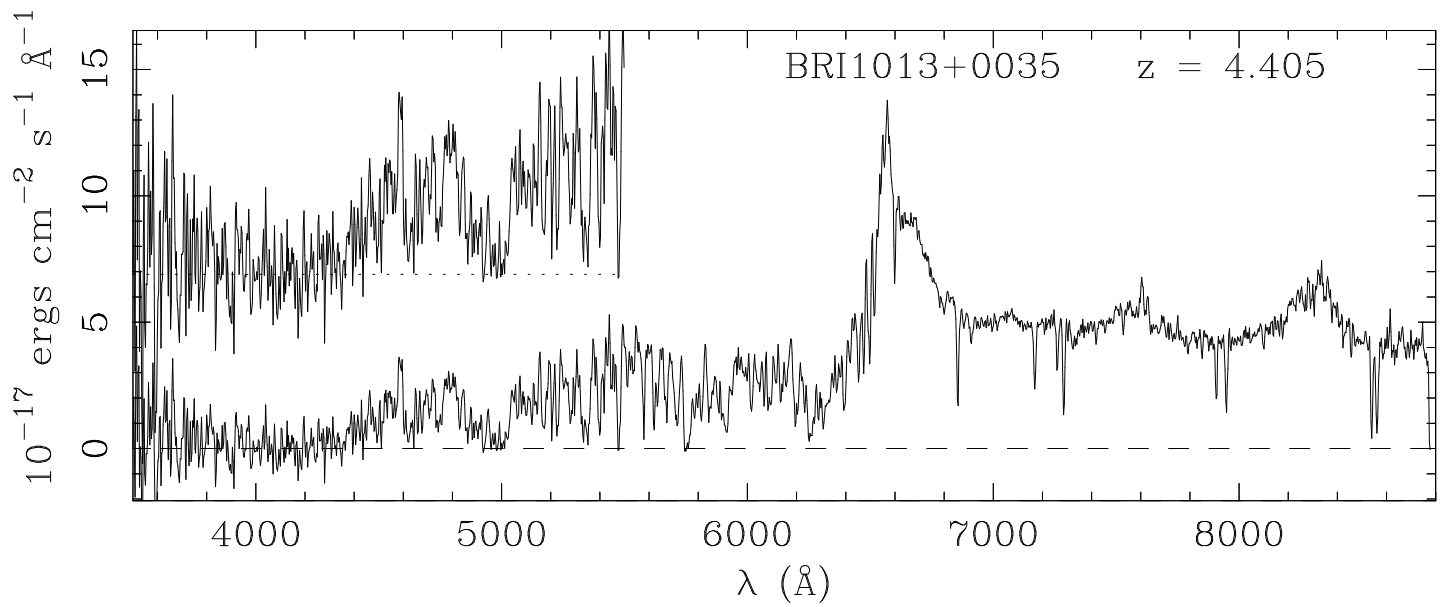
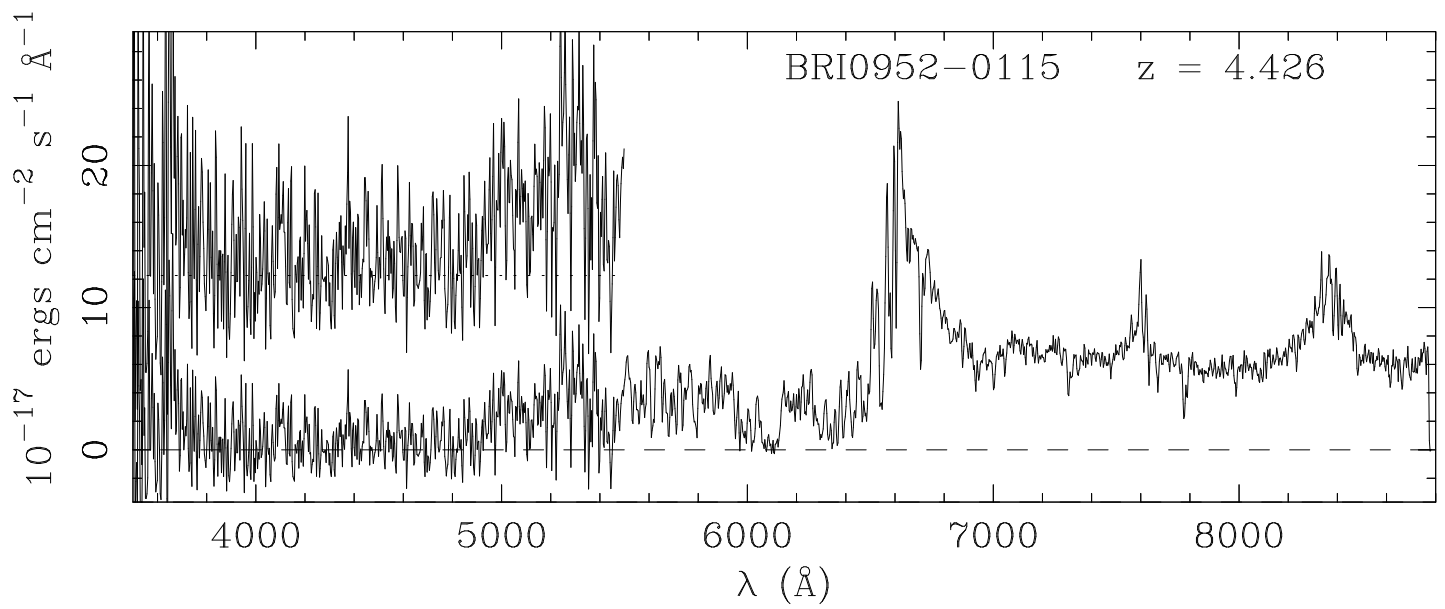
(a) B-star spectrum -- airmass=1.48

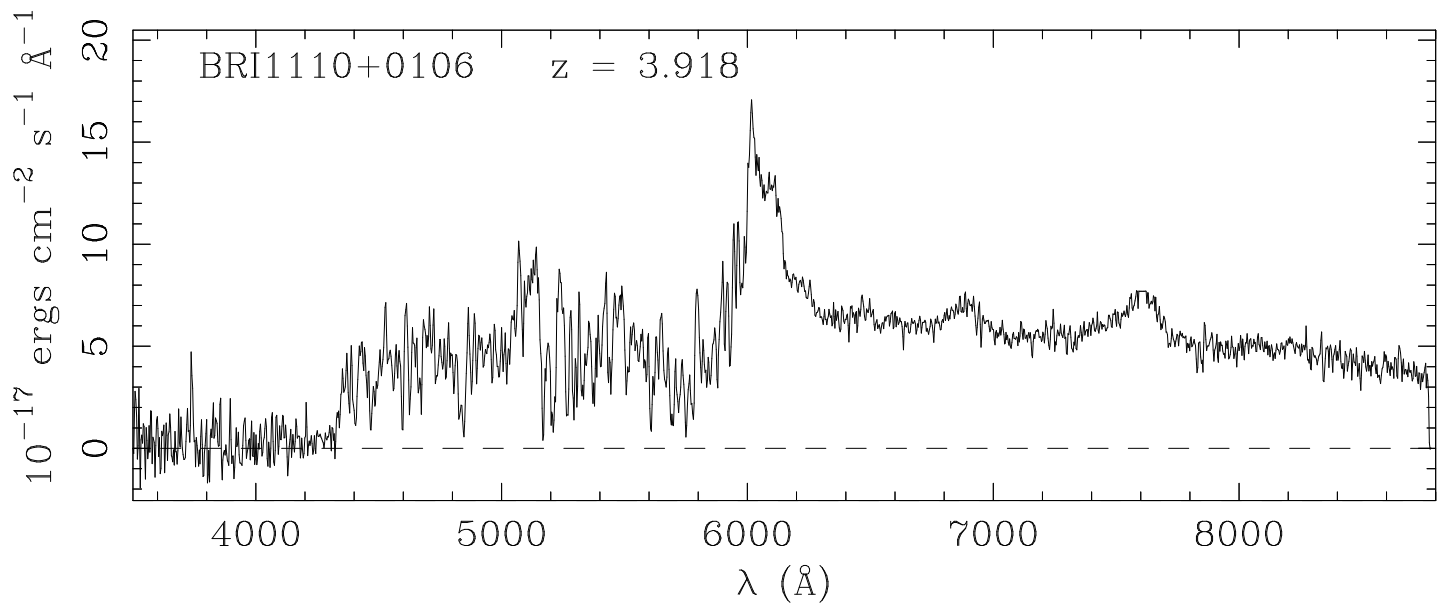
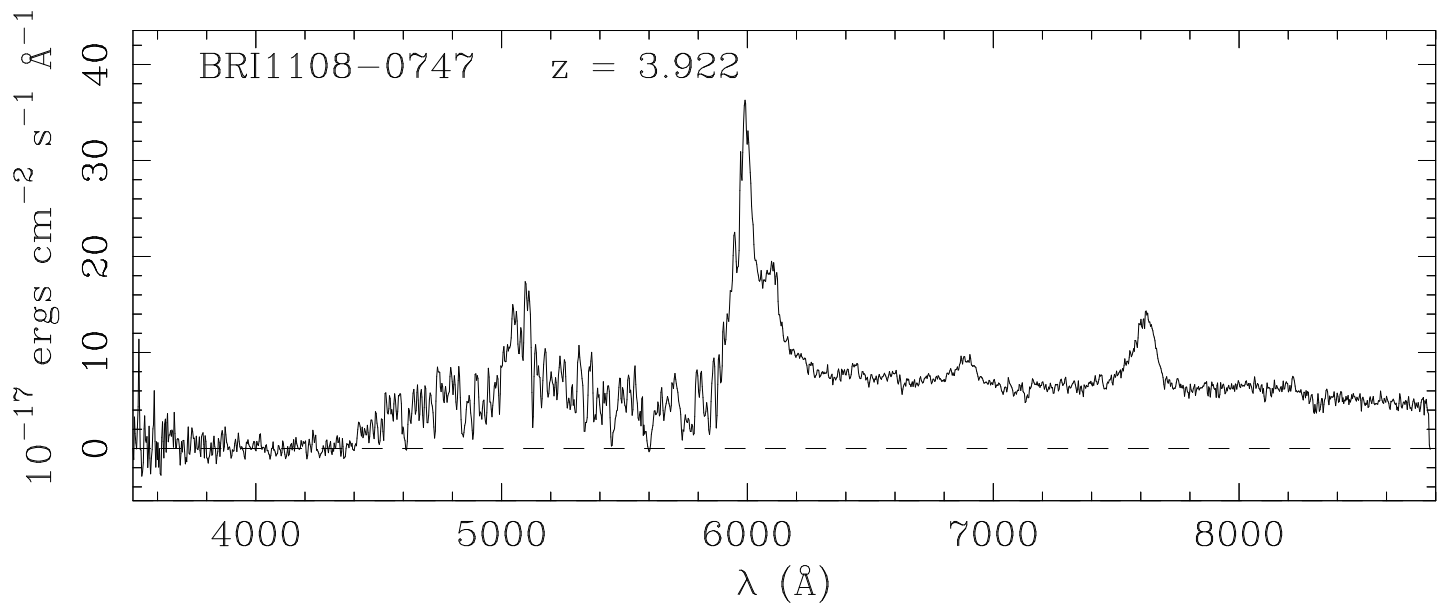
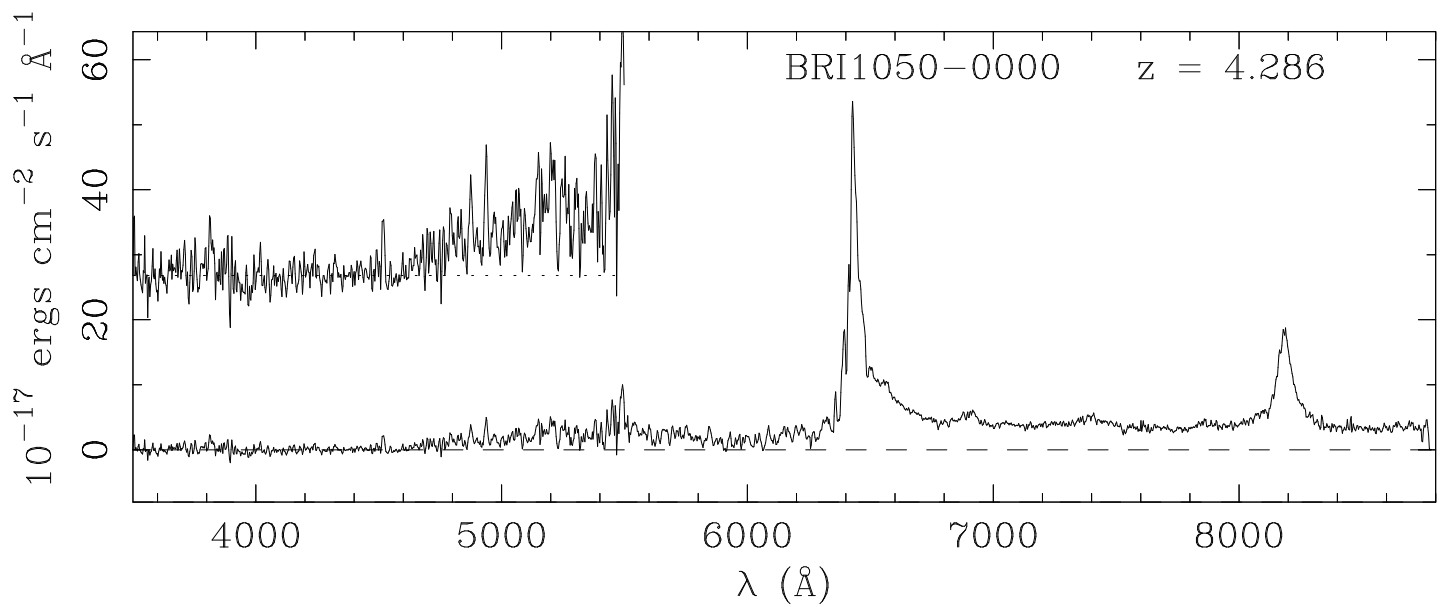


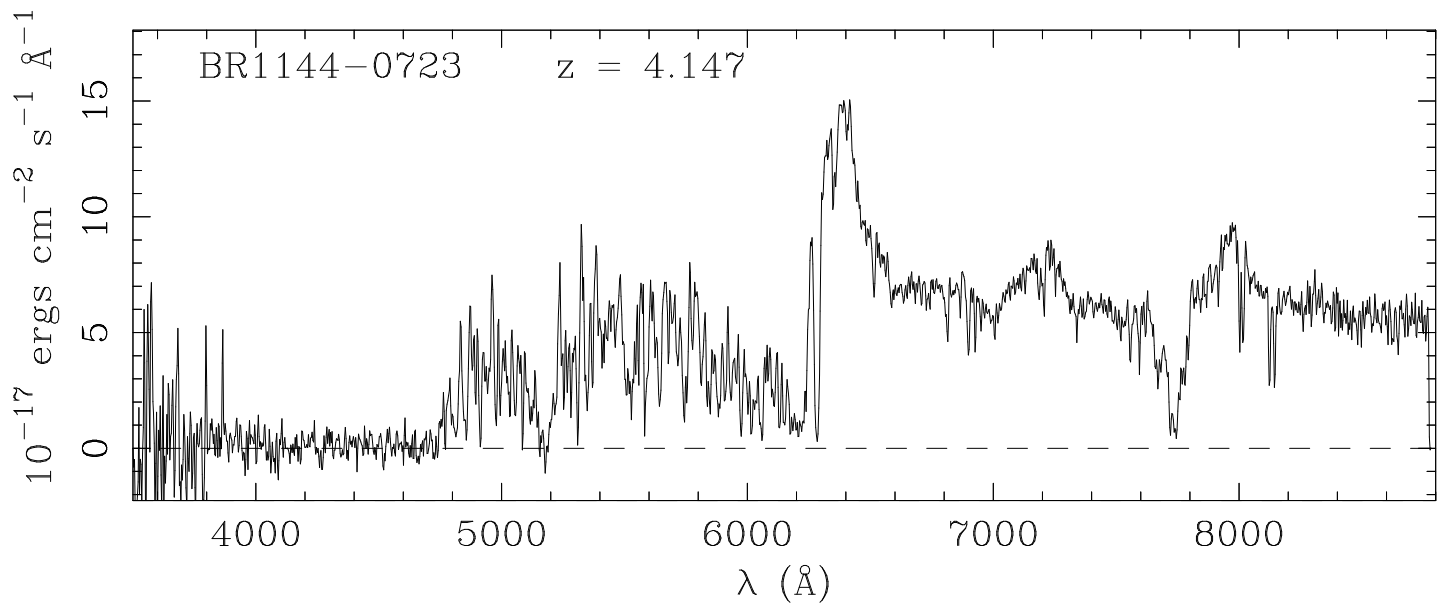
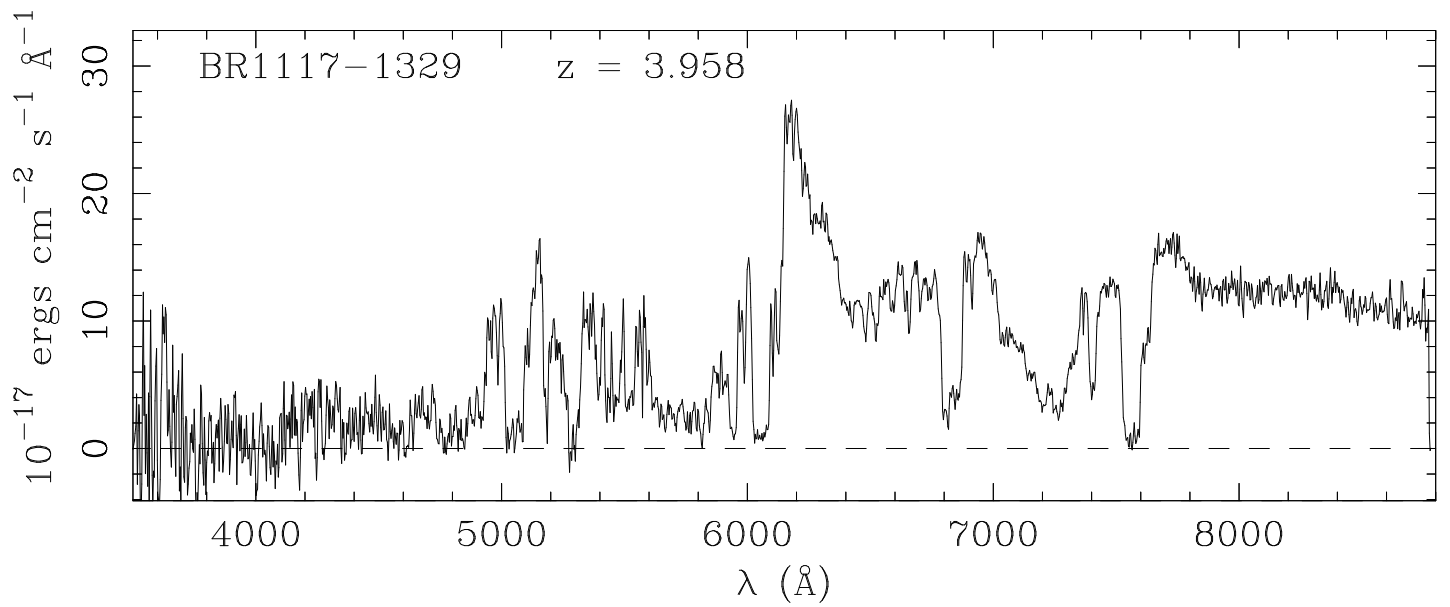
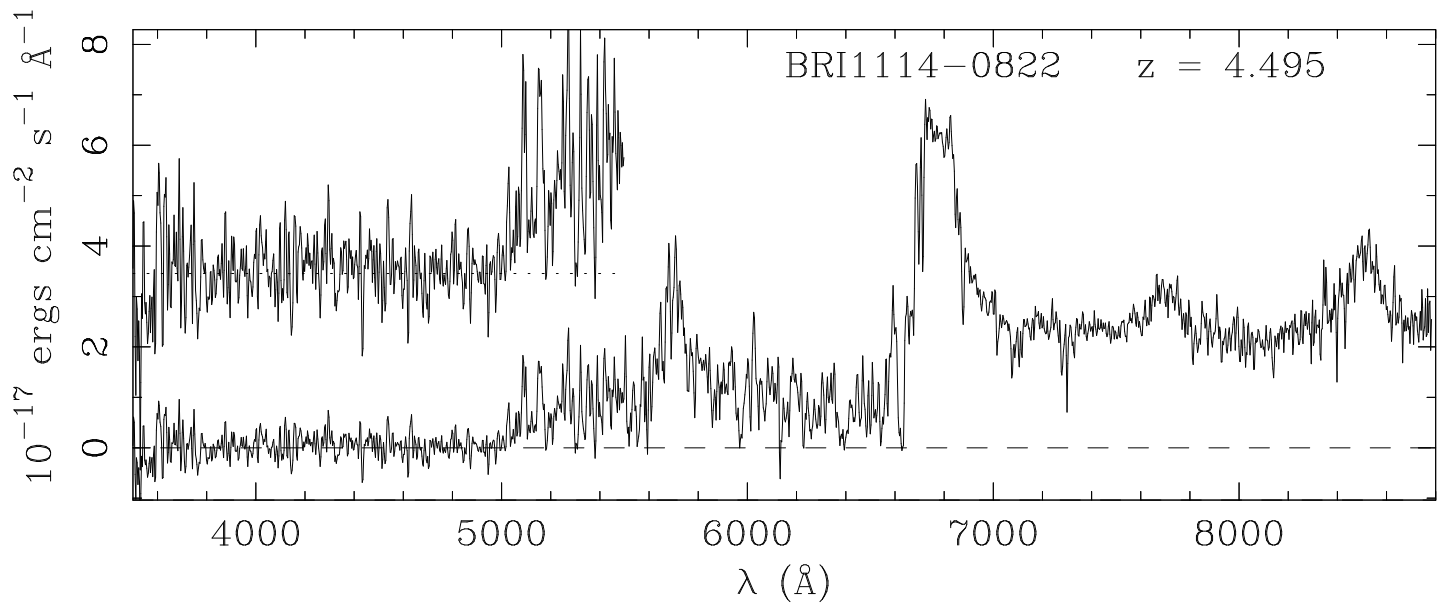


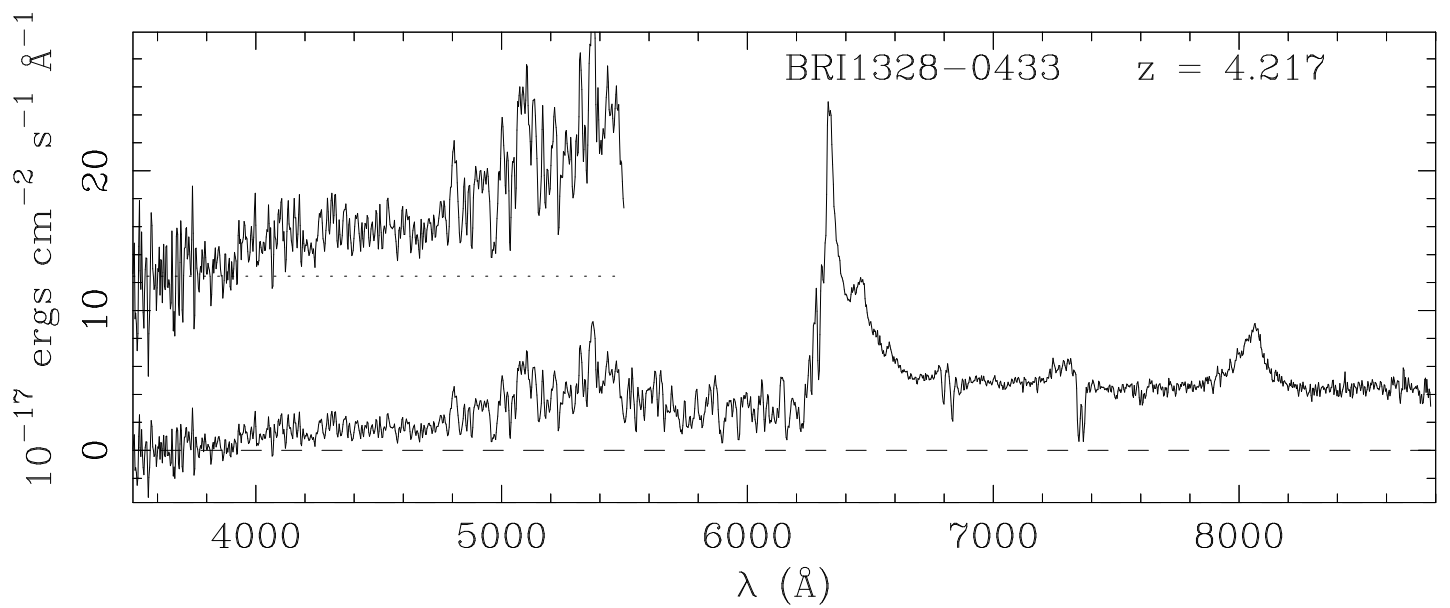
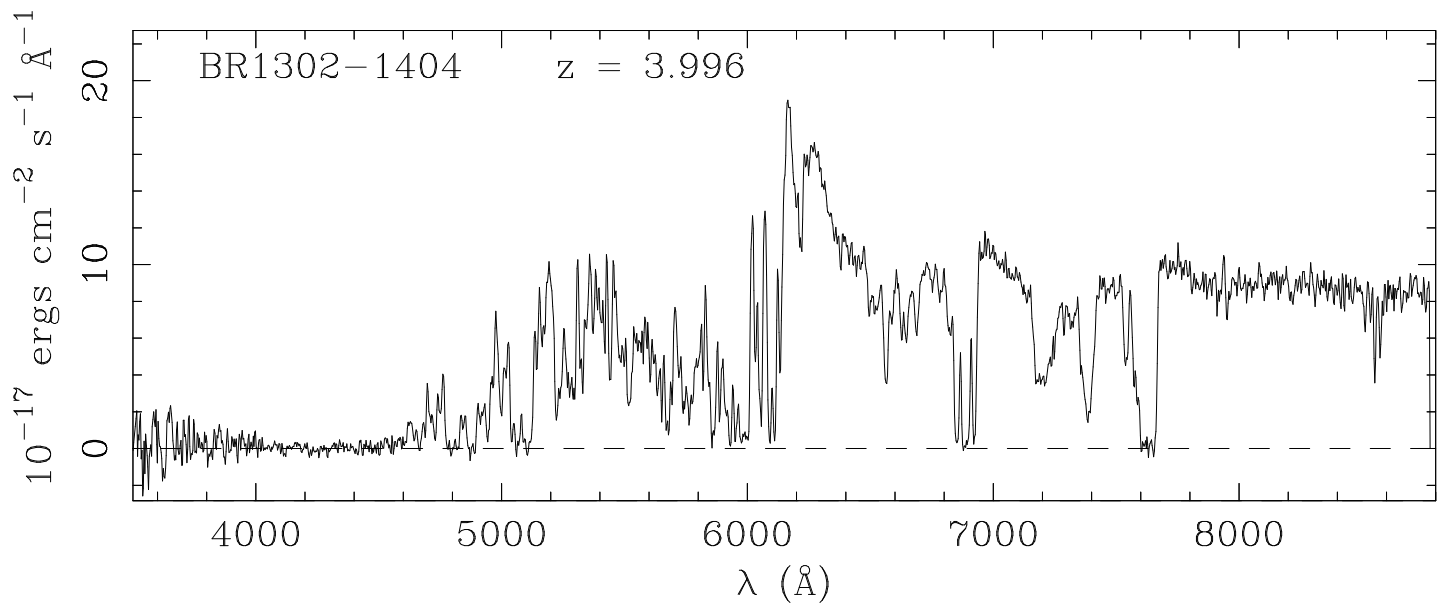
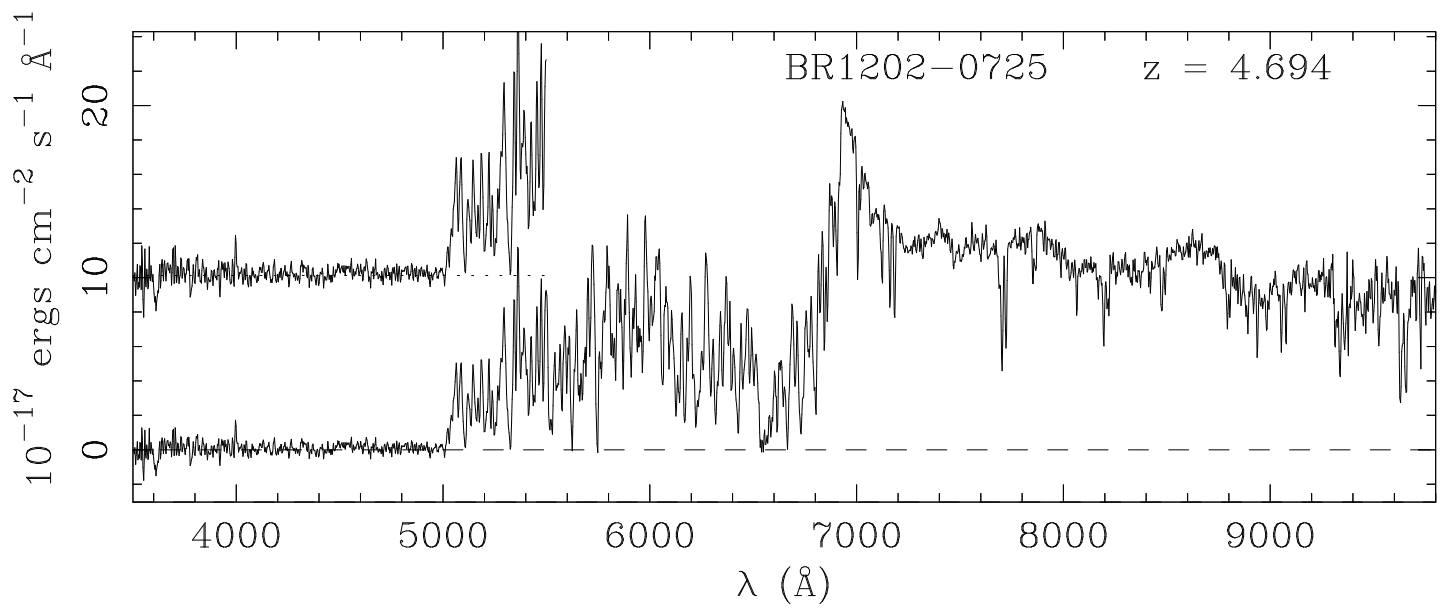


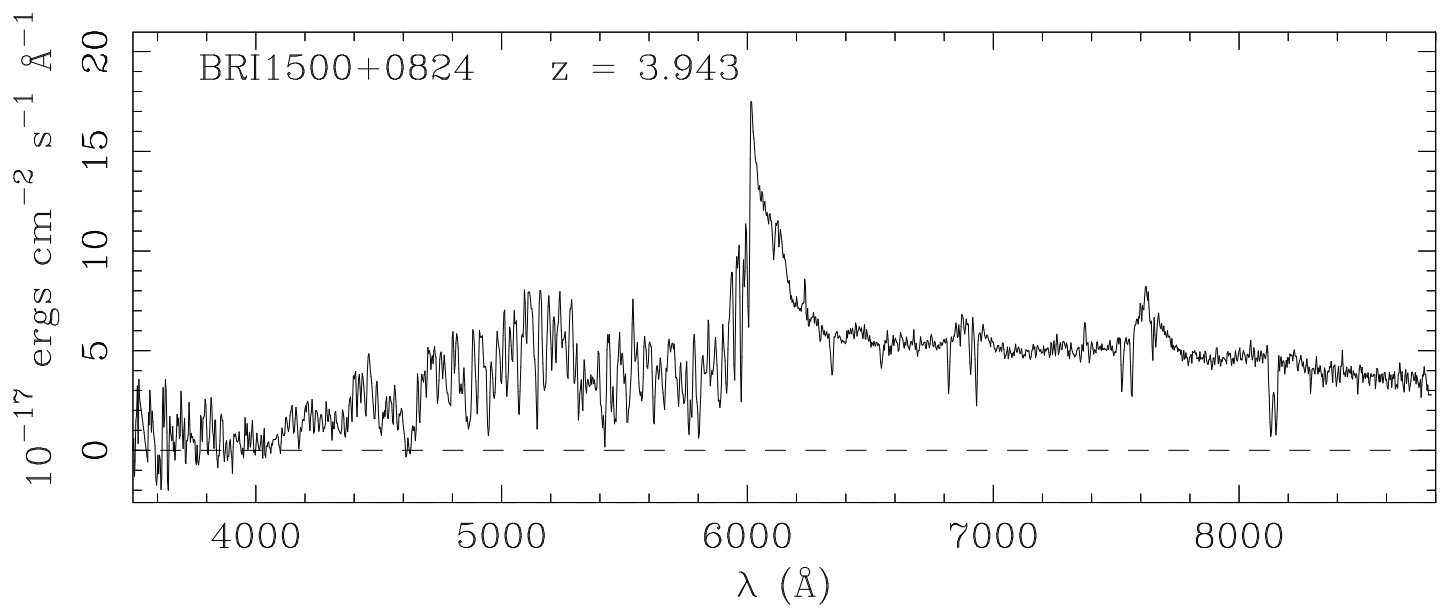
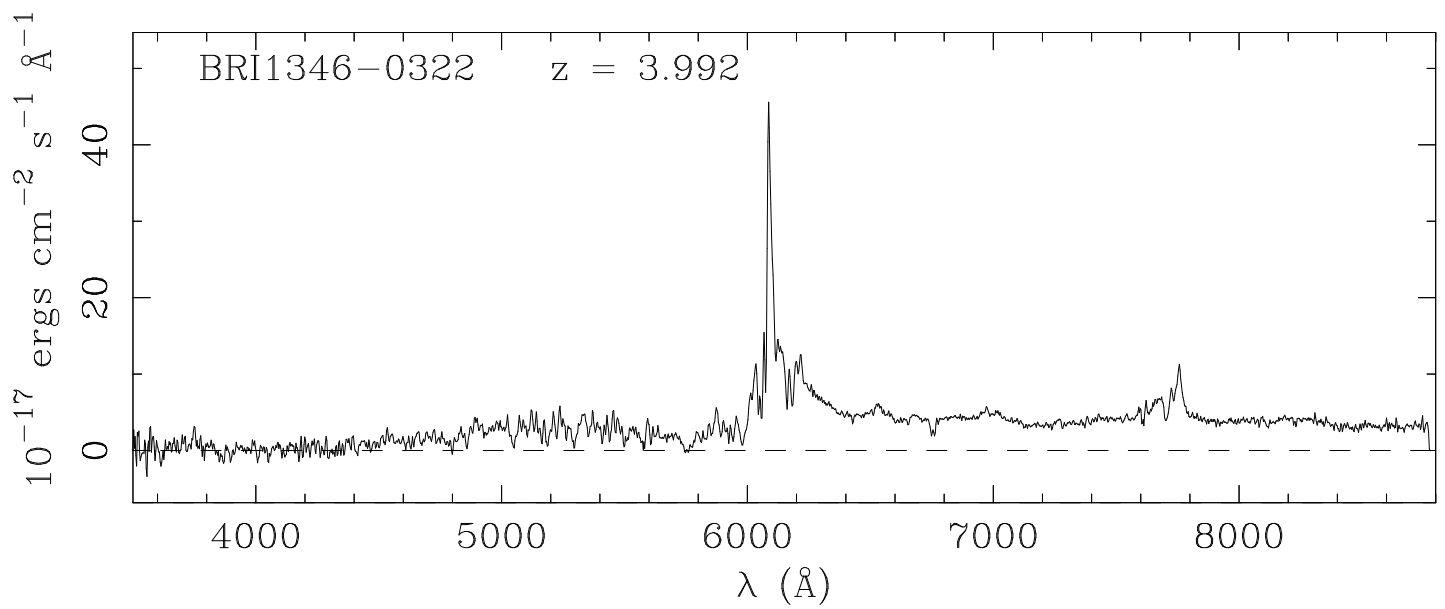
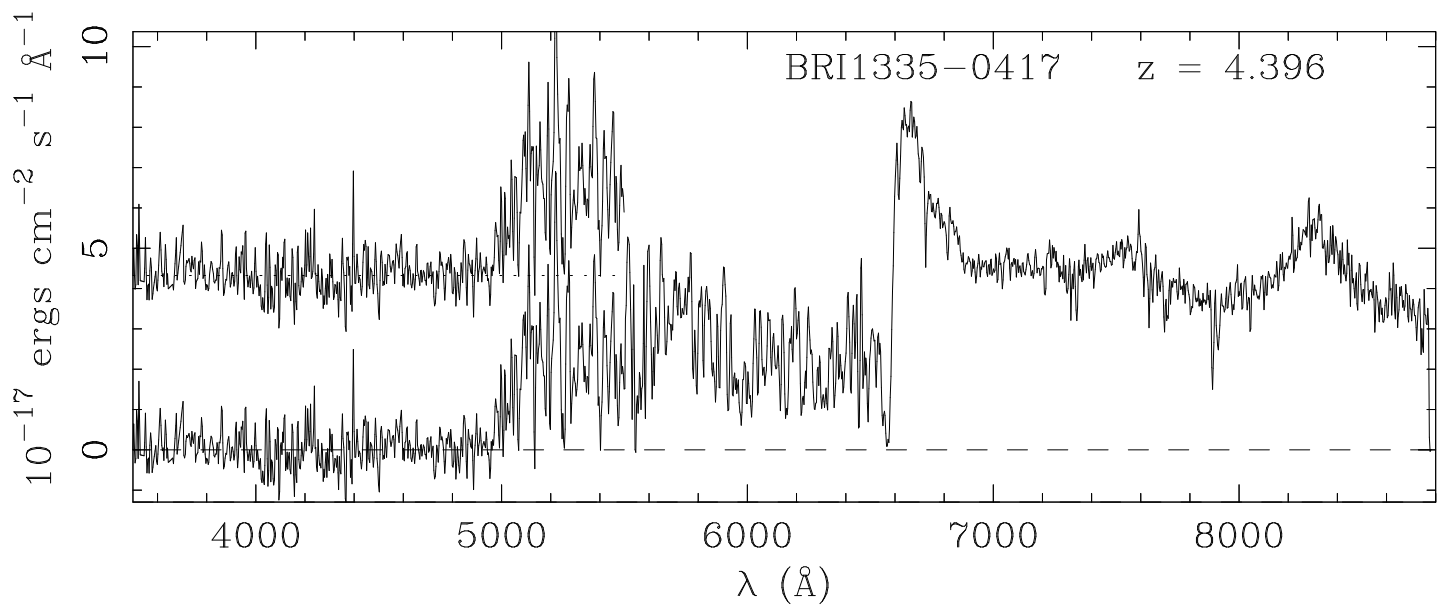


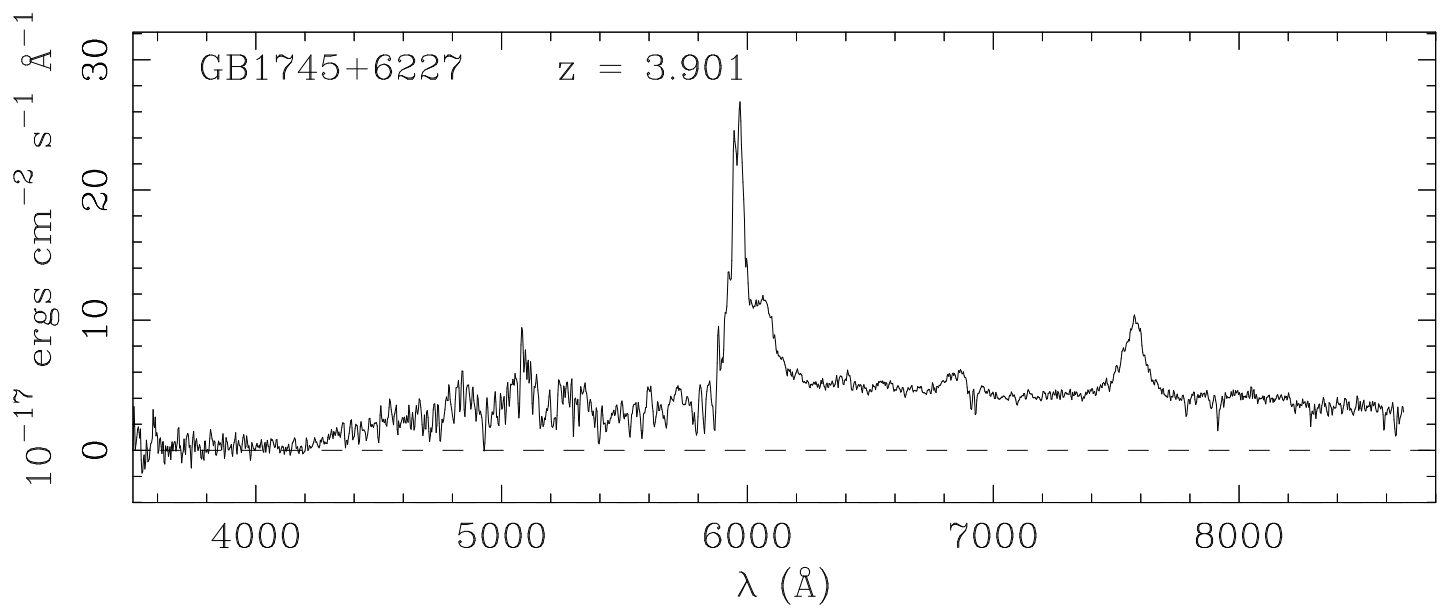
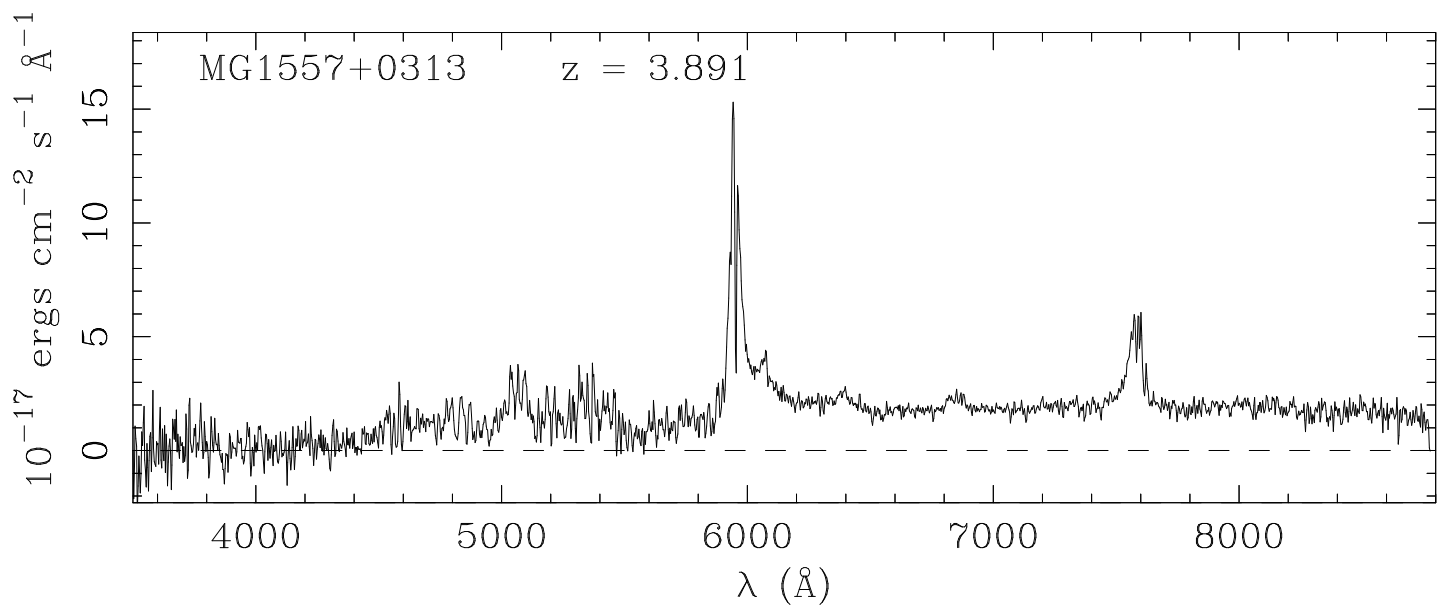
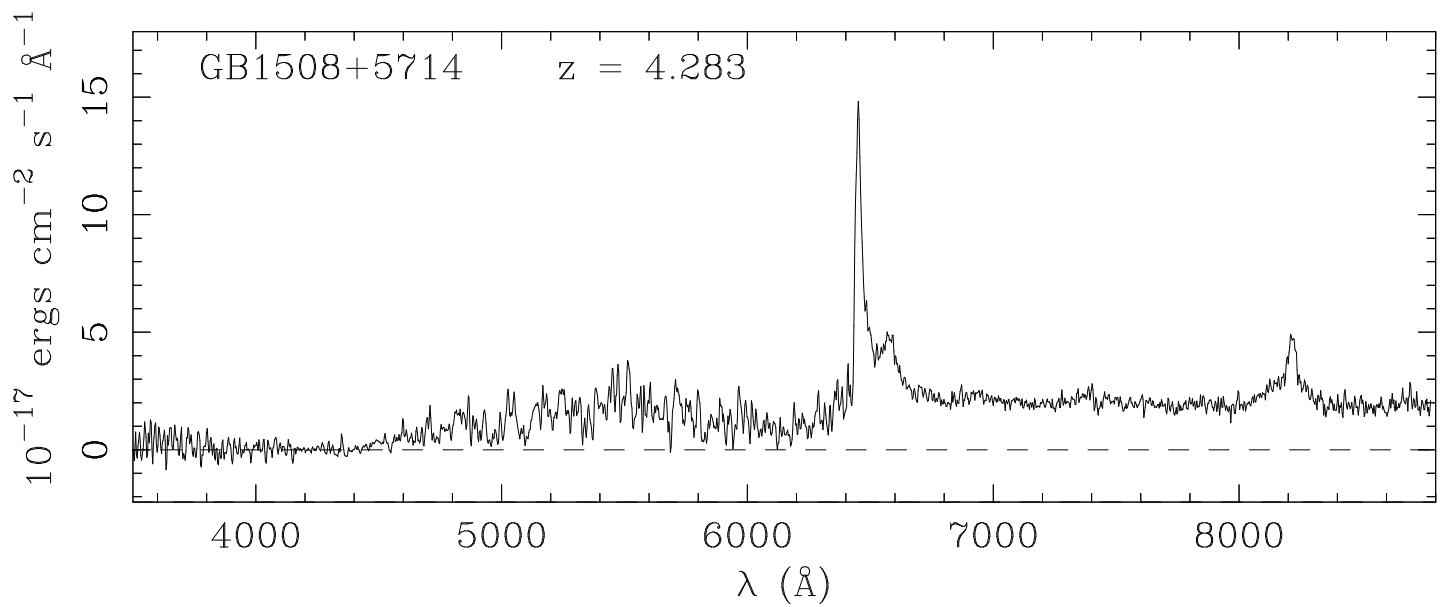


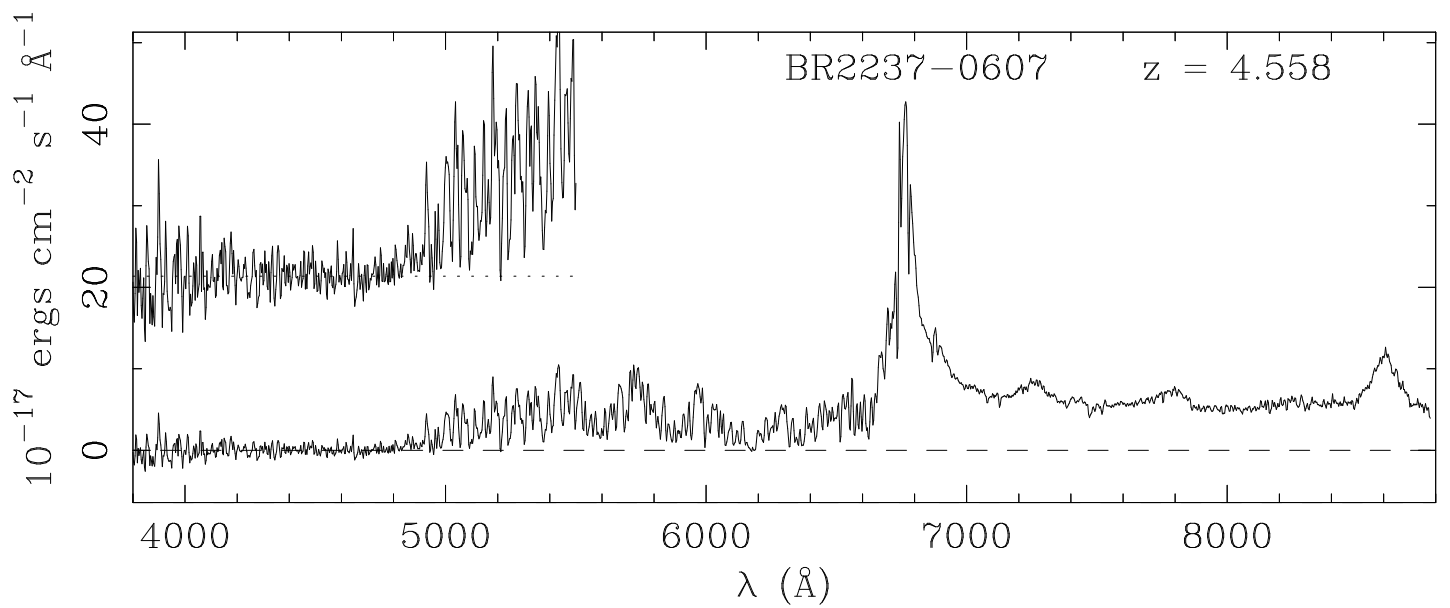
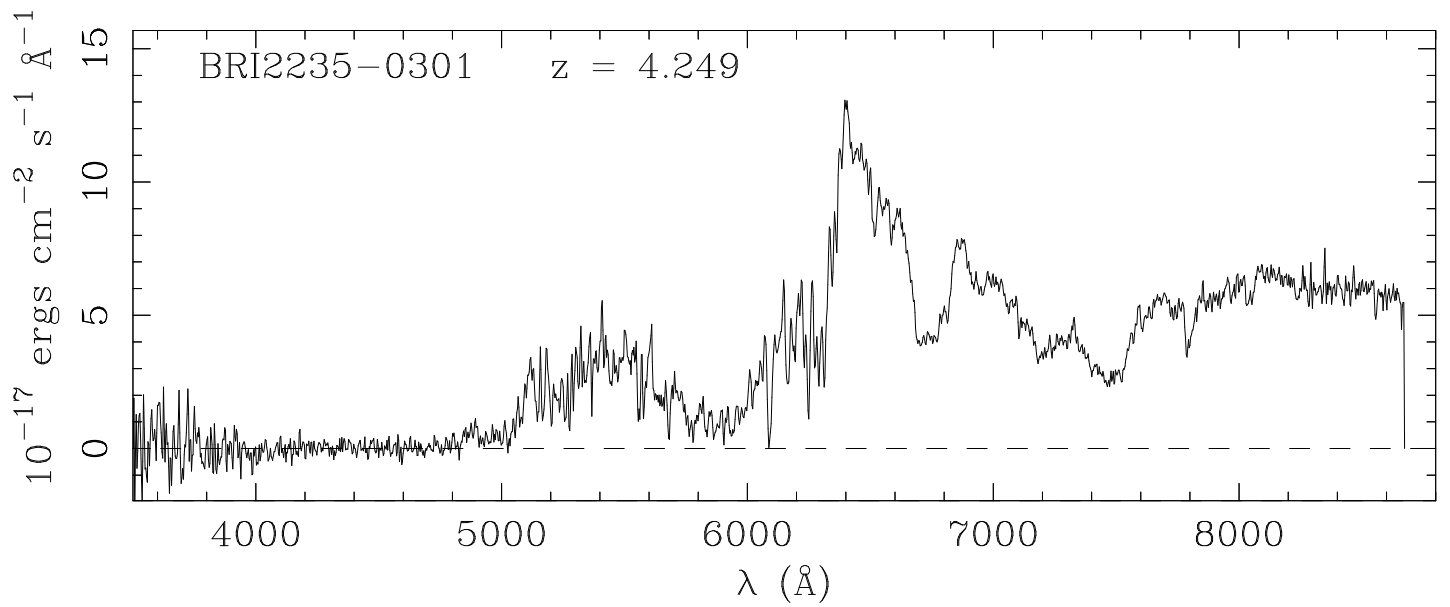
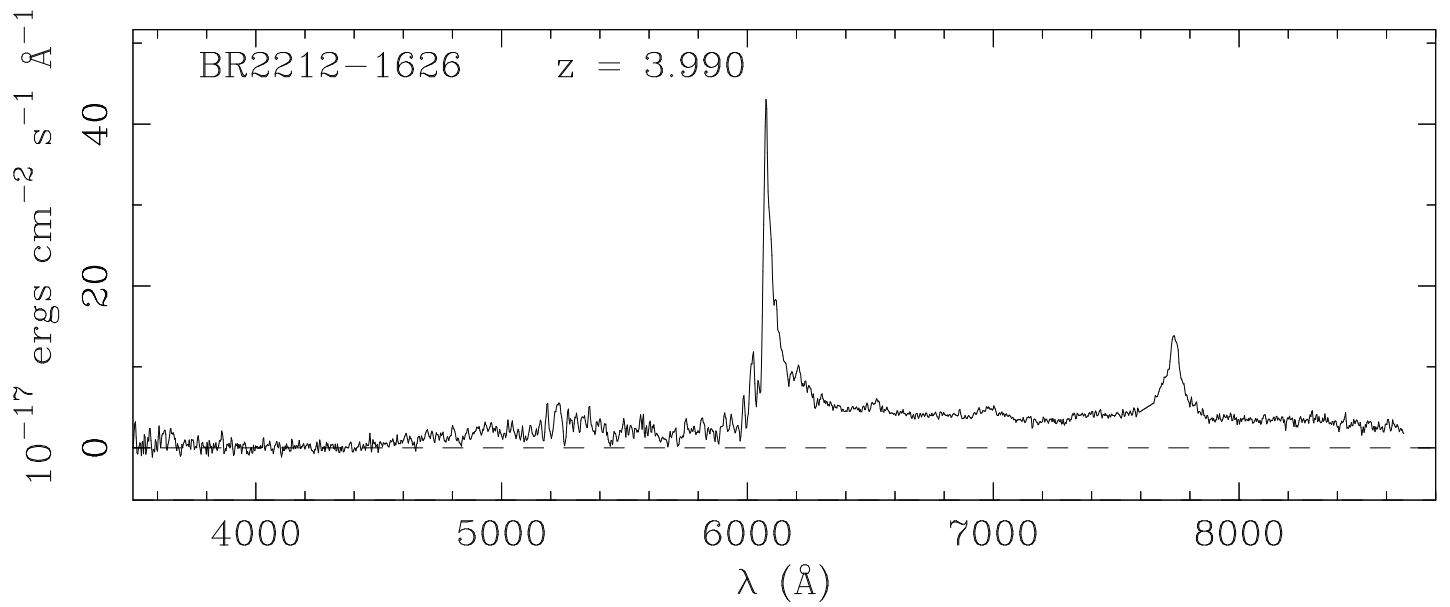


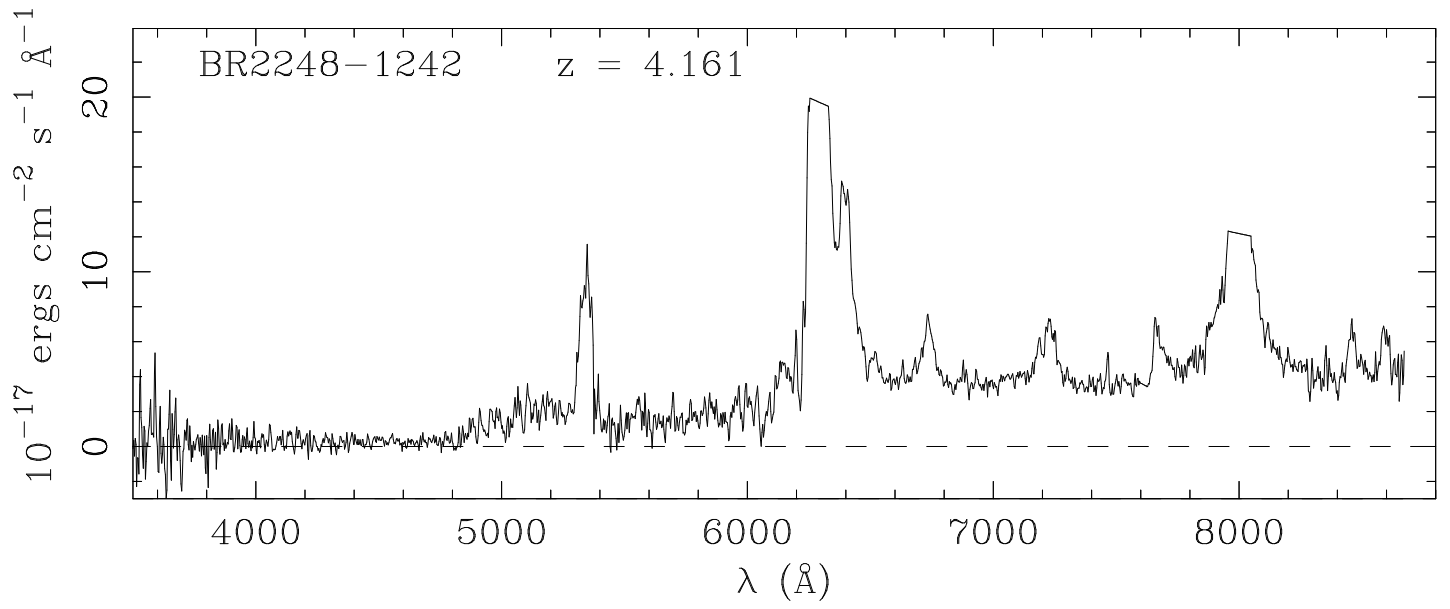
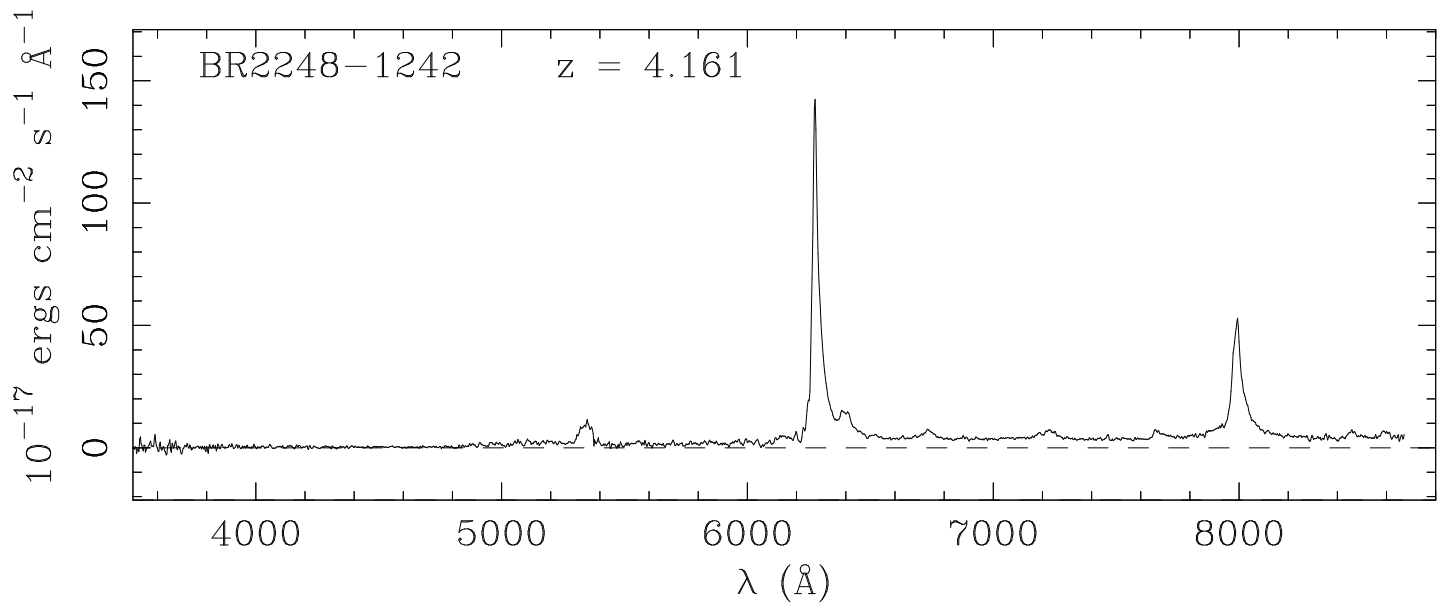


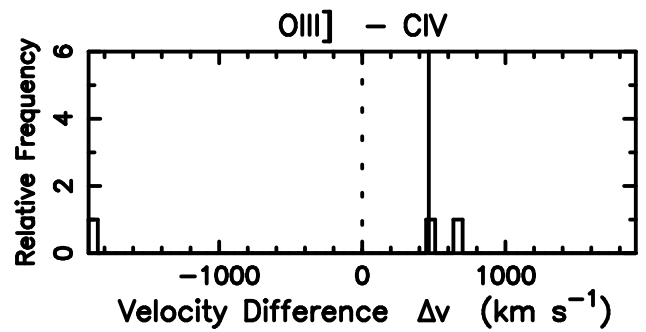
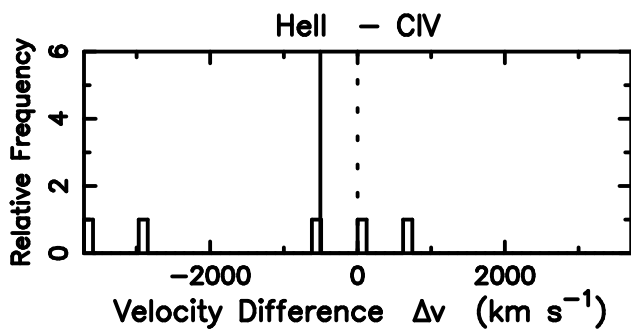
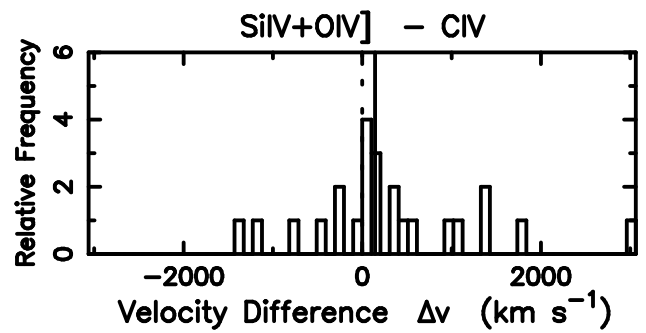
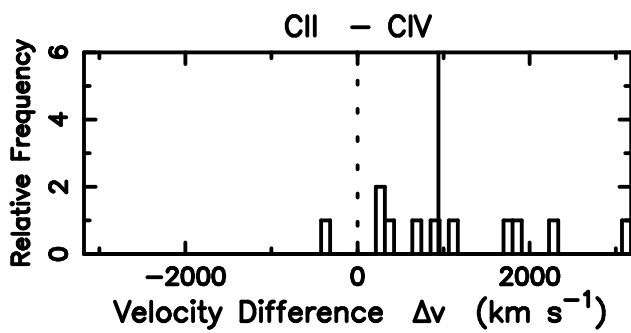
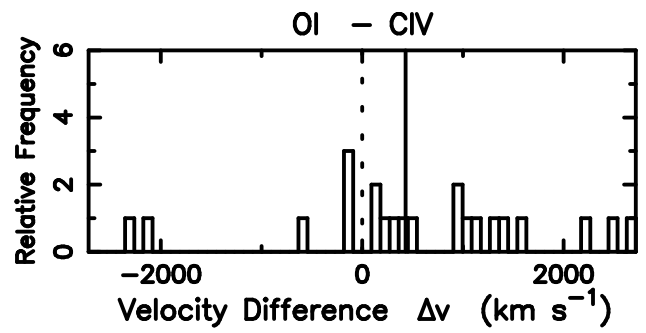
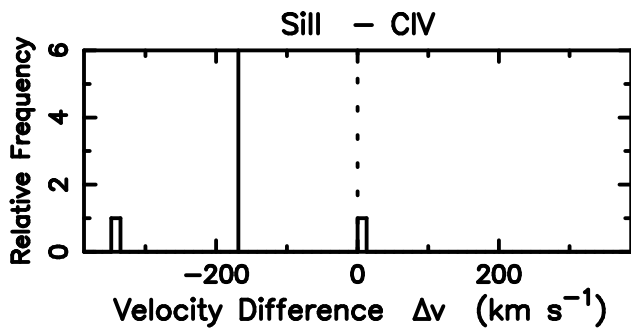
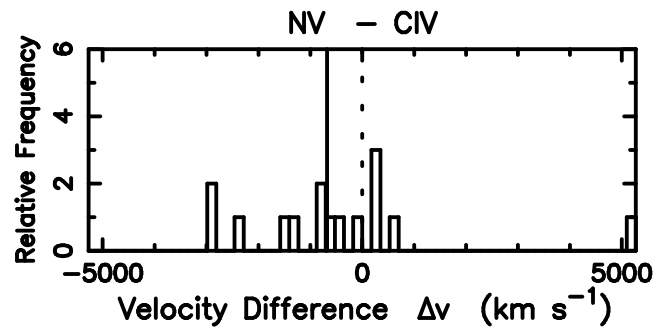
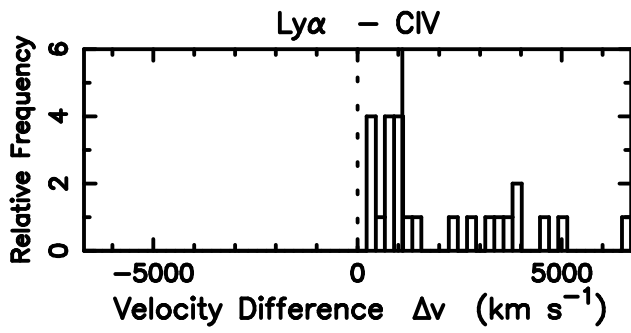
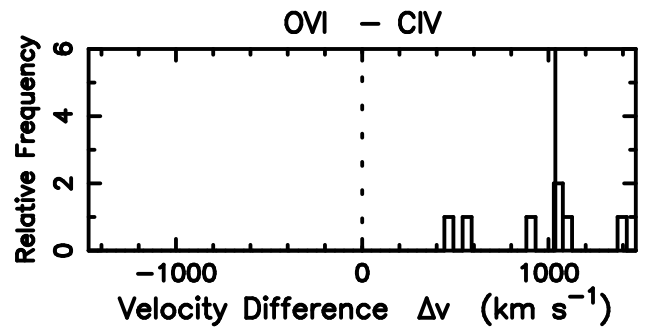
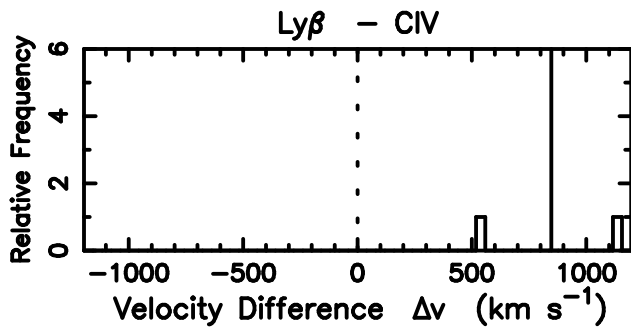


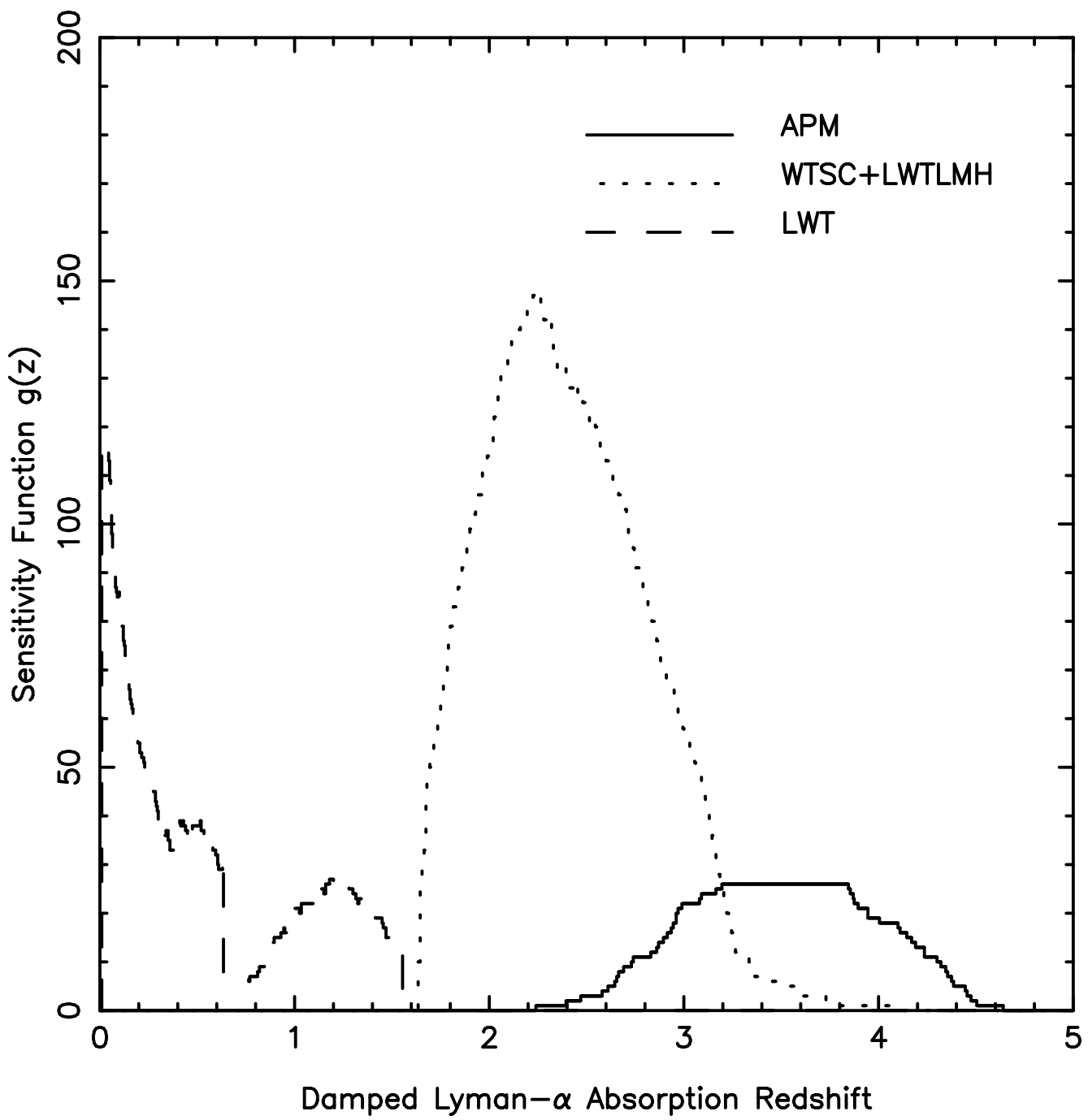


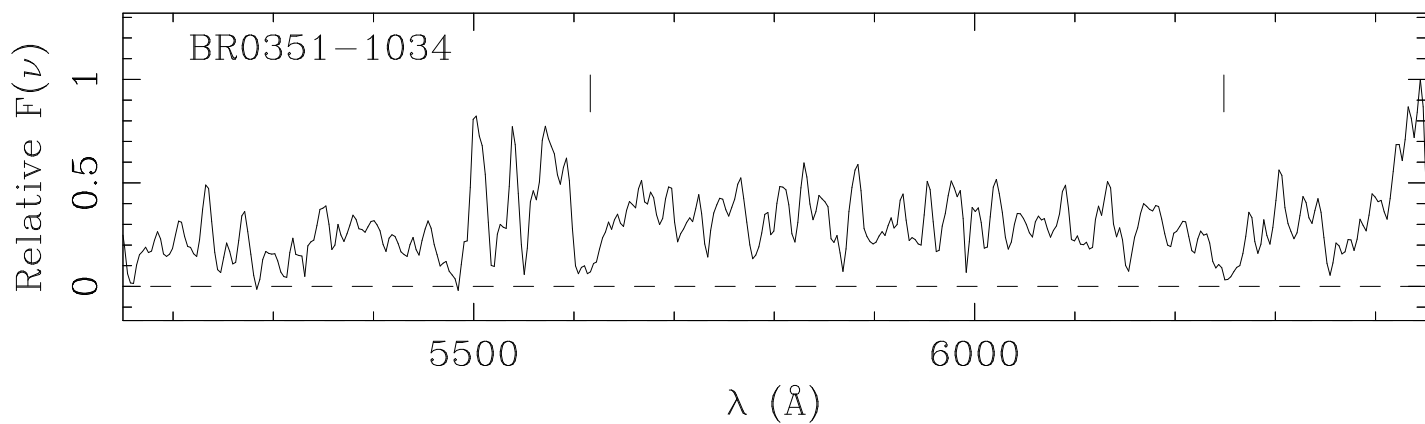
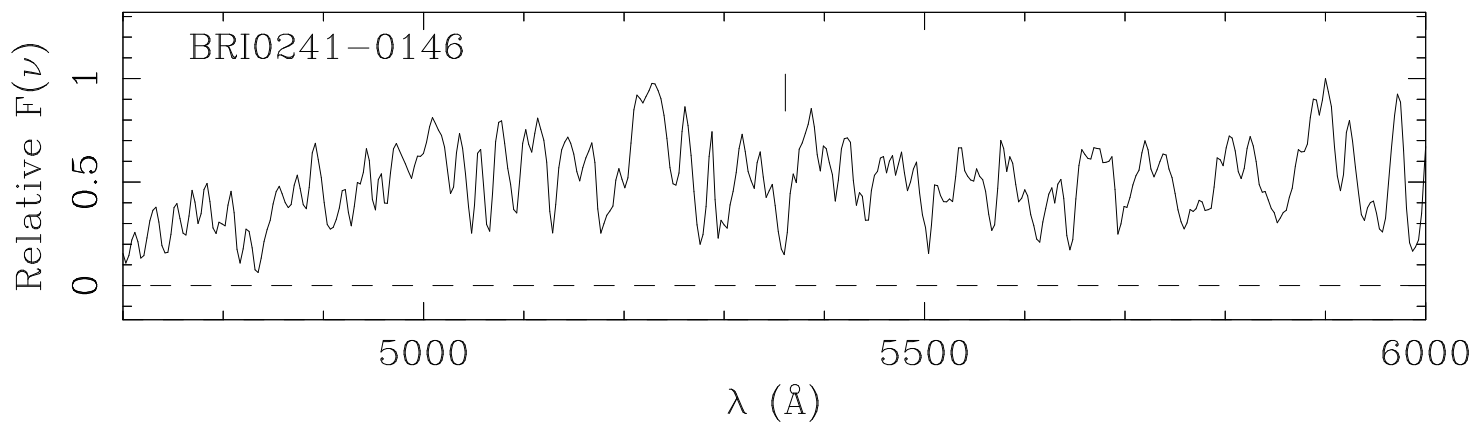
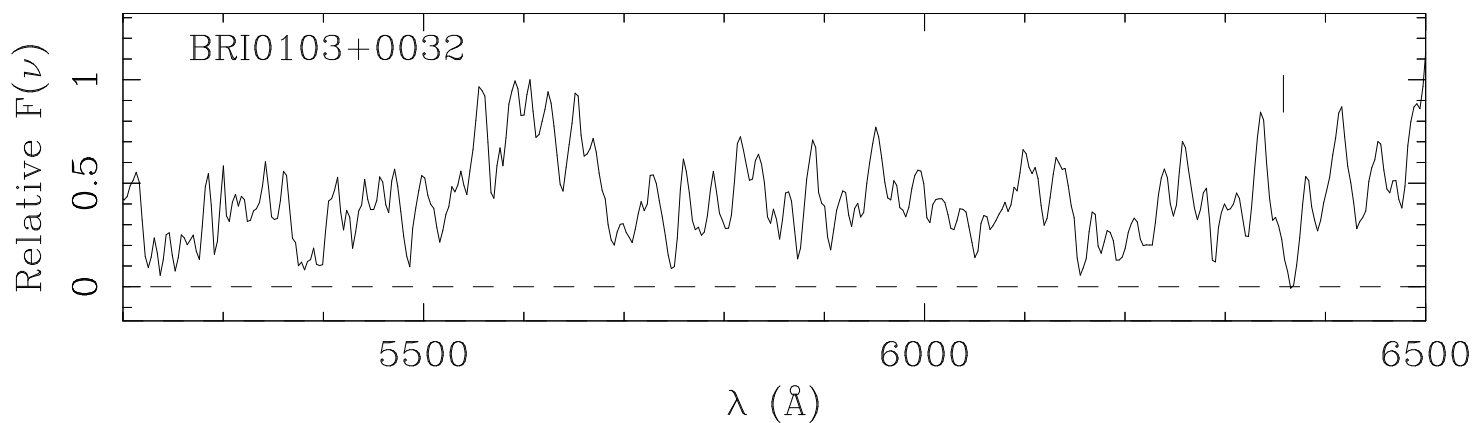
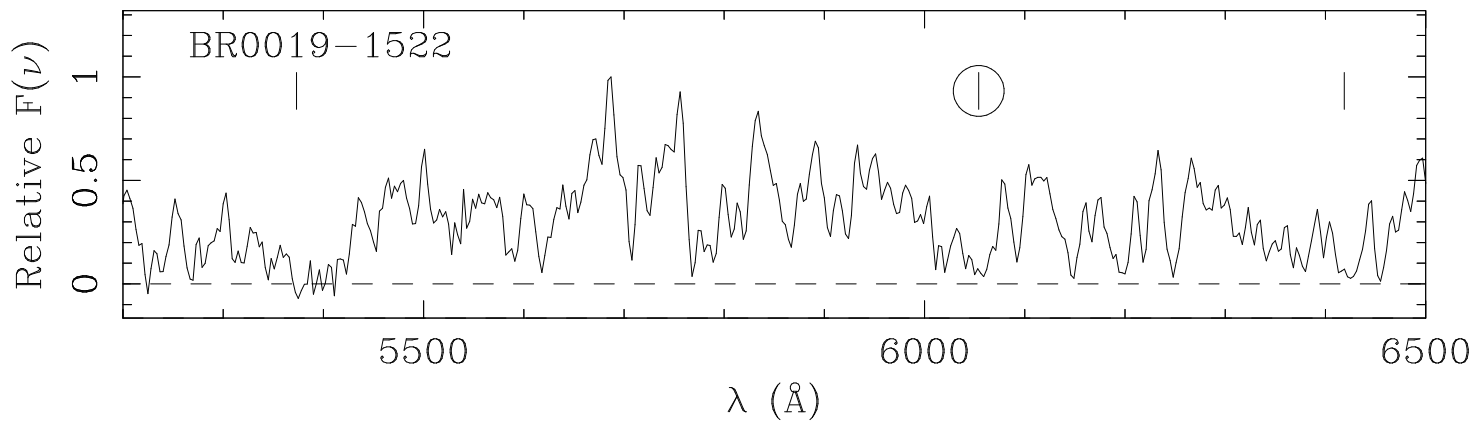


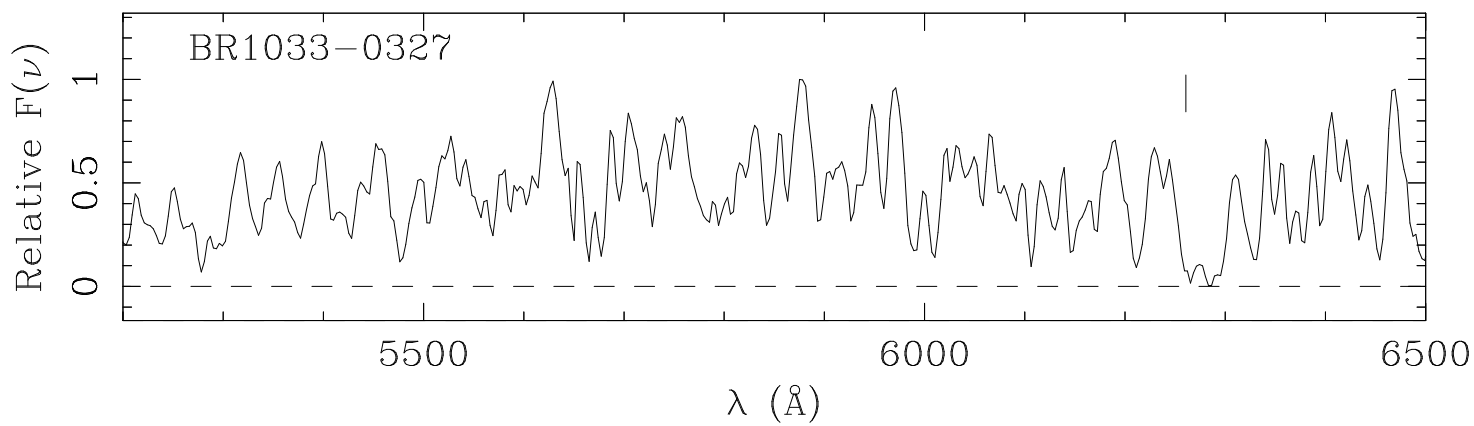
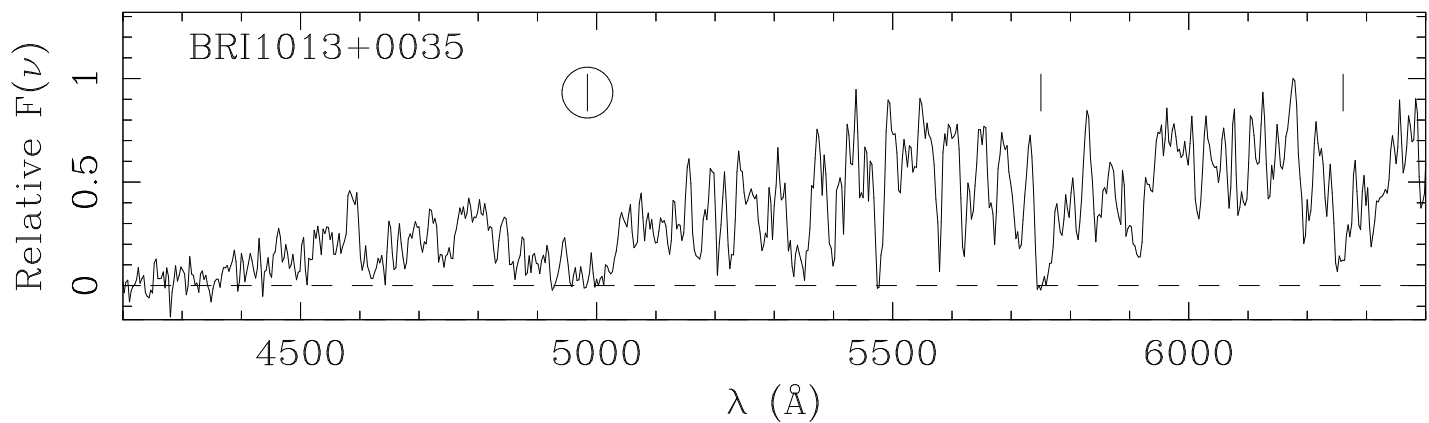
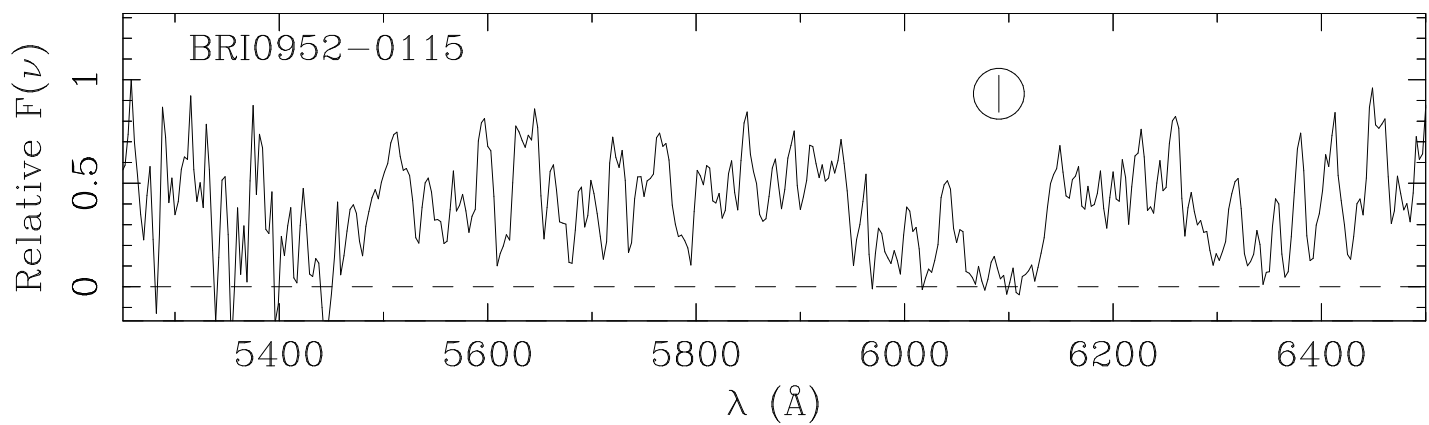
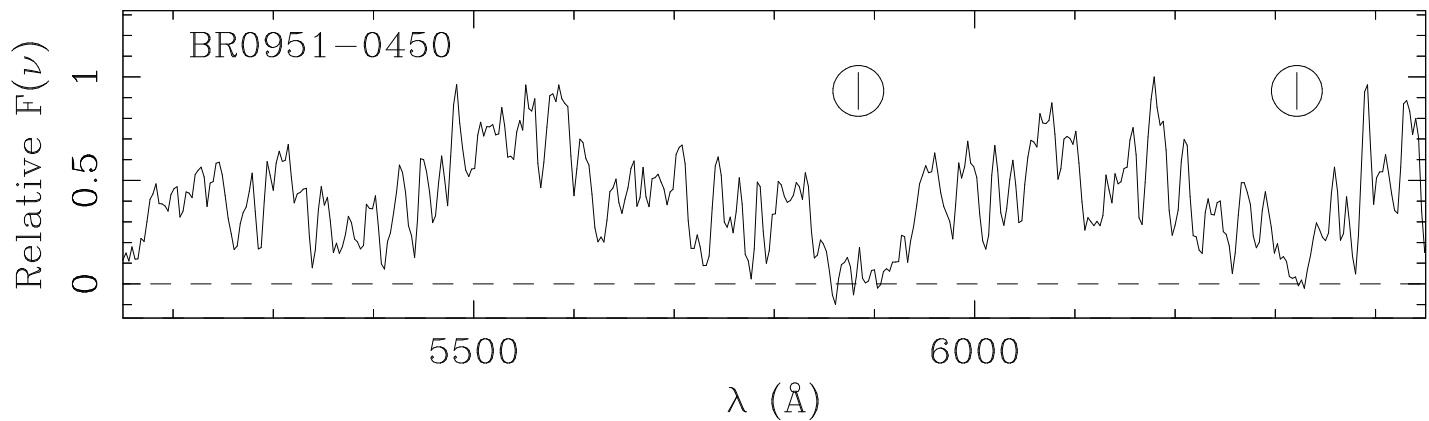


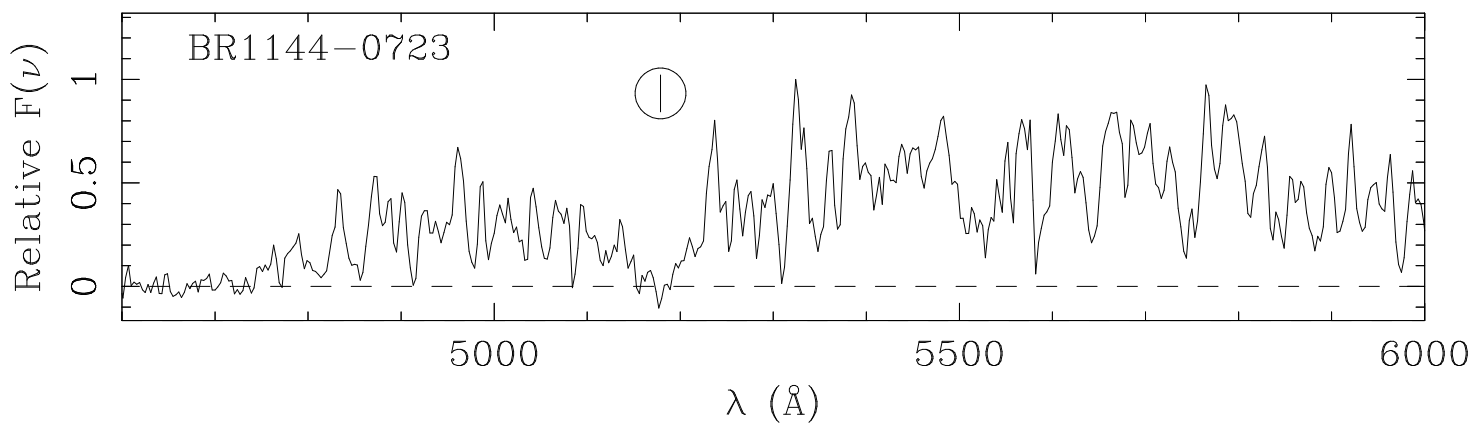
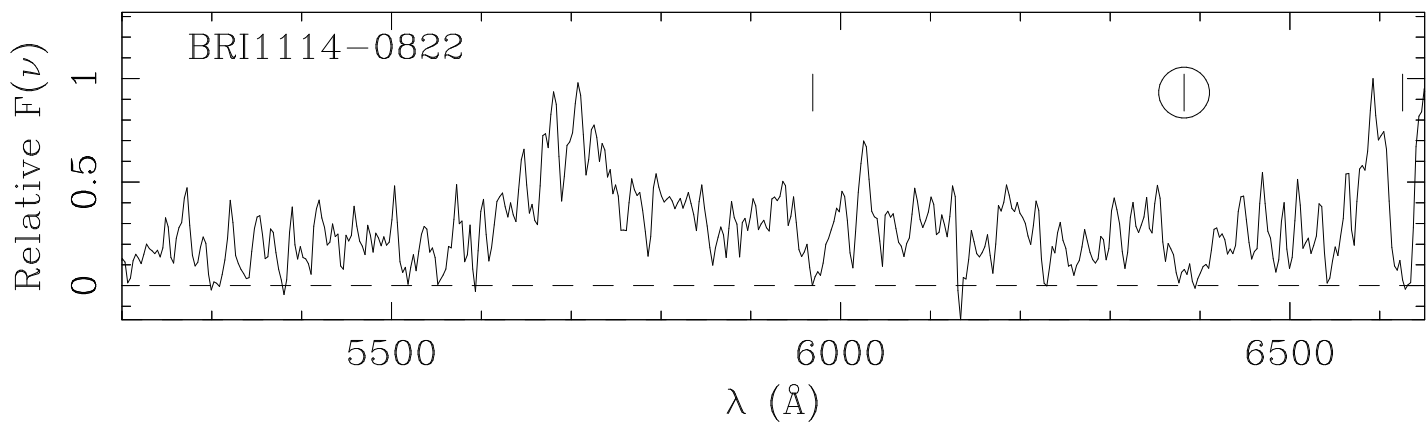
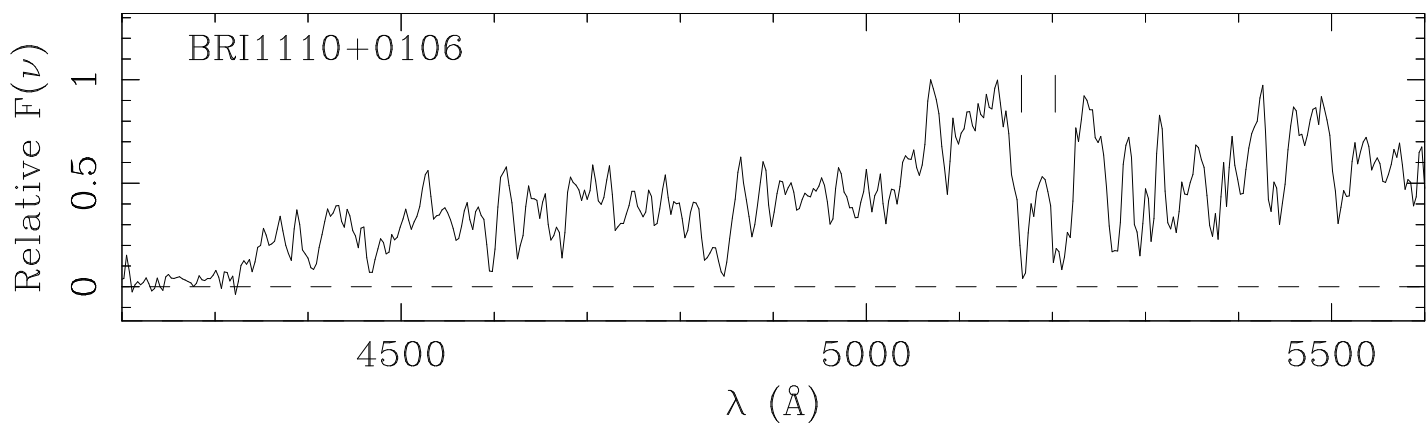
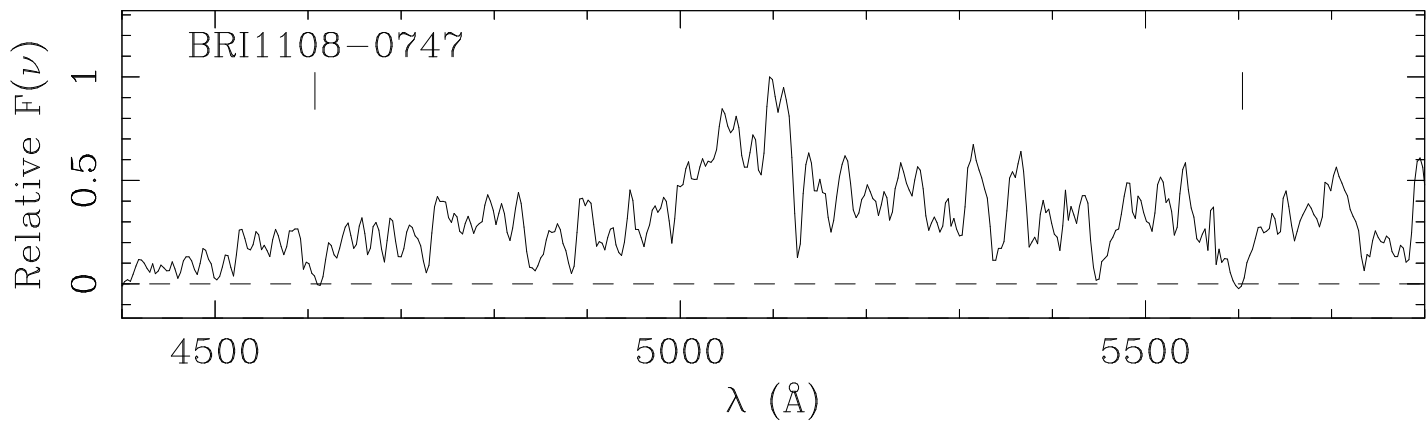


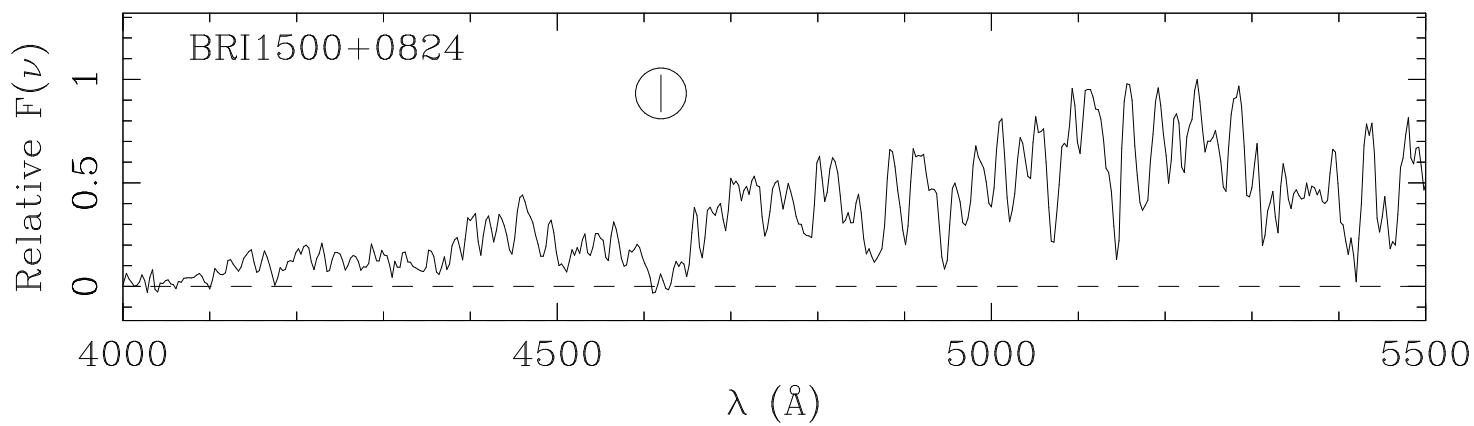
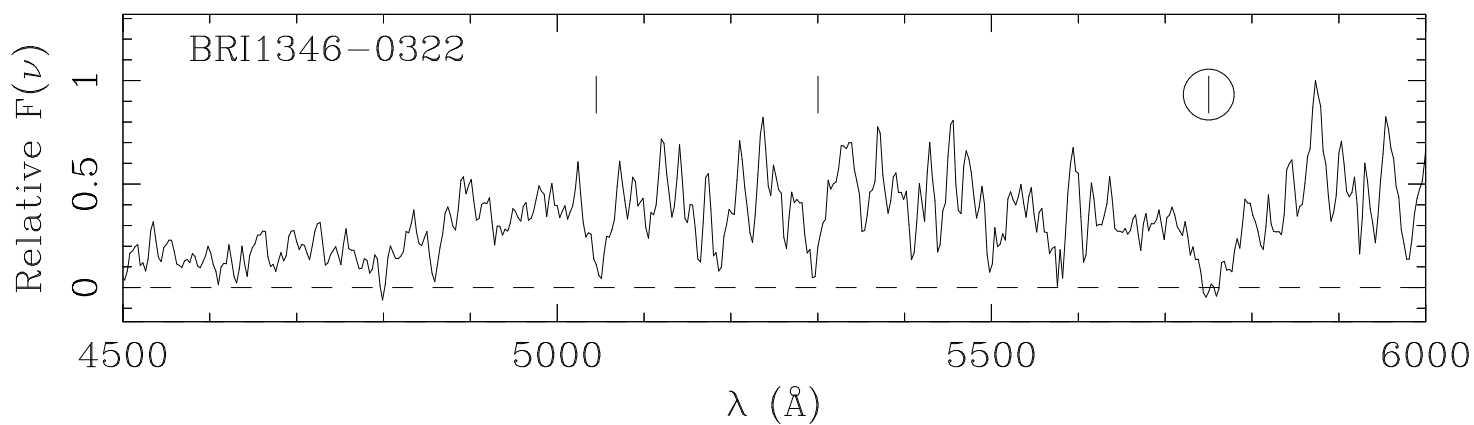
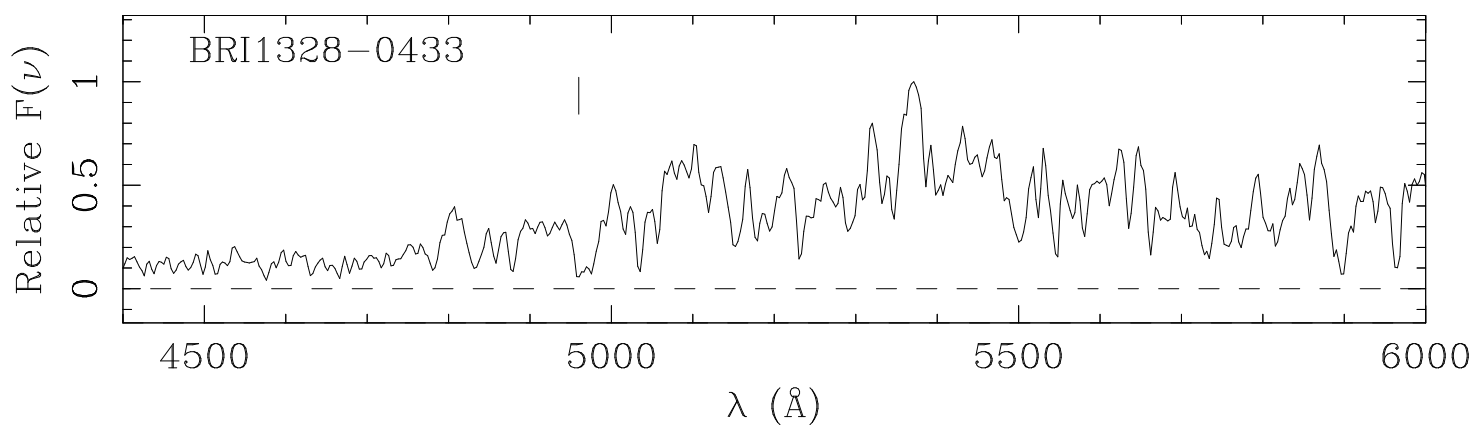
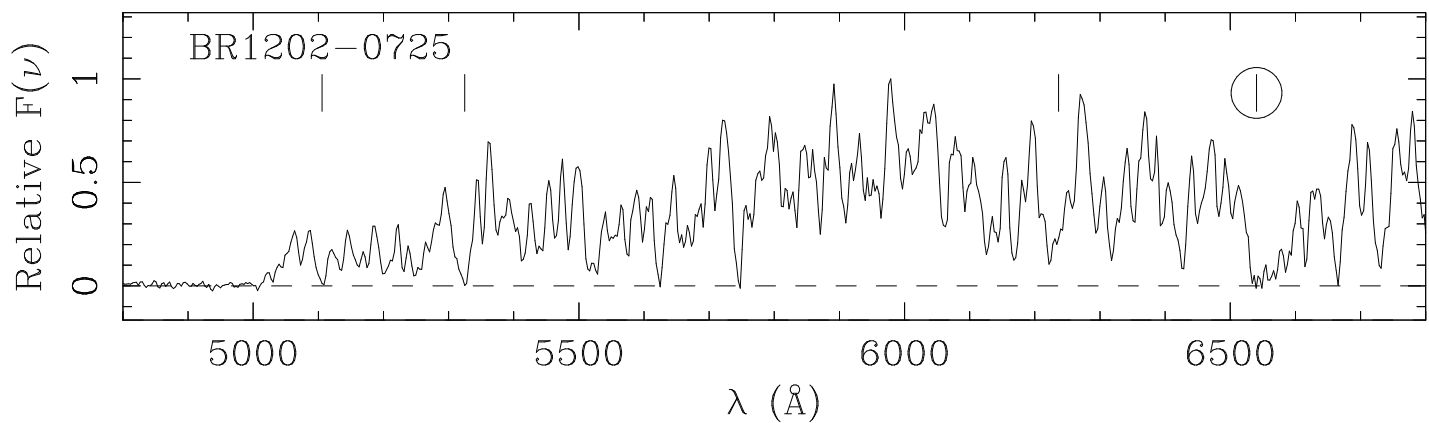


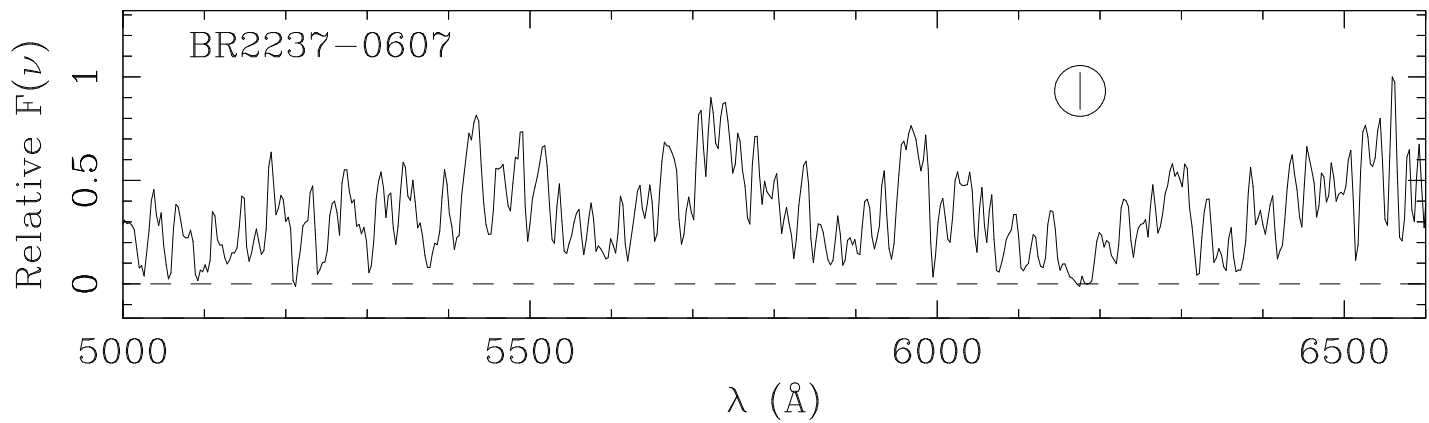












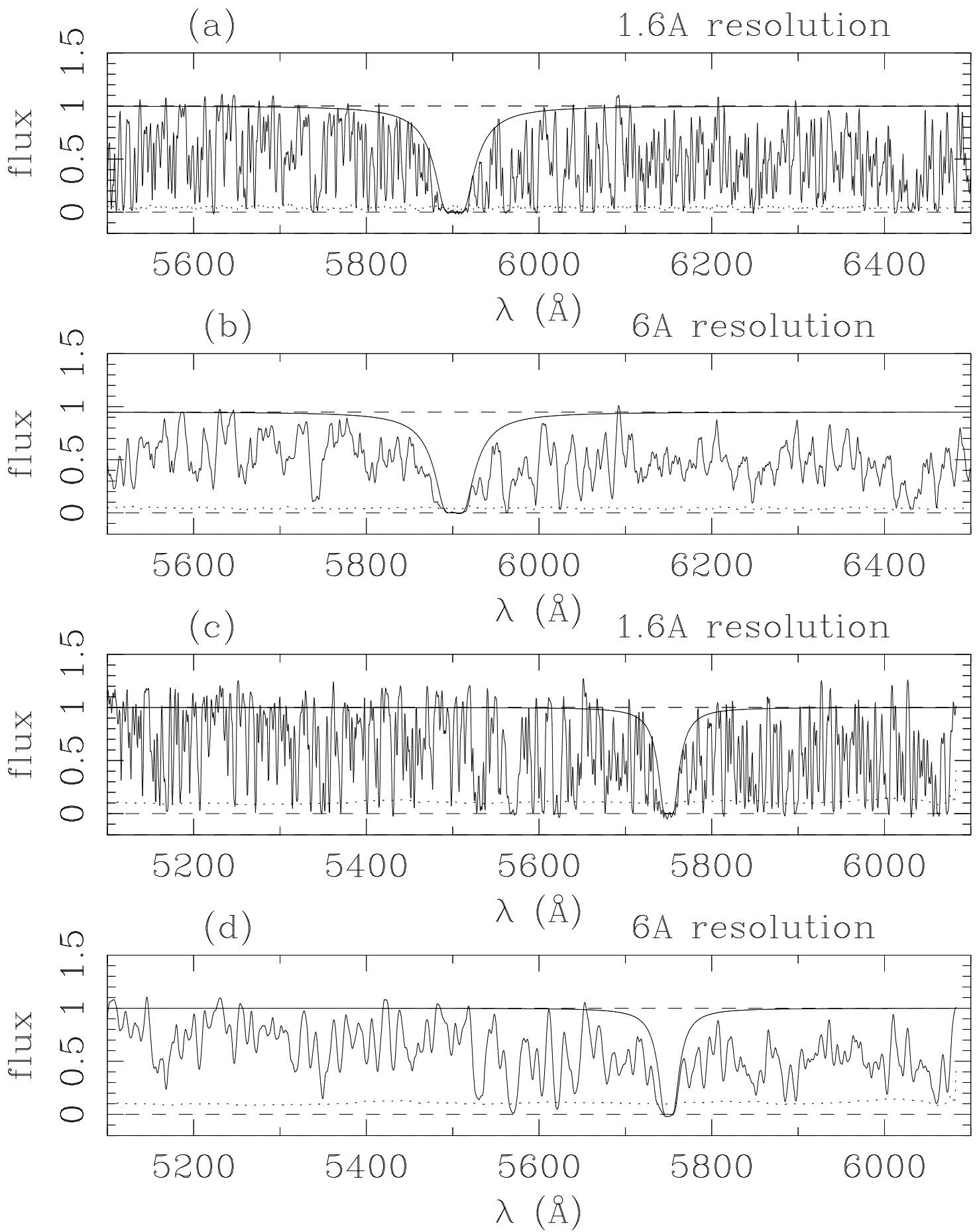


TABLE 1
WHT ISIS OBSERVATIONS LOG

QSO	Date (UT)	EXP (secs)	Arm	Slit (")	QSO	Date (UT)	EXP (secs)	Arm	Slit (")
BR0019 – 1522	92 Oct 04	2700	R/B	1.5	BR1117 – 1329	92 Apr 24	1200	R/B	1.5
		600	R/B	5			300	R	5
BRI0103 + 0032	93 Aug 21	2700	R	1.5	BR1144 – 0723	92 Apr 25	1800	R/B	1.5
		3000	B	1.5			300	R	5
		300	R/B	5	BR1202 – 0725	92 Apr 23	2700	R	1.5
BRI0151 – 0025	93 Aug 21	2700	R	1.5			2700	B	1.5
		3000	B	1.5			1200	R	1.5
		300	R/B	5			300	R	5
BRI0241 – 0146	93 Aug 21	1800	R/B	1.5		93 Apr 17	2700	R	1.5
		300	R/B	5			3000	B	1.5
BR0245 – 0608	93 Aug 21	2700	R	1.5			600	R	5
		3000	B	1.5	BR1302 – 1404	93 Apr 17	1500	R/B	1.5
		300	R/B	5	BR1328 – 0433	93 Apr 17	2700	R	1.5
BR0351 – 1034	93 Aug 21	900	R/B	1.5			3000	B	1.5
	93 Sep 20	2700	R	1.5	BRI1335 – 0417	92 Apr 25	2700	R/B	1.5
		2800	B	1.5			300	R	5
BR0401 – 1711	95 Feb 02	3600	R/B	1.5	BRI1346 – 0322	92 Apr 24	2700	R/B	1.5
							300	R	5
BR0945 – 0411	92 Apr 24	2700	R/B	1.5	BRI1500 + 0824	92 Apr 25	2700	R/B	1.5
		300	R	5			300	R	5
BR0951 – 0450	92 Apr 25	2700	R/B	1.5	GB1508 + 5714	93 Apr 17	2700	R	1.5
		300	R	5			3000	B	1.5
BRI0952 – 0115	92 Apr 24	900	R	1.5			600	R	5
		1000	B	1.5	MG1557 + 0313	92 Apr 25	2700	R/B	1.5
		300	R	5			300	R	5
BRI1013 + 0035	92 Apr 24	2700	R/B	1.5	GB1745 + 6227	93 Aug 92	2700	R	1.5
		300	R	5			3000	B	1.5
BR1033 – 0327	93 Apr 17	2700	R/B	1.5			600	R/B	5
		600	R	5	BR2212 – 1626	93 Aug 21	2700	R	1.5
BRI1050 – 0000	92 Apr 25	1800	R/B	1.5			3000	B	1.5
		300	R	5			450	R/B	5
BRI1108 – 0747	92 Apr 25	1800	R/B	1.5	BRI2235 – 0301	93 Aug 21	2700	R	1.5
		300	R	5			3000	B	1.5
BRI1110 + 0106	92 Apr 25	1800	R/B	1.5			450	R/B	5
		300	R	5	BR2237 – 0607	92 Oct 03	2700	R/B	1
BRI1114 – 0822	93 Apr 11	2700	R	1.5	BR2248 – 1242	93 Aug 21	2700	R	1.5
		3000	B	1.5			3000	B	1.5
		300	R	5			300	R/B	5

$\lambda_{ctr}=8494$

$\lambda_{ctr}=8494$

TABLE 2
QSO MAGNITUDES & POSITIONS

QSO	APM R	AB 7000Å	AB 1450Å×(1+z)	RA	Declination B1950.0	Ref. [†]
BR 0019 – 1522	19.0	18.8	18.8	00 19 35.9	–15 22 17	1
BRi0103 + 0032	18.6	18.9	18.8	01 03 45.2	+00 32 21	1
BRi0151 – 0025	18.9	19.0	18.9	01 51 06.0	–00 25 49	1
BRi0241 – 0146	18.2	18.4	18.4	02 41 29.3	–01 46 42	1
BR 0245 – 0608	18.6	18.9	18.8	02 45 27.4	–06 08 27	1
BR 0351 – 1034 ^a	18.6	–	–	03 51 23.7	–10 34 08	1
BR 0401 – 1711 ^b	18.7	–	–	04 01 40.8	–17 11 34	1
BR 0945 – 0411 ^c	18.8	18.9	18.9	09 45 18.6	–04 11 17	1
BR 0951 – 0450	18.9	19.4	19.2	09 51 25.0	–04 50 07	1
BRi0952 – 0115	18.7	18.8	18.7	09 52 27.2	–01 15 53	1
BRi1013 + 0035	18.8	19.1	19.0	10 13 15.0	+00 35 17	1
BR 1033 – 0327	18.5	18.8	18.8	10 33 51.5	–03 27 46	1
BRi1050 – 0000	18.6	19.5	19.4	10 50 46.7	–00 00 50	1
BRi1108 – 0747	18.1	18.8	18.8	11 08 41.9	–07 47 44	1
BRi1110 + 0106	18.3	19.0	18.9	11 10 12.3	+01 06 18	1
BRi1114 – 0822	19.4	20.1	19.7	11 14 55.2	–08 22 34	1
BR 1117 – 1329 ^c	18.0	18.1	18.1	11 17 39.4	–13 29 59	1
BR 1144 – 0723 ^c	18.6	18.9	18.8	11 44 02.4	–07 23 25	1
BR 1202 – 0725	18.7	18.1	18.0	12 02 49.2	–07 25 50	1
BR 1302 – 1404 ^c	18.6	18.4	18.4	13 02 46.8	–14 04 38	1
BRi1328 – 0433	19.0	19.1	19.1	13 28 54.9	–04 33 26	1
BRi1335 – 0417	19.4	19.2	19.1	13 35 27.5	–04 17 21	1
BRi1346 – 0322	18.8	19.4	19.4	13 46 41.1	–03 22 22	1
BRi1500 + 0824	19.3	19.1	19.1	15 00 18.6	+08 24 49	1
GB 1508 + 5714	18.9	20.0	19.8	15 08 45.2	+57 14 02	2
MG 1557 + 0313	19.8	20.0	20.0	15 57 00.5	+03 13 15	3
GB 1745 + 6227	18.3	19.3	19.3	17 45 48.0	+62 27 55	2
BR 2212 – 1626	18.1	18.7	18.6	22 12 44.8	–16 26 30	1
BRi2235 – 0301 ^c	18.2	18.5	18.5	22 35 47.4	–03 01 30	1
BR 2237 – 0607 ^a	18.3	–	–	22 37 17.4	–06 07 59	1
BR 2248 – 1242	18.5	19.5	19.4	22 48 39.8	–12 42 59	1

^aNo wide slit observations were obtained.

^bNot photometric conditions.

^cExhibits broad absorption lines (BAL).

[†]References for positions: (1) Irwin et al., in preparation, (2) Hook et al. (1995), (3) McMahon et al., in preparation

NOTE.—The APM R magnitudes are measured from the APM scans of the UK Schmidt plates. The errors are estimated to be ± 0.25 . The AB magnitudes at $\lambda=7000\text{\AA}$ and $\lambda=1450\text{\AA}\times(1+z)$ are calculated from the flux measured in the wide slit observations listed in table 1 using $AB = -2.5 * \log(f(\nu)[\text{ergs}/\text{s}/\text{cm}^2/\text{Hz}]) - 48.6$ as defined by Oke (1969). The errors are estimated to be ± 0.1 . The AB measures are 0.3 magnitudes fainter at 7000\AA and from 0.3 – 0.5 magnitudes fainter at $1450\text{\AA}\times(1+z)$ than magnitudes measured with respect to Vega.

TABLE 3
DETERMINATION OF QSO EMISSION REDSHIFTS

QSO	Redshift	Ly β 1026Å	OVI 1034Å	Ly α 1216Å	NV 1240Å	SiII 1263Å	OI 1304Å	CII 1335Å	Si/OIV 1400Å	CIV 1549Å	HeII 1640Å	OIII] 1663Å
BR 0019 – 1522	4.528±0.005			4.531				4.523	4.533	4.526		
BRI0103 + 0032	4.437±0.012			4.444	4.435			4.447	4.447	4.422	4.430	
BRI0151 – 0025	4.194±0.009			4.218	4.205			4.189	4.204	4.185	4.199	
BRI0241 – 0146	4.053±0.008			4.090				4.058	4.060	4.052	4.042	3.994
BR 0245 – 0608	4.238±0.013			4.265	4.200			4.250		4.240	4.223	
BR 0351 – 1034	4.351±0.005 ^a			4.398	4.320					4.327	4.327	
BR 0401 – 1711	4.236±0.014	4.261		4.251	4.257			4.247		4.235	4.227	
BR 0945 – 0411	4.145±0.010			4.174	4.147					4.146	4.145	
BR 0951 – 0450	4.369±0.022			4.433	4.438	4.339	4.390	4.386	4.377	4.345	4.336	
BRI0952 – 0115	4.426±0.020			4.467				4.448	4.432	4.425	4.400	
BRI1013 + 0035	4.405±0.038			4.442						4.432	4.378	
BR 1033 – 0327	4.509±0.005			4.521	4.503			4.511	4.516	4.507	4.504	
BRI1050 – 0000	4.286±0.005		4.310	4.294				4.291		4.281	4.285	
BRI1108 – 0747	3.922±0.008	3.924	3.932	3.936	3.919			3.934	3.921	3.917	3.915	3.926
BRI1110 + 0106	3.918±0.006			3.988						3.916	3.913	3.924
BRI1114 – 0822	4.495±0.004	4.518	4.516	4.557			4.455	4.491	4.498	4.497		
BR 1117 – 1329	3.958±0.031	3.983	3.982	4.043			3.925		3.964	3.986		
BR 1144 – 0723	4.147±0.004			4.169	4.152					4.145	4.150	
BR 1202 – 0725	4.694±0.010 ^b			4.694						4.679		
BR 1302 – 1404	3.996±0.013			4.078	4.060					3.986	4.005	
BRI1328 – 0433	4.217±0.011			4.224	4.181			4.223		4.223	4.205	
BRI1335 – 0417	4.396±0.026			4.489	4.381			4.410	4.426	4.378	4.370	
BRI1346 – 0322	3.992±0.014			4.011	3.984			4.004		3.976	3.996	3.935
BRI1500 + 0824	3.943±0.013			3.991				3.950		3.951	3.928	3.965
GB 1508 + 5714	4.283±0.019			4.309	4.292			4.266		4.279	4.304	
MG 1557 + 0313	3.891±0.001		3.900	3.896	3.845			3.889		3.892	3.891	
GB 1745 + 6227	3.901±0.016		3.903	3.910	3.876			3.911	3.919	3.888	3.888	
BR 2212 – 1626	3.990±0.002			4.005	3.952			3.990		3.988	3.992	
BRI2235 – 0301	4.249±0.018			4.322				4.269	4.245		4.234	
BR 2237 – 0607	4.558±0.003			4.569				4.559		4.562	4.555	
BR 2248 – 1242	4.161±0.002		4.168	4.164	4.111	4.160	4.163	4.165	4.159	4.160	4.160	4.168

NOTE.—The redshifts in **boldface** type were used to calculate the mean QSO emission redshift.

^aRedshift calculated from the strong CIV absorption doublet.

^bRedshift calculated from the Ly α edge. The redshift quoted for CIV in the table is for an absorption feature.

TABLE 4
EMISSION LINE VELOCITY SHIFTS

Line Pair	Median ^{a,c} Δv (km s ⁻¹)	Mean ^a Δv (km s ⁻¹)	σ (km s ⁻¹)	N ^b
Ly β - CIV	850 \pm 210	850	420	2
OVI - CIV	1040 \pm 50	930	330	7
Ly α - CIV	1100 \pm 70	2050	1790	25
NV - CIV	-680 \pm 130	-450	1930	15
SiII - CIV	-170 \pm 120	-170	240	2
OI - CIV	430 \pm 60	550	1260	22
CII - CIV	940 \pm 100	1130	1040	11
SiIV+OIV] - CIV	140 \pm 40	320	960	24
HeII - CIV	-500 \pm 376	-1270	1880	5
OIII] - CIV	470 \pm 470	-240	1410	3

NOTE.—The emission line redshifts are listed in table 3.

^a $\Delta v = c * (z - z_{\text{civ}}) / (1 + z_{\text{civ}})$

^b N = number of pairs of lines used in the calculation

^c The error is σ/N .

TABLE 5— *Continued*

QSO	λ (Å)	W	$\sigma(W)$	Ion	z	
BR1500 + 0824	6106.8	1.4	0.3	FeII	2.797	
	6343.9	4.0	0.5	AlIII	2.796	
	6545.6	1.7	0.5	-	-	
	6819.0	4.9	0.7	FeII	1.909	
	6907.6	4.0	0.4	FeII	1.910	
	6931.3	7.3	0.6	FeII	1.909	
	7524.2	3.9	0.6	FeII	1.908	
	7563.7	7.7	0.8	FeII	1.909	
	7648.5	2.4	0.4	CIV	3.940	
	7660.8	2.8	0.4	CIV	3.940	
	8130.5	14.8	0.7	MgII	1.908	
	8150.1	10.6	0.7	MgII	1.908	
	GB1508 + 5714	6518.1	2.3	0.5	-	-
		7428.5	3.7	1.1	-	-
MG1557 + 0313	5952.6	6.4	0.3	-	-	
	7583.3	2.4	0.4	CIV	3.898	
GB1745 + 6227	7596.1	1.5	0.4	CIV	3.898	
	5957.5	1.8	0.2	-	-	
BR2212 - 1626	6910.1	6.2	0.7	MgII	1.471	
	6928.8	6.3	0.7	MgII	1.471	
	7098.1	2.0	0.6	-	-	
	7512.3	1.3	0.4	FeII	2.323	
	7785.8	3.2	0.8	FeII	2.322	
	7887.3	2.7	0.8	FeII	2.322	
	7914.9	6.9	1.1	FeII	2.321	
	8590.3	4.1	1.1	FeII	2.321	
	8637.0	6.1	1.3	FeII	2.322	
	BR2237 - 0607	6167.3	2.8	0.6	-	-
6276.0		2.3	0.5	-	-	
6496.3		2.1	0.6	-	-	
8236.0		2.5	0.8	-	-	
BR2248 - 1242	6777.2	2.8	0.1	CII	4.078	
	6868.8	1.7	0.4	NV	4.545	
	6888.0	1.1	0.2	NV	4.545	
	7079.1	2.2	0.5	SiIV	4.079	
	7126.9	1.7	0.5	SiIV	4.079	
				or FeII	2.152	
	7310.2	1.6	0.6	-	-	
	7385.6	1.4	0.4	FeII	2.151	
	7472.4	3.6	0.5	MgII	1.672	
	7491.4	1.1	0.3	MgII	1.672	
				or FeII	2.156	
	7519.2	1.5	0.5	FeII	2.155	
	8164.1	1.6	0.5	FeII	2.156	
8487.7	1.6	0.5	CIV	4.482		
8502.3	0.6	0.2	CIV	4.482		
BR2248 - 1242	6487.5	6.0	1.1	-	-	
	7202.4	2.2	0.6	-	-	
	7939.5	2.0	0.6	-	-	

TABLE 5—*Continued*

QSO	λ (Å)	W	$\sigma(W)$	Ion	z
BR1114 – 0723 continued	7300.6	3.6	0.4	-	-
	7329.1	1.7	0.4	-	-
	7812.8	2.8	0.4	MgII	1.794
	7832.3	2.7	0.4	MgII	1.794
BR1202 – 0725	8331.5	4.2	1.3	-	-
	6888.5	5.6	0.3	MgII	1.463
	6906.2	6.1	0.3	MgII	1.463
	7005.0	3.8	0.3	CIV	3.525
	7017.2	1.3	0.3	CIV	3.525
	7067.4	1.4	0.3	CIV	3.565
	7079.9	0.8	0.2	CIV	3.565
	7122.3	2.8	0.3	FeII	1.753
	7161.1	3.1	0.3	FeII	1.754
	7183.2	3.8	0.2	CII	4.383
	7702.6	6.4	0.5	MgII	1.754
	7722.2	4.4	0.4	MgII	1.754
	7852.4	2.6	0.4	CIV	4.072
	7865.5	1.8	0.4	CIV	4.072
	8064.6	2.1	0.4	FeII	2.441
	8194.9	7.6	0.6	FeII	2.439
	8212.6	3.1	0.6	SiII	4.379
	8475.6	3.3	0.5	CIV	4.474
	8491.3	1.8	0.4	CIV	4.474
	8793.0	3.8	0.5	CIV	4.679
	8806.1	1.4	0.4	CIV	4.679
	8891.4	2.5	0.6	FeII	2.437
	8937.7	2.7	0.7	FeII	2.438
	9053.9	3.9	0.9	MgII	2.238
	9076.2	3.1	0.7	MgII	2.238
	9314.7	4.6	0.6	-	-
	9337.1	8.4	0.6	MgII	2.339
9360.1	5.8	0.6	MgII	2.339	
9526.4	4.5	1.3	MgI	2.339	
9630.6	13.4	1.0	MgII	2.444	
9656.1	9.8	1.0	MgII	2.444	
BR11328 – 0433	6797.6	5.4	0.5	FeII	1.628
	6832.7	8.0	0.7	FeII	1.628
	6862.8	2.9	0.6	-	-
	7349.4	15.0	0.6	MgII	1.628
BR11335 – 0417	7367.6	13.2	0.6	MgII	1.628
	6617.0	2.4	0.3	FeII	1.823
	6702.4	1.3	0.4	FeII	1.823
	6725.3	3.3	0.5	FeII	1.822
	6813.9	2.9	0.6	SiII	4.406
	7210.6	3.3	0.8	CII	4.403
	7339.6	2.4	0.6	FeII	1.823
	7696.9	2.6	0.5	-	-
	7707.6	5.2	0.5	-	-
	7892.6	5.5	0.7	MgII	1.822
BR11346 – 0322	7914.8	4.4	1.1	MgII	1.822
	6115.7	1.6	0.2	-	-
	6160.4	6.3	0.4	NV	3.974
	6182.3	7.4	0.4	NV	3.974
	6207.1	1.1	0.3	-	-
	6428.4	1.8	0.6	-	-
	6654.7	1.8	0.6	FeII	1.943
	6749.8	7.5	0.8	CIV	3.359
	6760.2	5.0	0.7	CIV	3.359
	6986.5	1.2	0.3	FeII	1.943
	7002.2	1.8	0.5	SiIV	3.992
	7705.7	9.9	0.7	CIV	3.974
	7737.3	4.1	0.5	CIV	3.994
	8116.9	3.0	0.8	CIV	3.994
8222.1	1.2	0.8	-	-	
8231.8	1.8	0.8	MgII	1.944	

TABLE 5— *Continued*

QSO	λ (Å)	W	$\sigma(W)$	Ion	z	
BRI0952 – 0115 continued	7776.9	7.9	0.6	CIV	4.023	
	7788.5	3.2	0.6	CIV	4.023	
	7987.2	3.3	0.8	-	-	
	8082.3	1.9	0.5	FeII	4.025	
	8234.5	1.8	0.4	-	-	
	8344.7	5.6	0.6	-	-	
	8383.8	4.7	0.5	MgII	1.993	
	8403.9	2.5	0.4	MgII	1.993	
	8418.9	2.4	0.6	-	-	
	8482.8	2.3	0.5	-	-	
	8663.2	2.7	0.9	-	-	
	BRI1013 + 0035	6599.4	4.4	0.4	FeII	3.103
		6855.6	6.3	0.5	-	-
		6911.3	2.5	0.5	FeII	2.057
7169.2		5.2	0.5	FeII	2.059	
7260.8		3.3	0.6	FeII	2.058	
7287.1		6.9	0.5	FeII	2.058	
7303.2		0.8	0.2	-	-	
7324.8		3.0	0.7	-	-	
7907.7		5.2	0.9	FeII	2.057	
7948.5		6.8	0.7	FeII	2.057	
8539.9		8.4	0.6	MgII	2.054	
8561.2		9.1	0.6	MgII	2.054	
BRI1033 – 0327		6689.2	2.9	0.2	-	-
		6869.4	1.9	0.3	CII	4.148
BRI1050 – 0000	6487.3	1.7	0.3	CII	3.861	
	6776.0	2.1	0.5	SiIV	3.862	
	6818.6	1.7	0.5	SiIV	3.862	
	7528.0	3.7	0.6	CIV	3.862	
	7538.1	4.3	0.6	CIV	3.862	
	8117.7	1.6	0.3	-	-	
BRI1108 – 0747	8141.8	0.6	0.2	-	-	
	5977.9	6.1	0.3	-	-	
	6630.1	2.6	0.5	-	-	
	6791.7	3.1	0.4	-	-	
	6804.1	0.7	0.2	-	-	
	7083.9	1.4	0.4	CIV	3.575	
	7094.0	1.1	0.3	CIV	3.575	
	7132.3	2.5	0.4	CIV	3.607	
	7143.8	1.2	0.4	CIV	3.607	
	8310.5	4.24	0.9	-	-	
	BRI1110 + 0106	6413.0	2.7	0.5	FeII	1.479
6446.4		1.9	0.5	FeII	1.479	
6634.7		1.4	0.4	-	-	
6932.2		1.6	0.4	MgII	1.479	
6950.7		1.5	0.4	MgII	1.479	
7158.6		1.7	0.5	-	-	
7299.6		1.6	0.5	-	-	
7323.0		2.4	0.6	-	-	
7829.7		2.2	0.7	MgII	1.800	
7852.1		2.5	0.8	MgII	1.800	
8574.3		4.5	1.1	-	-	
BRI1114 – 0723	6697.5	3.0	0.3	MgII	1.395	
	6713.7	3.1	0.3	MgII	1.395	
	6846.4	1.6	0.3	CIV	3.422	
	6858.7	1.2	0.3	CIV	3.422	
	6877.1	4.8	0.6	-	-	
	7016.4	2.5	0.6	-	-	
	7076.9	3.6	0.4	CIV	3.571	
	7088.1	1.9	0.4	CIV	3.571	
	7105.2	2.0	0.4	CIV	3.589	
	7116.3	1.4	0.3	CIV	3.589	
	7280.2	4.3	0.5	-	-	

TABLE 5—*Continued*

QSO	λ (Å)	W	$\sigma(W)$	Ion	z
BR0351 – 1034 continued	7173.5	2.0	0.6	CIV	3.633
	7185.2	1.2	0.5	CIV	3.633
	7196.0	0.7	0.2	-	-
	7431.7	1.5	0.4	-	-
	7458.8	6.6	0.5	SiIV	4.352
	7507.5	5.2	0.4	SiIV	4.352
	7550.7	5.0	0.6	-	-
	7822.5	3.3	0.5	-	-
	7834.6	2.4	0.5	-	-
	7843.6	2.0	0.5	-	-
	7895.7	12.6	0.7	CIV	4.098
	7906.9	11.4	0.7	CIV	4.098
	7916.4	8.5	0.5	-	-
	7940.0	11.1	0.7	-	-
	7952.2	8.4	0.5	-	-
	8159.8	6.0	0.5	-	-
	8173.1	4.7	0.5	-	-
	8188.0	3.7	0.5	-	-
	8197.0	3.4	0.5	MgII	1.931
	8218.2	2.0	0.4	MgII	1.931
	8228.1	2.4	0.4	CIV	4.315
	8241.9	2.2	0.4	CIV	4.315
	8286.8	21.5	1.0	CIV	4.351
8297.7	15.1	1.0	CIV	4.351	
BR0401 – 1711	6382.5	2.7	0.1	-	-
	6972.7	1.6	0.3	-	-
	7198.9	3.1	0.3	-	-
	7297.7	2.4	0.3	-	-
	7307.9	2.2	0.3	-	-
	7344.4	1.6	0.3	-	-
	8095.0	2.7	0.1	CIV	4.229
	8109.5	2.0	0.1	CIV	4.229
	8396.9	4.9	0.8	-	-
	BR0951 – 0450	6553.5	5.7	0.4	SiIV
6598.8		2.0	0.4	SiIV	3.703
6614.1		3.1	0.4	-	-
6712.6		4.2	0.6	-	-
6769.5		3.5	0.6	SiIV	3.858
6815.9		2.0	0.4	SiIV	3.858
7282.7		5.5	0.7	CIV	3.703
7293.3		4.2	0.7	CIV	3.703
7359.6		5.0	1.1	-	-
7416.0		3.3	0.6	SiII	3.858
7456.7		2.4	0.7	-	-
7517.4		2.1	0.6	CIV	3.855
7528.4		2.8	0.6	CIV	3.855
8108.8		7.1	1.1	-	-
8306.1		1.8	0.5	CIV	4.364
BRI0952 – 0115	8317.3	1.1	0.3	CIV	4.364
	6648.4	2.0	0.2	CIV	3.294
	6660.2	1.3	0.2	CIV	3.294
	6704.9	6.3	0.4	CII	4.024
	6719.7	8.1	0.3	-	-
	6749.6	1.2	0.3	-	-
	6826.4	1.8	0.4	-	-
	6875.6	2.7	0.3	-	-
	6928.4	2.8	0.5	CIV	3.475
	6941.3	1.7	0.5	CIV	3.475
	7002.6	2.8	0.4	SiIV	4.024
	7047.6	2.2	0.4	SiIV	4.024
	7132.2	1.2	0.3	FeII	1.993
	7208.8	2.4	0.5	-	-
	7306.4	4.6	0.5	CIV	3.719
	7317.6	3.6	0.5	CIV	3.719
	7345.5	1.6	0.5	-	-
7478.4	1.6	0.5	-	-	
7669.4	3.9	0.5	SiII	4.024	

TABLE 5
METAL ABSORPTION SYSTEMS

QSO	λ (Å)	W	$\sigma(W)$	Ion	z
BR0019 – 1522	6777.7	4.4	0.3	SiII	3.439
	6805.5	5.0	0.4	CIV	3.396
	6819.3	1.7	0.4	CIV	3.396
	7141.0	2.0	0.5	FeII	3.440
	7153.9	1.9	0.4	-	-
BRI0103 + 0032	7417.2	3.4	0.5	-	-
	6616.6	3.4	0.1	MgII	1.366
	6634.2	5.4	0.2	MgII	1.366
	6664.6	1.0	0.2	-	-
	6695.1	9.7	0.4	FeII	1.810
BRI0151 – 0025	7325.0	8.3	0.7	FeII	1.817
	7880.5	2.2	0.6	MgII	1.818
	7898.5	4.2	0.7	MgII	1.818
	6405.0	5.9	0.4	NV	4.170
	6425.0	4.3	0.3	NV	4.170
BRI0241 – 0146	7549.7	1.1	0.3	CIV	3.876
	7562.7	1.0	0.3	CIV	3.876
				or FeII	1.908
	7582.9	2.9	0.6	-	-
	7890.0	1.2	0.3	-	-
	8003.1	6.2	0.7	FeII	1.910
	8132.4	4.7	0.8	MgII	1.908
	8153.5	4.4	0.8	MgII	1.908
	8628.2	3.8	1.2	-	-
	6317.8	1.1	0.4	-	-
BR0245 – 0608	6336.9	1.7	0.5	FeII	1.437
	6382.3	1.4	0.4	-	-
	6467.4	1.5	0.5	-	-
	6809.0	0.6	0.2	MgII	1.435
	6827.8	0.7	0.2	MgII	1.435
	6882.3	2.1	0.5	-	-
	6923.6	2.5	0.5	-	-
	6966.7	2.2	0.6	-	-
	7691.1	4.8	0.6	-	-
	8060.4	3.3	0.9	-	-
BR0351 – 1034	6312.4	11.2	0.5	-	-
	6356.4	17.0	0.5	FeII	1.712
	6380.5	4.9	0.4	-	-
	6438.0	4.6	0.4	FeII	1.708
	6453.2	4.2	0.4	FeII	1.712
	6477.5	0.9	0.2	CIV	3.184
	6488.0	3.2	0.4	CIV	3.184
	6861.5	2.8	0.6	-	-
	7047.2	1.9	0.5	FeII	1.710
	7093.1	4.1	0.5	-	-
	7104.8	1.9	0.4	-	-
	7160.7	2.1	0.4	SiIV	4.139
	7208.3	3.0	0.5	SiIV	4.139
	7580.5	3.0	0.5	MgII	1.711
	7600.9	3.5	0.6	MgII	1.711
7957.1	5.9	0.7	CIV	4.140	
7971.9	1.8	0.5	CIV	4.140	
BR0351 – 1034	6545.9	9.2	0.4	MgII	1.340
	6559.5	7.9	0.4	MgII	1.340
	6576.0	3.6	0.4	-	-
	6631.7	4.9	0.3	NV	4.353
	6653.0	4.4	0.4	NV	4.353
	6744.9	1.3	0.3	SiII	4.351
	6867.2	2.6	0.5	-	-
	6873.9	2.3	0.5	-	-
	6989.2	5.8	0.5	FeII	1.933
	7000.7	3.5	0.4	-	-
	7105.2	1.4	0.4	SiIV	4.098
	7148.3	1.4	0.4	SiIV	4.098

TABLE 6
APM COLOR SURVEY LYMAN-LIMIT SYSTEMS

QSO ^a	z_{em}	z_{min}	z_{lls}	τ_{lls}
BR 0019 – 1522	4.52	2.51	4.27	>5.8
BRI0103 + 0032	4.44	2.51	4.31	1.6
			4.15	>1.6
BRI0151 – 0025	4.20	2.51	4.05	>3.7
BR 0245 – 0608	4.24	2.51	4.23	>3.9
BR 0951 – 0450	4.37	2.84	4.22	>3.1
BRI0952 – 0115	4.43	2.84	4.25	>2.1
BRI1013 + 0035	4.41	2.84	3.78	>2.3
BR 1033 – 0327	4.51	2.84	4.19	>3.5
BRI1050 – 0000	4.29	2.84	4.08	>2.5
BRI1114 – 0822 ^b	4.51	2.84	4.50	>3.7
BR 1202 – 0725	4.69	2.84	4.52	>3.0
BRI1328 – 0433	4.22	2.84	4.25	0.6
			3.31	>1.5
BRI1335 – 0417 ^b	4.40	2.84	4.45	>3.1
GB 1508 + 5714	4.30	2.84	3.88	>4.6
BR 2237 – 0607	4.56	2.51	4.28	>2.6

z_{em} = QSO emission redshift

z_{min} = minimum z at which a LLS could be observed

z_{lls} = Lyman-limit system redshift

τ_{lls} = optical depth at the Lyman-limit

^a $z_{em} \geq 4.2$, used in Storrie-Lombardi, et al. (1994)

^b $((z_{em} - z_{lls}) / (1 + z_{em})) \times c < 4000 \text{ km s}^{-1}$

TABLE 7
APM DAMPED LYMAN- α ABSORPTION SURVEY

QSO	z_{min}	z_{max}	z_{em}	Metals ^a	z_{abs}	W_{rest} [Å]	$\log N_{HI}$ estimated
BR 0019 – 1522	2.97	4.473	4.528	SiII 1526, FeII1608 CIV1549	3.42	7.6	20.0
					3.98	12.3	20.5*
					4.28	8.0	20.1
BRI0103 + 0032	2.87	4.383	4.437		4.23	5.8	19.8
BRI0151 – 0025	2.74	4.142	4.194				
BRI0241 – 0146	2.86	4.002	4.053		3.41	5.7	19.8
BR 0245 – 0608	2.96	4.186	4.238				
BR 0351 – 1034	3.09	4.297	4.351	CIV1549	3.62	6.6	19.9
					4.14	6.3	19.9
BR 0401 – 1711	2.82	4.184	4.236				
BR 0951 – 0450	2.93	4.315	4.369	SiIV1400, CIV1549 SiII 1526	3.84	24.0	21.0*
					4.20	10.6	20.3*
BRI0952 – 0115	2.99	4.372	4.426	CII1334, CIV1549 SiIV1400, SiII 1526	4.01	18.0	20.8*
BRI1013 + 0035	2.61	4.351	4.405	FeII1608	3.10	17.5	20.8*
					3.73	9.6	20.2
					4.15	7.4	20.0
BR 1033 – 0327	2.91	4.454	4.509	CII1334	4.15	9.6	20.2
BRI1050 – 0000	2.83	4.233	4.286				
BRI1108 – 0747	2.64	3.873	3.922		2.79	8.3	20.1
				CIV1549	3.61	9.0	20.2
BRI1110 + 0106	2.58	3.869	3.918		3.25	5.2	19.7
					3.28	6.2	19.9
BRI1114 – 0822	3.19	4.440	4.495		3.91	6.7	19.9
					4.25	11.7	20.4*
					4.45	5.3	19.7
BR 1144 – 0723 ^b	2.89	4.096	4.147		3.26	17.8	20.8*
BR 1202 – 0725	3.16	4.637	4.694		3.20	5.4	19.7
					3.38	7.1	20.0
					4.13	7.8	20.1
				CII1334	4.38	13.2	20.5*
BRI1328 – 0433	2.24	4.165	4.217		3.08	8.3	20.1
BRI1335 – 0417	3.08	4.342	4.396				
BRI1346 – 0322	2.65	3.942	3.992		3.15	6.8	19.9
				CIV1549	3.36	5.0	19.7
					3.73	10.0	20.3*
BRI1500 + 0824	2.39	3.894	3.943	FeII1608, AlII1671	2.80	11.3	20.4*
GB 1508 + 5714	2.73	4.230	4.283				
MG 1557 + 0313	2.66	3.842	3.891				
GB 1745 + 6227	2.47	3.852	3.901				
BR 2212 – 1626	2.69	3.940	3.990				
BR 2237 – 0607	2.96	4.502	4.558	CII1334, SiIV1400	4.08	11.5	20.4*
BR 2248 – 1242	2.94	4.109	4.161				

* These candidates are above the statistical sample threshold of $N_{HI} \geq 2 \times 10^{20}$ atoms cm^{-2} .

z_{min} = minimum redshift at which a DLA could be observed

z_{em} = emission redshift of the QSO

z_{max} = 3000 km s^{-1} blueward of z_{em}

z_{abs} = redshift at which a DLA candidate was observed

^aMetals detected (see table 5) that correspond to the damped candidate redshift.

^bThis QSO exhibits some BAL characteristics. The damped candidate at $z=3.26$ is tentative as it falls at the same wavelength as OVI at $z=4.0$.